# ABSTRACT

WANG, XIN. Hydrodynamic Relaxation in a Unitary Fermi Gas. (Under the direction of John Thomas).

Thermodynamics and hydrodynamic transport properties in a resonantly interacting or unitary Fermi gas are of special interest since they are universal functions of density and temperature. However, the behavior of the shear viscosity $\eta$ and the thermal conductivity $\kappa_T$ of a unitary Fermi gas is not yet established. This dissertation provides a new time-domain, free evolution method of measuring hydrodynamic transport coefficients in quantum gases, by observing the free decay of a spatially periodic density profile in a box potential. Measurement of the evolution enables the first independent determination of both the universal thermal conductivity and the universal shear viscosity in a normal fluid strongly interacting Fermi gas, providing new parameter-free tests of predictions.

Hydrodynamic Relaxation in a Unitary Fermi Gas

by
Xin Wang

A dissertation submitted to the Graduate Faculty of
North Carolina State University
in partial fulfillment of the
requirements for the Degree of
Doctor of Philosophy

Physics

Raleigh, North Carolina
2022

APPROVED BY:

| | |
|---|---|
| Albert Young | Michael Kudenov |
| Thomas Schäfer | John Thomas<br>Chair of Advisory Committee |

# DEDICATION

For Yixuan

# BIOGRAPHY

Xin Wang was born in Wuhan, China on September 17, 1989. He attended Fudan University in 2009, where he participated in experimental condensed matter physics on iron-based superconductors for his junior research project under the guidance of Professor Donglai Feng. He studied the shear viscosity of spinning soft matters for his undergraduate thesis under the direction of Professor Luwei Zhou and received his B.S. in Physics in 2013. Later this year, he enrolled in the graduate program at North Carolina State University. He joined the AMO research group of Professor John Thomas in 2015. His research in the JET lab was focused on universal hydrodynamics in a strongly interacting Fermi gas. He also contributed to setting up new experimental apparatuses and improving system stability. He was awarded an M.S. in Physics in 2020, with his Ph.D. following in May 2022.

# ACKNOWLEDGEMENTS

I cannot precisely express how do I feel when I finally reach this point where I can write my dissertation and obtain my Ph.D. degree. The one thing I am pretty sure about is that I feel truly blessed to have these people around me in my long journey as a graduate student. Without them, I could never reach this far.

I would like to express my great appreciation to my advisor, Dr. John Thomas for his enormous support and help. It was my privilege of having John as my advisor and mentor. Besides his world-class talent and sharp insights in physics, he always creates a friendly, supportive and creative atmosphere for the whole group. These were what attracted me to join the group even though I knew the experiments we did were very hard and I had to wait for several years before taking over the system for my thesis project. Moreover, as a great mentor, he inspired me to both become an independent researcher and become a better person. His enthusiasm for physics is boundless. It is truly impressive that he thought about pressure waves on a road trip, and he does "Thermodynamic Sudoku" after dinner as a habit. John treats every group member with respect and is supportive of their life. He has never pushed or forced us to do any research. Instead, he provided stimulative ideas and helped us with his knowledge. The only downside about John is that I had to think hard about how good I needed to be to graduate, since he usually said "You are good so you can stay." and "You are too good so you can never graduate." I have enjoyed the spirited discussion about physics and experiments with John. Our talk often goes beyond research and it has always been great fun, from his suggestion that Tempranillo is pretty good to his favorite closure " Hope the universe will be flat." Thank you, John, I am truly grateful for having you as my advisor.

I am indebted to our postdocs, Stetson Roof and Ilya Arakelyan. I learned a lot of lab and coding skills from Stetson when we set up the optics together. I especially thank you for letting me have more control and ownership of the lab when I was a junior in the group. It was great fun hitting the gym with him and talking about who is the best basketball player on the planet when taking boring data. I am glad that Stetson cannot argue with me in this thesis, so he has to agree that Lebron is better than MJ, hands down. Ilya, who knows everything in the lab, helped me a lot when I ran into trouble. His thorough understanding of what we do and solid lab skills helped me to take over the whole complicated system smoothly and be able to run it all by myself. Thank you for teaching me how to think and plan professionally. I appreciate his modest personality and his straightforward jokey

talking style.

I have had the fortune of working with bright graduate students from Duke and NC State. I would like to thank Arunkumar Jagannathan for introducing and explaining all the basics of the research in our group, which helped me in choosing my research topic. Your friendliness and kindness made me feel at home when I first joined the group. I enjoyed all kinds of talks with him, from stock investments to politics. What impresses me is his tennis skill is as good as his physics. Nithya Arunkumar, thank you for teaching me how to pick up and run the system. I am glad that you and Arun both like the spicy fried fish of Szechuan Taste which I recommended. Lorin Baird, the big brother of team Hydro, has always been a fun person to work with and talk to. Thank you for writing RoboXin which freed me from watching the atom number fluctuations, and I hope you have already found the foods in California are way better than that of the Mexican restaurant in Georgia. Kangara Mudiyanselage Jayampathi, the kindest person that I have ever met, has been always willing to help whenever I asked. Thank you for adding some joyful memories to my graduate student life, from bench pressing together to hanging out to cheer my marriage with those folks. Saeed Pegahan, I am glad that we all made it for being able to graduate with a lack of hands in both labs. I like your screenshot for the Zoom group meeting during the lockdown and it amused my committee during my defense.

There was a time John decided to stop recruiting new students so I was supposed to be the last one in our group. While he changed his mind and we were happy to welcome the junior members. Xiang Li, Camen Royce, and Jingjing Huang, thanks for bringing new energy and thoughts to the group and I enjoyed the fruitful discussions with you guys. I admire their dedication and I appreciate the opportunity for building leadership when teaching and working with them.

I would like to express my heartful gratitude to my parents who always support me unconditionally. They gave me great freedom to chase what I dreamt of. They trusted and respected every decision I made, allowing me to choose physics, a very fun but not that "useful" major, for my degrees. They never give me too much pressure on this long journey, and they are always there for me whenever I need them.

My special thanks to our graduate program coordinator, Rhonda Benett for helping me with all the paperwork and stuff through the years, as well as sharing me with the delicious candies.

I am in debt of gratitude to my committee members, Dr. Thomas Schäfer, Dr. Albert Young, and Dr. Michael Kudenov. Thank you for helping me in both doing research and writing this dissertation.

Finally, I would like to express my deepest gratitude to my wife, Yixuan Jiang. Thank you for understanding me, trusting me, and constantly supporting the whole family. I won't be able to make it happen without you. It was my greatest fortune that I met you at NC State, and it turned out to be my most important decision to go to the gym that day where we first met. Your sweet smile is my favorite coffee that wipes the fatigue and is what encourages me to work hard every single day. No matter enjoying sunshine and wines on Miami beach or cleaning and sanitizing all the groceries during the Covid lockdown, you are always with me. You always make sure that I have the best lunch box in the group even when you were so busy with your work. Thank you for taking over everything for our family in the last few months when I was sprinting to the finishing line. You are so smart that you would definitely become a great physicist if your love of food didn't lead you to study food science. Also, thank you for giving birth to our cute baby little James, who showed the greatest interest in physics at the age of 1, and tried to climb on my desk to type his own "equations" for me whenever I wrote my thesis at home. This forced me to hide in my closet to write the thesis and surprisingly it turned out to be more productive.

# TABLE OF CONTENTS

**List of Tables** . . . . . **ix**

**List of Figures** . . . . . **x**

**Chapter 1 Introduction** . . . . . **1**
1.1 Tunable Interactions . . . . . 3
1.2 Unitary Fermi Gas . . . . . 9
1.3 Ultracold Gases in Homogeneous Potentials . . . . . 12
1.4 Primary Results . . . . . 14
1.5 Significance of Current Work . . . . . 16
1.6 Dissertation Organization . . . . . 17

**Chapter 2 Theory** . . . . . **19**
2.1 Thermodynamic Theory . . . . . 19
2.1.1 Thermodynamic Relations . . . . . 19
2.1.2 Unitary Fermi Gas Thermodynamics . . . . . 21
2.2 Hydrodynamic Theory . . . . . 25
2.2.1 Hydrodynamic Linear Response . . . . . 26
2.2.2 Analytic Solution in Fourier Space . . . . . 28
2.2.3 Damped Oscillator . . . . . 33

**Chapter 3 Experimental Methods** . . . . . **35**
3.1 Atom Trapping and Cooling . . . . . 35
3.2 Imaging . . . . . 39
3.3 Optical Box . . . . . 40
3.3.1 Box Beam . . . . . 42
3.3.2 Digital Micromirror Devices . . . . . 45
3.3.3 The “Top-Hat” Beam Shaper . . . . . 50
3.3.4 Alignment of the Box . . . . . 57
3.4 Box Loading and Perturbation . . . . . 60
3.4.1 Box Potential . . . . . 61
3.4.2 Perturbing Potential . . . . . 64

**Chapter 4 Data Analysis Methods** . . . . . **68**
4.1 Data Taking and Processing . . . . . 68
4.2 Data Analysis Methods . . . . . 71
4.2.1 Numerical Integration of the Complete Equations . . . . . 71
4.2.2 Solving Ordinary Differential Equations . . . . . 81
4.2.3 Analytic Fit Function . . . . . 83
4.2.4 Exact Analytic Fit Function . . . . . 86
4.3 Data Analysis Details . . . . . 93

4.3.1 Statistical Uncertainty . . . 93
4.3.2 Determination of the Central Density . . . 95

**Chapter 5 Results . . . 98**
5.1 Experimental Results . . . 98
5.1.1 Sound Diffusivity . . . 106
5.2 Systematic Shifts of the Results . . . 108
5.2.1 Effect of Density Variation on the Measured Transport Coefficients . 108
5.2.2 Stored Energy . . . 111
5.2.3 Long Wavelength Limit . . . 113
5.3 Breakdown of Hydrodynamics . . . 115

**Chapter 6 Conclusion . . . 120**
6.1 Summary . . . 120
6.2 Outlook . . . 122

**References . . . 123**

**APPENDICES . . . 129**
Appendix A Code for Javis Halftoning . . . 130
Appendix B Code for Numerical Integration . . . 133
Appendix C Code for Exact Analytic Fit Function . . . 143

# LIST OF TABLES

Table 5.1 Measured Transport Coefficients . . . . . 106
Table 5.2 Validity of the Long Wavelength Limit . . . . . 115
Table 5.3 Comparison of Time Scales and Drude Corrections . . . . . 119

# LIST OF FIGURES


Figure 1.1 A unitary Fermi gas is loaded into a box potential with a small static spatially periodic perturbation $\delta U$, creating a spatially periodic 1D density profile. After $\delta U$ is abruptly extinguished, the dominant Fourier component exhibits a two-mode oscillatory decay (see Fig. 1.6). 3

Figure 1.2 Magnetic field dependence of the $2^2S_{1/2}$ ground state of $^6Li$. We use a 50-50 mixture of the two lowest spin states $|1\rangle$(spin up) and $|2\rangle$(spin down) for the experiment. Plot was originally drawn by Kinast [2006]. 5

Figure 1.3 Magnetic Feshbach resonance occurs due to the hyperfine coupling between the scattering continuum in the triplet potential (open channel) and the molecular bound state in the singlet potential (closed channel). When $B = B_{res}$, the energy of the triplet state moves downward into resonance with the singlet state. . . . . 7

Figure 1.4 The s-wave scattering length $a_s$ near a magnetic Feshbach resonance at $B_{res} = 832.18$ [Zürn et al. 2013]. When $B < B_{res}$, the scattering length is positive and the interactions are repulsive, this regime is called BEC side of the Feshbach resonance. When $B > B_{res}$, the scattering length is negative and interactions are attractive, this regime is called BCS side of the Feshbach resonance. When $B = B_{res}$, the scattering length diverges, yielding strong interactions. . . . . 8

Figure 1.5 Absorption images show the free evolution of the periodic density profile. An oscillatory decay of the ripples is observed. . . . . 14

Figure 1.6 Real part of the Fourier transform of the density perturbation $\delta n(q,t)$, normalized to $\delta n(q,0)$, for $q = 2\pi/\lambda$ with $\lambda = 22.7\,\mu$m. The reduced temperature $T/T_F = 0.46$. Blue dots: data; Red curve: analytic hydrodynamics model, Eq. 1.21. Inset shows contributions of thermal diffusion (orange) and first sound (blue). The error bars are statistical. 15

Figure 2.1 Reduced temperature $\theta = T/T_F$ versus adiabatic sound speed $\tilde{c}_S \equiv c_S/v_F$ and isothermal sound speed $\tilde{c}_T \equiv c_T/v_F$. For $\theta > 0.25$, $\theta$ monotonically increases with $\tilde{c}_S$ ($\tilde{c}_T$), showing that the fitted $\tilde{c}_S$ ($\tilde{c}_T$) can be used as a thermometer to determine $\theta$ in the normal fluid region. The blue dots are obtained from the equation of state of Ref. Ku et al. [2012]. The upper (lower) red solid curve shows a fit with a cubic polynomial, $\theta(\tilde{c}_S) = -0.399 + 0.958\,\tilde{c}_T + 0.839\,\tilde{c}_T^2 - 0.059\,\tilde{c}_T^3$, $\theta(\tilde{c}_T) = 0.478 - 4.410\,\tilde{c}_T + 11.688\,\tilde{c}_T^2 - 5.711\,\tilde{c}_T^3$. . . . . 23

Figure 2.2 Reduced temperature $\theta = T/T_F$ versus the heat capacities per particle at constant volume $c_{V_1}$ and at constant pressure $c_{P_1}$. The red lines are obtained from interpolations of the equation of state of Ref. Ku et al. [2012]. The upper (lower) black dashed curve shows the fit with a quartic polynomial, $c_{V_1} = 1.190 - 0.872\,\theta + 2.160\,\theta^2 - 1.387\,\theta^3 + 0.283\,\theta^4$ ($c_{P_1} = 1.904 - 3.223\,\theta + 7.998\,\theta^2 - 5.500\,\theta^3 + 1.194\,\theta^4$). . . . . 24

Figure 2.3 Components of the analytic fit function $\delta n(q,t)$ Eq. 2.57 and $\delta \tilde{T}(q,t)$ Eq. 2.59 for a typical data at $T/T_F = 0.46$. Red curve: Total fit function; Orange curve: Zero frequency, exponentially decaying (thermal diffusion) mode; Blue curve: oscillating, exponentially decaying first sound mode. Note that the two components are in phase for $\delta n(q,0)$ and 180° out of phase for $\delta \tilde{T}(q,0)$, ensuring an isothermal initial condition. . . . . 32

Figure 3.1 Experimental setup for initial cooling of $^6$Li atoms by the Zeeman slower and the slower beam and precooling by the MOT beams, repumper beams and MOT coils. MOT and repumper beams are overlapped and are shown together in red. Inset shows fluorescence from the atoms trapped in the MOT. *This figure is directly taken form thesis of Jagannathan [2016] for demonstration purpose.* . . . . . 37

Figure 3.2 Illustration of the box trap. A 532 nm beam propagating in the vertical (x) direction provides 4 vertical walls of the box. A 669nm beam propagating in the horizontal plane (y-z) provides the top and bottom sheets. Two CCD cameras view through x and y directions at each of the two spins, enabling in-situ imagery for both spins. . . . . 40

Figure 3.3 Box beam path along with the main chamber and imaging system. Top(bottom) orange(green) colored shapes represent a 669 nm gaussian (532 nm "top-hat") laser beam. Red colored shapes represent the imaging beams. . . . . 41

Figure 3.4 Illustration of the box trap. A 532 nm beam propagating in the vertical (x) direction provides 4 vertical walls of the box. A 669nm beam propagating in the horizontal plane (y-z) provides the top and bottom sheets. . . . . 44

Figure 3.5 (a) Setup of the horizontal DMD, key elements including a high power fiber, the DMD, a higher order diffraction beam block, a microscope objective and lenses. (b) Micromirror landed position and light paths [DMD], the orientation of the mirrors are diagonal respect to the DMD chip frame. . . . . 48

Figure 3.6 Left: In the proper trigger "slave mode", mirrors only respond to external triggers. Right: Example of another mode, where the mirrors refresh at a fixed time interval. . . . . 50

Figure 3.7 Grayscale image of a box made by the DMD with a gaussian input beam, taken by a ThorLabs CMOS camera. The light intensity varies and decrease rapidly for the long side. . . . . 51

Figure 3.8 Illustration of the box position, with respect to the magnetic coils proving high field (832 G). . . . . 52

Figure 3.9 A simulation of the relative intensity, as a function of the ratio of the radius(distance to the center) to the gaussian width. A certain radius prefers one optimal width; for radius larger than the Gaussian width, expanding the beam will increase intensity. . . . . 53
Figure 3.10 Typical setup for the "Top-Hat" beam shaper, including a collimated laser beam, a beam shaper element, a focusing lens and a focal plane for the application [THS]. EFL is effective focal length, $D$ is the input beam size, $d$ is the spot size. Figure only for demonstration, we actually use a round spot in the experiments. . . . . 55
Figure 3.11 Simulation results for the designed intensity profile for a TH-228-Q-Y-A "Top-Hat" beam shaper, with 3 mm input beam size and a perfect alignment. Image of the actual spot in experiments is shown in Fig. 3.12. . . . . 55
Figure 3.12 CMOS camera images of typical Top Hat beam applications. The disk in (a) is about 250 $\mu$m in diameter. The box pattern in (b) is about 200 by 95 $\mu$m. This figure is just to show our capability of making very shape edges, the box we actually use in experiments are much thicker to prevent atoms from accumulating outside of it and affecting the image (see Sec. 3.4). . . . . 57
Figure 3.13 Simulation results for a beam width departs from 3 mm. A larger beam is transformed to a hollow top and a smaller beam is transformed to a gaussian-like top. Above are 2-D spots at focal plane; Bottom are radial intensity profiles. . . . . 58
Figure 3.14 Relative position of the box, the FORT and the atom cloud during the box loading. Blue: atom cloud; Pink: FORT at final depth of forced evaporation; Gray: the optical box. . . . . 62
Figure 3.15 2D absorption images from the horizontal and vertical directions. The box dimension is roughly 52 (x) by 50 (y) by 160 (z) $\mu$m. Upper(lower) image pixel size, which is the camera pixel size divides by magnification, is 1.06(1.34) $\mu$m. . . . . 63
Figure 3.16 For a sinusoidal potential, the desired pattern (left); the digital halftoned binary pattern (middle); and the blurred halftoning pattern (right). A Jarvis Halftoning operation and the blurring effect of the projecting system, together, make the optical potential close to ideal. . . . . 65
Figure 3.17 Design of a sinusoidal perturbing potential (7 spatial periods of 23 $\mu$m wavelength), and the observed column density of the atom cloud from the horizontal view CCD camera. . . . . 66

Figure 4.1 Evolution of the atom cloud in the first 1400 $\mu$s is shown as 2D column density images (using a MATLAB 'jet' colormap with a shifted zero-color for better look). An averaged background is subtracted from each image to show better contrast of the perturbations. Also, each image is averaged by a vertical-flipped "mirror" image to show better vertical symmetry. Clearly we see a oscillatory decay. . . . . 70
Figure 4.2 Column Density $n_0(x,z)$ and 1D background density $\tilde{n}_0(z)$ (blue dots). Red curve: Fit of Eq. 4.3. . . . . 72
Figure 4.3 Box potential in units of local Fermi energy $\epsilon_F(n_0)$ for the central density $n_0$. The potential is determined from the measured background density $n_0(z)$ using Eq. 4.4. Note that the curvature at the bottom of the box potential energy arises from curvature in the bias magnetic field, which produces a small confining harmonic potential. A typical $\epsilon_F(n_0) \simeq 0.2\,\mu$K, and the box depth $U_0 \simeq 1.0\,\mu$K. . . . . 73
Figure 4.4 Spatial profile of measured data and numerical simulation of $\delta n(z,t)$ for the $T/T_F = 0.28$ case at $t = 0.9$ ms, with (b) or without (a) a band-pass filter based on dominant spatial frequencies. In (b), the filter is applied on both the data and the initial condition for the simulation. 75
Figure 4.5 Spatial profile and absolute values of the Fourier transformed spectrum at $t = 0.2$ ms for a $T/T_F = 0.28$ data. Here, q is in unit of cm$^{-1}$ for convenience, since most of our calculations are in the cgs units. . 76
Figure 4.6 A surface plot of $\chi^2$ as function of $\eta$ and $\kappa_T$. Each $\delta n_p(q,t)$ for the $\chi^2$ calculation is obtained by performing the numerical integration for a given set of $\{\eta, \kappa_T\}$ , with $c_T$ fixed. $\chi^2$ shown here is per number of measurement times, which is summed over all the times we take measurements and divided by total number of measured times. . . . 78
Figure 4.7 Evolution of $\delta n(q)$ as function of time, where $T/T_F = 0.28$ and $q = 2\pi/\lambda$, with $\lambda = 23.5\,\mu$m, for the 3 central spatial periods, compared with all 5 spatial periods. Here, $\eta$ is in units of $\hbar\, n_0$ and $\kappa_T$ is in units of $\hbar\, n_0\, k_B/m$. The best fit simulation works for both cases in the first 2.5 ms, and deviates from the 5 periods data after 2.5 ms due to effect of walls. Error bars are statistical (see Sec. 4.3.1). . . . . 80
Figure 4.8 Components of the analytic fit function $\delta n(q,t)$ Eq. 4.13 for a typical data in the middle temperature range of our measurements, where $T/T_F = 0.46$ and $q = 2\pi/\lambda$, with $\lambda = 22.7\,\mu$m. Red curve: Total fit function; Orange curve: Zero frequency, exponentially decaying (thermal diffusion) mode; Blue curve: oscillating, exponentially decaying first sound mode. . . . . 85
Figure 4.9 $T/T_F = 0.28$, $\lambda = 23.5\mu m$. . . . . 89
Figure 4.10 $T/T_F = 0.34$, $\lambda = 23.5\mu m$. . . . . 89
Figure 4.11 $T/T_F = 0.40$, $\lambda = 23.0\mu m$. . . . . 90
Figure 4.12 $T/T_F = 0.46$, $\lambda = 22.7\mu m$. . . . . 90
Figure 4.13 $T/T_F = 0.52$, $\lambda = 23.0\mu m$. . . . . 91

Figure 4.14 $T/T_F = 0.63$, $\lambda = 23.3\mu m$. . . . . 91
Figure 4.15 $T/T_F = 0.56$, with longer wavelength $\lambda = 41.7\mu m$. . . . . 92
Figure 4.16 $T/T_F = 0.37$, with shorter wavelength $\lambda = 18.2\mu m$. . . . . 92
Figure 4.17 Density profiles along the $x$ and $y$ directions of the box potential. The horizontal imaging path is cleaner than the vertical imaging path, where an artificial distortion can be seen. . . . . 95

Figure 5.1 Real part of the Fourier transform of the density perturbation $\delta n(q,t)$ for $q = 2\pi/\lambda$ with $\lambda = 22.7\,\mu$m. The reduced temperature $T/T_F = 0.46$. Blue dots (data); Red curve: Analytic fit of our hydrodynamics model. Inset shows contributions of thermal diffusion (orange exponential) and first sound (blue). The error bars are the standard deviation of the mean of $\delta n(q,t)$ (see Sec. 4.3.1). . . . . 100
Figure 5.2 Shear viscosity $\eta$ in units of $\hbar n$ versus reduced temperature $T/T_F$. Blue dots: $\lambda \simeq 23\,\mu$m. Orange dots: Left (right) $\lambda = 18.2(18.9)\,\mu$m. Pink dots: Left (right) $\lambda = 32.3(41.7)\,\mu$m. Red solid curve: Fit to cloud expansion data, $\alpha_0\,\theta^{3/2} + \alpha_2$, where $\alpha_0 = 2.77, \alpha_2 = 0.25$ [Bluhm et al. 2017]. Shaded region denotes the standard deviation of the fit. Upper purple-dashed curve: Prediction of Enss et al. [2011]. Lower red-dashed curve: High temperature limit, $\alpha_0\,\theta^{3/2}$. Data error bars are statistical (see Sec. 4.3.1). . . . . 102
Figure 5.3 Thermal conductivity $\kappa_T$ in units of $\hbar n\, k_B/m$ versus reduced temperature $T/T_F$. Blue dots: $\lambda \simeq 23\,\mu$m. Orange dots: Left (right) $\lambda = 18.2(18.9)\,\mu$m. Pink dots: Left (right) $\lambda = 32.3(41.7)\,\mu$m. Red-dashed curve: High temperature limit, $15/4\,\alpha_0\,\theta^{3/2}$, where $\alpha_0 = 2.77$. Error bars are statistical (see Sec. 4.3.1). . . . . 104
Figure 5.4 Sound diffusivity $D_1 = 2\,a/q^2$, in units of $\hbar/m$ versus reduced temperature $T/T_F$. Blue dots: $\lambda \simeq 23\,\mu$m. Orange dots: Left (right) $\lambda = 18.2(18.9)\,\mu$m. Pink dots: Left (right) $\lambda = 32.3(41.7)\,\mu$m. Red-dashed curve: Long wavelength, high temperature limit, $D_1 = 7/3\,\alpha_0\,\theta^{3/2}$. Red solid curve: $D_1 = 4/3(\alpha_0\,\theta^{3/2} + \alpha_2) + \alpha_0\,\theta^{3/2}$, where $\alpha_0 = 2.77, \alpha_2 = 0.25$. Error bars are statistical (see Sec. 4.3.1). . . . . 105
Figure 5.5 Sound diffusivity, $D_1 = 2\,a/q^2$, in units of $\hbar/m$ versus reduced temperature $\theta = T/T_F$. Blue, Orange and Pink dots: Current work. Red dots: Patel et al. [2020]. Red-dashed curve: Long wavelength, high temperature limit, $D_1 = 7/3(\alpha_0\,\theta^{3/2})$, where $\alpha_0 = 2.77$. Red solid curve: $D_1 = 4/3(\alpha_0\,\theta^{3/2} + \alpha_2) + (n\,k_B\,T/p)\,\alpha_0\,\theta^{3/2}$. . . . . 109

Figure 5.6 Another comparison of sound diffusivity, $D_1 = 2a/q^2$, in units of $\hbar/m$ versus reduced temperature $\theta = T/T_F$. Blue, Orange and Pink dots: Current work. Red dots: Patel et al. [2020]. Red-dashed curve: Long wavelength, high temperature limit, $D_1 = 7/3(\alpha_0\,\theta^{3/2})$, where $\alpha_0 = 2.77$. Red solid curve: $D_1 = 4/3(\alpha_0\,\theta^{3/2} + \alpha_2) + \alpha_0\,\theta^{3/2}$, with $\alpha_2 = 0.25$. Shaded region denotes the standard deviation of the fit to first term on the right-hand side [Bluhm et al. 2017]. Purple solid curve: $D_1 = 4/3(\alpha_0\,\theta^{3/2} + \alpha_2) + \alpha_0\,\theta^{3/2}$, with $\alpha_2 = 0.95$. . . . . 110

CHAPTER

# 1

# INTRODUCTION

A resonantly interacting or unitary Fermi gas is of special interest, as it is a scale-invariant, strongly interacting quantum many-body system. It is unique in modeling exotic systems, from high temperature superconductors and neutron stars to the quark-gluon plasma that existed microseconds after the Big Bang. Studies in such systems widely connect to different forms of matter across vast energy scales [Adams et al. 2012; Bloch et al. 2012; Strinati et al. 2018], including nuclear physics, astrophysics, condensed matter physics and high energy physics. This system provides test-bed for variety of theories from thermodynamics to string theory.

In unitary Fermi gases, thermodynamic and transport properties are universal functions of the density and temperature, permitting parameter-free comparisons with predictions. However, the behavior of the shear viscosity $\eta$ and the thermal conductivity $\kappa_T$ of a unitary Fermi gas is not yet established.

A normal unitary gas, at temperatures above the superfluid transition $T_c$, is a single component fluid that affords the simplest universal system for hydrodynamic transport measurements, as the transport properties comprise only the shear viscosity $\eta$ and the thermal conductivity $\kappa_T$, since the bulk viscosity $\xi$ vanishes in scale-invariant systems [Son 2007; Hou et al. 2013; Elliott et al. 2014]. Further, measurements in the normal fluid at high

temperature $T$ can be compared with benchmark variational calculations for a unitary gas in the two-body Boltzmann limit [Bruun and Smith 2007; Braby et al. 2010],

$$\eta = \frac{15}{32\sqrt{\pi}} \frac{(m k_B T)^{3/2}}{\hbar^2} \tag{1.1}$$

and

$$\kappa_T = \frac{15}{4} \frac{k_B}{m} \eta, \tag{1.2}$$

with $k_B$ the Boltzmann constant and $m$ the atom mass.

It has been found by experiments [Joseph et al. 2015], that a leading correction to Eqs. 1.1 is required, which is proportional to density $n$ [Bluhm and Schäfer 2016; Bluhm et al. 2017]. This also suggests a density dependent correction to Eq. 1.2. However, before this dissertation, $\eta$ and $\kappa_T$ in the strongly interacting normal fluid regime have never been directly measured independently.

This dissertation presents a new time-domain, free evolution method for measuring hydrodynamic transport coefficients in a normal fluid unitary Fermi gas. The universal thermal conductivity and the universal shear viscosity in the normal fluid regime have been measured independently for the first time.

We create an ultracold ($\sim$ 100 nK) near-homogeneous sample of strongly interacting $^6$Li, confined in a box potential. A periodic spatial profile is initially created in thermal equilibrium by a perturbing potential, Fig. 1.1. After the perturbation is abruptly extinguished, we measure the free decay of the density profile. The dominant spatial Fourier component exhibits an exponentially decaying (thermally diffusive) mode and a decaying oscillatory (first sound) mode, enabling independent measurement of the thermal conductivity and the shear viscosity directly from the time-dependent evolution.

Our new time-domain, free-decay experiments utilize advanced light-crafting techniques. We employ digital micromirror devices (DMDs), containing millions of mirrors in micron size-scale, to project laser light patterns into the $\sim$150 micron long rectangular box, with programmable dynamic control. The laser light used for the DMD projection is reshaped by a "top-hat" beam shaper, achieving a uniform intensity distribution on the desired focal plane, which improves the box trap depth, thus enabling measurements in a wide range of temperatures.

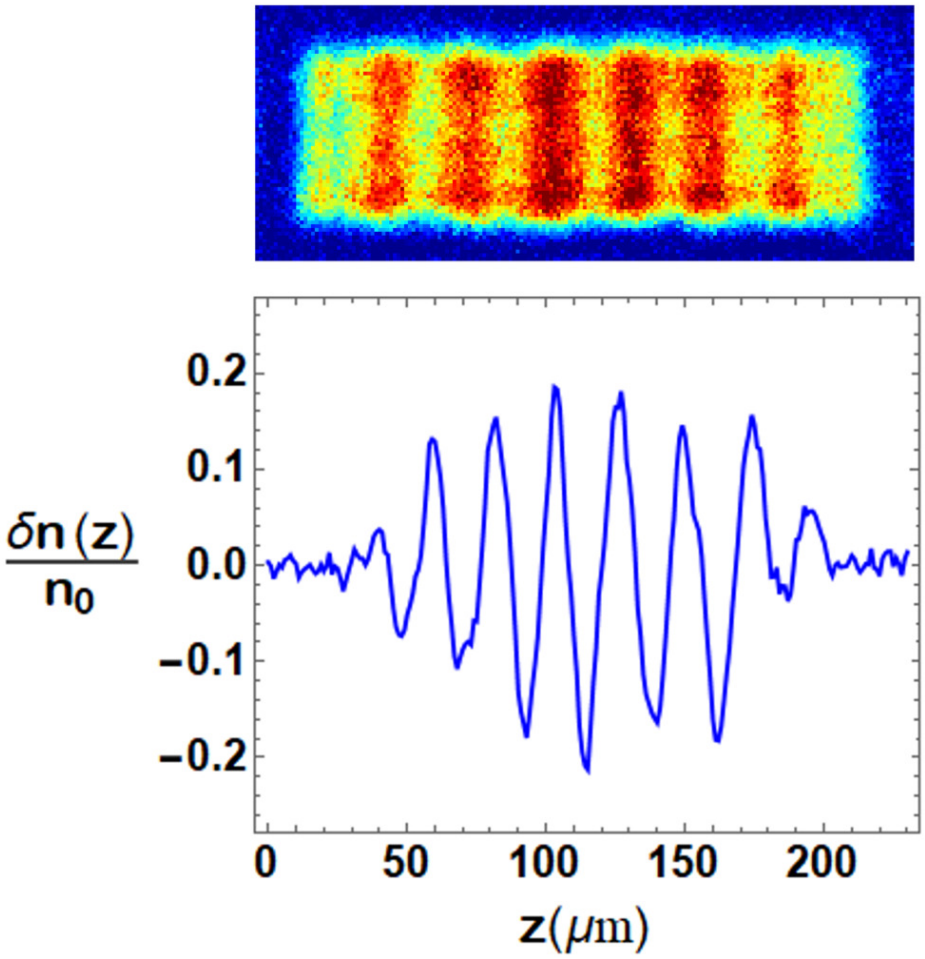


Figure 1.1: A unitary Fermi gas is loaded into a box potential with a small static spatially periodic perturbation $\delta U$, creating a spatially periodic 1D density profile. After $\delta U$ is abruptly extinguished, the dominant Fourier component exhibits a two-mode oscillatory decay (see Fig. 1.6).

## 1.1 Tunable Interactions

Since quantum degeneracy was observed in laboratories [Anderson et al. 1995; Bradley et al. 1995; Davis et al. 1995; DeMarco and Jin 1999] and strongly interacting Fermi gas was produced [O'Hara et al. 2002], a dilute ultra-cold atomic Fermi gas has been a powerful platform for studying quantum many-body physics, in which the interactions are precisely tunable between non-interacting to scale-invariant strongly interacting. This tunability is

accomplished through the existence of a magnetic Feshbach resonance, where a change in the strength of an applied bias magnetic field can produce either strong or weak interactions in the gas, with either an attractive or repulsive potential [Bloch et al. 2008; Ketterle and Zwierlein 2008].

The interaction strength can be quantified by the s-wave scattering length $a_s$. Near a resonating magnetic field, the scattering length is given by [Moerdijk et al. 1995]

$$a_s = a_{bg}\left(1-\frac{\Delta}{B-B_{res}}\right), \tag{1.3}$$

where $a_{bg} = 1582a_0$ is the background scattering length, $\Delta = 262.3G$ is the resonance width and $B_{res} = 832.18G$ [Zürn et al. 2013] is the resonant magnetic field.

Before further explaining how the Feshbach resonances works, we need to know some basic atomic structure for the $^6$Li. $^6$Li, which is a fermion, has 3 protons, 3 neutrons and 3 electrons. Its ground state $2S_{1/2}$ has a nuclear spin of $I = 1$, electronic spin $S = 1/2$ and orbital angular momentum $L = 0$. The total atomic angular momentum then takes the values $F = 1/2,\ 3/2$.

Without the presence of a magnetic field, the $F = 1/2$ level has two states, $m_f = \pm 1/2$; while the $F = 3/2$ level has four states, $m_f = \pm 3/2,\ \pm 1/2$. With the presence of a magnetic field, the atomic levels of $^6$Li further split into six states by the Zeeman interaction, see Fig. 1.2).

The interaction Hamiltonian is given by [Houbiers et al. 1998]:

$$H_{int} = \frac{a_{hf}}{\hbar^2}\boldsymbol{S}\cdot\boldsymbol{I} - \frac{\mu_B}{\hbar}(g_J\boldsymbol{S} + g_I\boldsymbol{I})\cdot\boldsymbol{B}, \tag{1.4}$$

where $a_{hf}/h = 152.14$ MHz is the magnetic dipole constant, $g_J = -2.002$ and $g_I = 0.000448$ [Arimondo et al. 1977]. The eigenstates can be written in $|m_S\ m_I\rangle$ basis, as

$$\begin{aligned}
|1\rangle &= \sin\theta_+\,|1/2\ \ 0\rangle - \cos\theta_+\,|{-1/2}\ \ 1\rangle \\
|2\rangle &= \sin\theta_-\,|1/2\ \ {-1}\rangle - \cos\theta_-\,|{-1/2}\ \ 0\rangle \\
|3\rangle &= |{-1/2}\ \ {-1}\rangle \\
|4\rangle &= \sin\theta_-\,|{-1/2}\ \ 0\rangle + \cos\theta_-\,|1/2\ \ {-1}\rangle \\
|5\rangle &= \sin\theta_+\,|{-1/2}\ \ 1\rangle + \cos\theta_+\,|1/2\ \ 0\rangle \\
|6\rangle &= |1/2\ \ 1\rangle\,,
\end{aligned} \tag{1.5}$$

where $\sin\theta_\pm = 1/\sqrt{1+(Z^\pm+R^\pm)^2/2}$, $Z^\pm = (\mu_n+2\mu_e)B/a_{hf} \pm 1/2$, and $R^\pm = \sqrt{(Z^\pm)^2+2}$. The

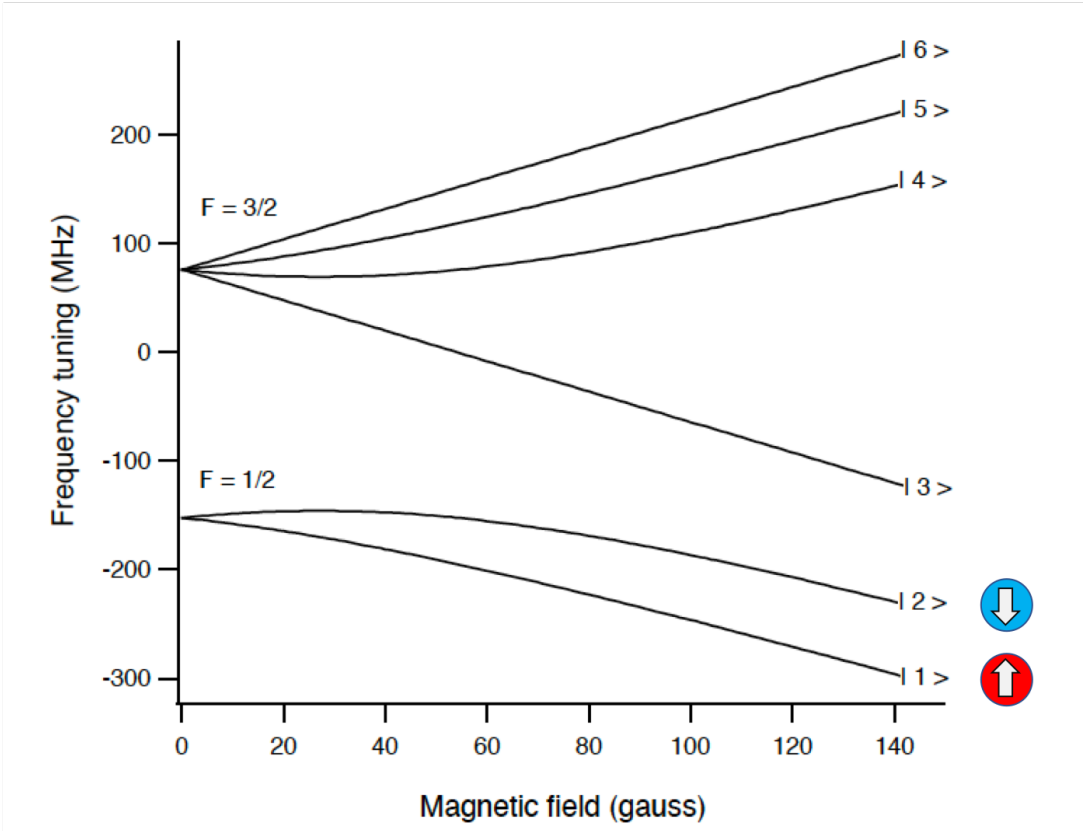


Figure 1.2: Magnetic field dependence of the $2^2S_{1/2}$ ground state of $^6Li$. We use a 50-50 mixture of the two lowest spin states $|1\rangle$(spin up) and $|2\rangle$(spin down) for the experiment. Plot was originally drawn by Kinast [2006].

states are numbered in order of increasing energy, Fig. 1.2.

We use a 50-50 mixture of the lowest ground states $|1\rangle, |2\rangle$ in the experiment. At high field, the $\sin\theta_{\pm}$ term is close to zero and the two lowest states become $|1\rangle = |-1/2 \;\; 1\rangle$ and $|2\rangle = |-1/2 \;\; 0\rangle$, split by $\sim 76$ MHz at a $B \sim 832$ G.

For a $^6$Li-$^6$Li collision, the symmetry of the wavefunction must be taken into consideration. The two particle wavefunction is a product of three terms: the center-of-mass wavefunction (describing where in the trap the collision takes place), the spatial wavefunction (describing the relative position of the atoms), and the spin wavefunction (describing the intrinsic angular momenta of the atoms). Since $^6$Li is a composite fermion, the overall wavefunction must be antisymmetric. The center-of-mass wavefunction is clearly symmetric. As a result, the product of the spatial wavefuncton and spin wavefunction must be antisymmetric.

In an ultracold gas, higher energy collisions are greatly suppressed and the dominant interaction is s-wave scattering. For s-wave collisions of atoms in the $|1\rangle, |2\rangle$ mixture, the total magnetic quantum number $M = 0$ is conserved. In the $|S, m_S; I, m_I\rangle$ basis, where S is the total electronic spin quantum number and I is the total nuclear spin quantum number, there are five states for $M = 0$. The states $|0,0;0,0\rangle$ and $|0,0;2,0\rangle$ are called singlet states, since $S = 0, m_s = 0$. There are also three triplet states $|1,-1;1,1\rangle$, $|1,0;1,0\rangle$ and $|1,1;1,-1\rangle$, with $S = 1, m_s = 1,0,-1$, respectively.

When two atoms approach each other, they effectively reside in attractive potential wells. In the triplet potential, the two atoms with their valence electronic spins are parallel ($S = S_1 + S_2 = 1$), where the spin wavefunction is symmetric, requiring the spatial wavefunction to be antisymmetric. In such case, the electrons are excluded from the region between the nuclei, yielding a shallow potential well. In the singlet potential, however, the two electronic spins are antiparallel ($S = S_1 + S_2 = 0$), where the spin wavefunction is antisymmetric, requiring the spatial wavefunction to be symmetric. The electrons are allowed to sit in the region between the nuclei, and the electrostatic attraction between electrons and nuclei leads to a deep potential well. Here, multiple molecular bound states are allowed in the deep well. In an ultracold $^6$Li-$^6$Li collision, where there are both triplet and singlet potentials, with the presence of a magnetic field, the triplet potential threshold for a $|1\rangle$ - $|2\rangle$ collision is lower than that of the singlet potential threshold. So the triplet potential is energetically accessible as an open channel for the scattering; while the singlet potential is called a closed channel, which is usually not energetically accessible.

However, a magnetic Feshbach resonance occurs when a bias magnetic field tunes the total energy of a colliding atom pair in the open triplet channel into resonance with a molecular bound state in the closed singlet channel [Chin et al. 2010]. Such tuning can be realised since the singlet state ($m_s = 0$) has much smaller energy shift in the bias magnetic field compared to the triplet states with $m_s = -1, 1$, while the nuclear magnetic moment is negligible. The nearest bound state is lower than the triplet state, so the triplet state need to be tuned downward, see Fig. 1.3.

Actually, we can find that the only triplet state that can be tuned down is $|1,-1;1,1\rangle$, since it has $m_s = -1$ and the tunable energy is $-2\mu_B B$, where $\mu_B$=1.4 MHz/G is the Bohr magneton.

Now let us consider what is the change on the scattering length when a resonance between the two channels happens. The collision cross section and the s-wave scattering

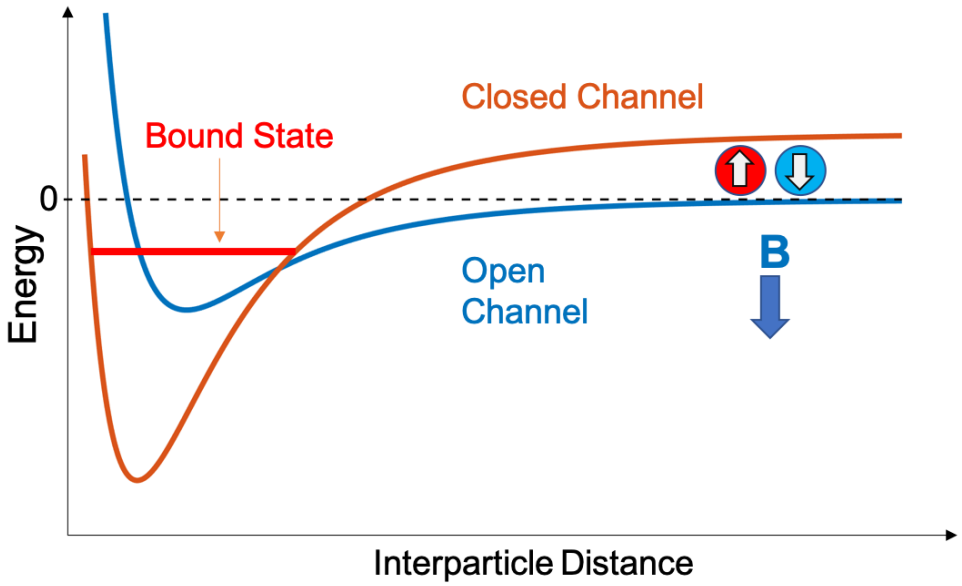


Figure 1.3: Magnetic Feshbach resonance occurs due to the hyperfine coupling between the scattering continuum in the triplet potential (open channel) and the molecular bound state in the singlet potential (closed channel). When $B = B_{res}$, the energy of the triplet state moves downward into resonance with the singlet state.

length are given by [Sakurai and Napolitano 2020]

$$\begin{aligned} \sigma_c &= \frac{4\pi}{k^2}\sin\delta^2 \\ a_s &= -\lim_{k\to 0}\frac{\tan\delta}{k}, \end{aligned} \tag{1.6}$$

where $\sigma_c$ is the total cross section, $a_s$ is the s-wave scattering length, $\delta$ is the scattering phase shift and $k$ is the wavevector. It can be shown from the partial wave approach that the s-wave scattering length diverges when a resonance between bound and unbound states happens, where the phase shift becomes odd number of $\pi/2$, thus $\sin\delta = 1$. Hereby, near the Feshbach resonance, the zero energy ($k = 0$) scattering length rapidly increases.

Fig. 1.4 shows the zero energy s-wave scattering length near the magnetic Feshbach resonance. At the Feshbach resonance $B_{res}$, the scattering length diverges, leading to strong interactions. For magnetic fields below the resonance, the scattering length is positive and interactions are repulsive. This side of the Feshbach resonance is described by Bose-Einstein condensation. Unbound atom pairs with opposite spins can form a BEC of molecules by

inelastic three-body collisions[Jochim et al. 2003; Zwierlein et al. 2004] or an adiabatic ramp across the Feshbach resonance [Greiner et al. 2003; Bourdel et al. 2004]. For magnetic fields above the resonance, the scattering length is negative and interactions are attractive. This side of the resonance can be understood in the famous framework of Bardeen-Cooper-Schrieffer (BCS) theory [Bardeen et al. 1957]. Unbound free atoms can form Cooper pairs with other fermions due to the presence of weak attractions between them.

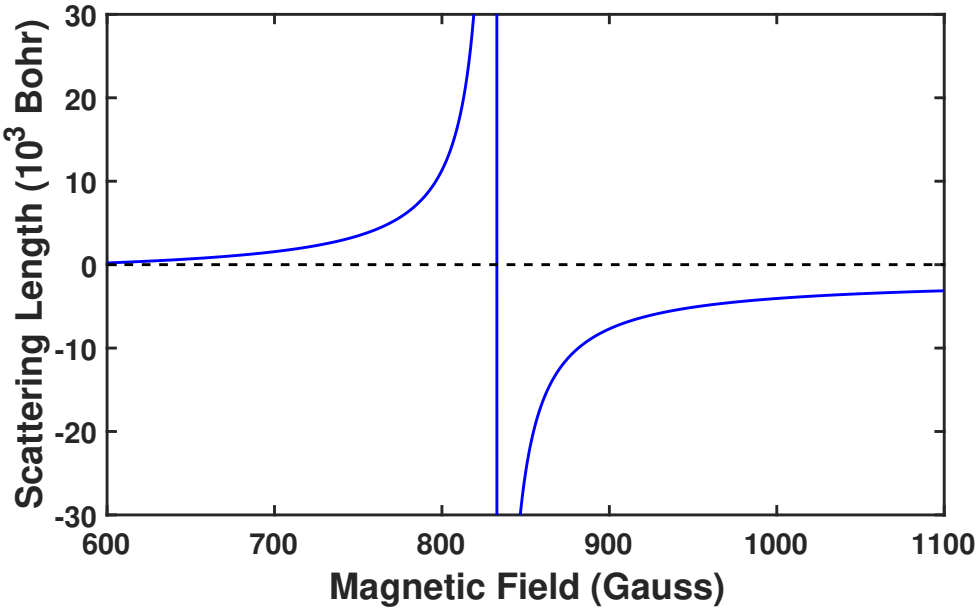


Figure 1.4: The s-wave scattering length $a_s$ near a magnetic Feshbach resonance at $B_{res} = 832.18$ [Zürn et al. 2013]. When $B < B_{res}$, the scattering length is positive and the interactions are repulsive, this regime is called BEC side of the Feshbach resonance. When $B > B_{res}$, the scattering length is negative and interactions are attractive, this regime is called BCS side of the Feshbach resonance. When $B = B_{res}$, the scattering length diverges, yielding strong interactions.

At resonance, the scattering length no longer plays any role in the description of the gas. The only length scales that remain are the thermal De Broglie wavelength $\lambda_T$ and the average distance between the atoms, or inverse Fermi wavevector $L \sim 1/k_F$. Therefore, this scale-invariant region is also called the unitary regime, where the scattering cross section reaches the unitary limit $4\pi/k^2$, with $k = 2\pi/\lambda_T$.

## 1.2 Unitary Fermi Gas

As we mentioned in the previous section, at the Feshbach resonance, the collisional behaviour in such strongly interacting system becomes independent of the scattering length. This system is a scale-invariant unitary Fermi gas. In an unitary Fermi gas, thermodynamic and transport properties are universal functions of the density and temperature [Ho 2004].

Thermodynamics in the unitary Fermi gas has been well established. The pressure $p$ and the energy density $\mathscr{E}$ are functions only of the density and temperature, as required by universality, related by $p = 2\mathscr{E}/3$ [Ho 2004]. Note that this equation relates the pressure and local energy density for the unitary gas in the same way as for an ideal, noninteracting homogeneous gas, although the energy densities are different [Thomas et al. 2005]. Dimensional analysis then shows that the energy density takes the simple form

$$\mathscr{E} = \frac{3}{5} n \, \epsilon_F(n) \, f_E(\theta) \equiv n \, E_1, \tag{1.7}$$

where $E_1$ is the energy per particle and $\theta \equiv T/T_F$ is the reduced temperature with $T_F$ the local Fermi temperature. For a balanced 50-50 mixture of two spin components of total density $n$, the local Fermi energy is

$$\epsilon_F(n) = k_B T_F = \frac{m v_F^2}{2} = \frac{\hbar^2 (3\pi^2 n)^{2/3}}{2m}. \tag{1.8}$$

The universal function $f_E(\theta)$ has been measured by Ku et al. [2012], which determines all of the thermodynamic properties. The pressure is then

$$p = \frac{2}{5} n \, \epsilon_F(n) \, f_E(\theta). \tag{1.9}$$

The entropy density takes a similar form

$$s = n k_B \, f_S(\theta) = n s_1(\theta) \equiv n s_1, \tag{1.10}$$

where $s_1$ is the entropy per particle and $f_S(\theta)$ can be determined from $f_E(\theta)$.

Above are some examples of the thermodynamic properties as universal functions. Other properties, such as the chemical potential $\mu$, will be covered later in this dissertation.

# Hydrodynamics in an Unitary Fermi Gas

A hydrodynamic system can be described by three conserved charges: the mass density $\rho$, the momentum density $\boldsymbol{\pi} = \rho\, \boldsymbol{v}$ and the energy density $\mathscr{E}$ [Schäfer 2014], which obey the conservation laws

$$\partial_t \rho = -\nabla\cdot\boldsymbol{\pi}, \tag{1.11}$$

$$\partial_t \pi_i = -\nabla_j \Pi_{ij}, \tag{1.12}$$

$$\partial_t \mathscr{E} = -\nabla\cdot\mathbf{J}. \tag{1.13}$$

where $\Pi_{ij}$ is the stress tensor and $\mathbf{J}$ is the energy current.

In a simple non-relativistic fluid, rotational symmetry and Galilean invariance require the stress tensor to take the form

$$\Pi_{ij} = \rho\, v_i v_j + p\delta_{ij} + \delta\Pi_{ij} \tag{1.14}$$

where $\boldsymbol{v}$ is the velocity field and $p$ is the pressure. The dissipative term $\delta\Pi_{ij}$ can be expanded to the first order of gradient expansion[1] as

$$\delta\Pi_{ij} = -\eta\,\sigma_{ij} - \xi\,\sigma'_{ij}, \tag{1.15}$$

with $\sigma_{ij} \equiv \partial_i v_j + \partial_j v_i - 2\,\delta_{ij}\nabla\cdot\mathbf{v}/3$ and $\sigma'_{ij} = \delta_{ij}\nabla\cdot\mathbf{v}$. Here, we have two transport coefficients in the expression, namely, the shear viscosity $\eta$ and the bulk viscosity $\xi$.

The energy current $\boldsymbol{J}$ is given by

$$\mathbf{J} = (p+\mathscr{E})\mathbf{v} + \delta\mathbf{J}, \tag{1.16}$$

and the first order gradient expansion is

$$\delta J_i = v_j\delta\Pi_{ij} - \kappa_T\nabla_i T. \tag{1.17}$$

The last term describes the contribution from heat transfer, which gives another transport coefficient, i.e., the thermal conductivity $\kappa_T$.

So far, we have defined the transport coefficients to characterize a hydrodynamic system.

[1] Generally, the gradient expansion is an infinite expansion of the energy-momentum tensor. In fluids dynamics, it is expanded around the perfect fluid in powers of gradients of fluid variables [Chapman et al. 1990; Florkowski et al. 2016]

These coefficients are parameters that have to be extracted from experiment. Actually, the viscosity is determined by the rate of momentum diffusion, and the thermal conductivity is determined by the rate of thermal diffusion.

In an unitary Fermi gas, hydrodynamic transport properties are also universal functions, only depending on density $n$ and temperature $T$, with transport coefficients as parameters that have to be extracted from experiment.

We can express the viscosity in units of $\hbar\, n$,

$$\eta \equiv \alpha_\eta \hbar\, n \tag{1.18}$$

$$\xi \equiv \alpha_\xi \hbar\, n \tag{1.19}$$

and determine $\alpha_\eta, \alpha_\xi$ from the measurements. Similarly, we can express the thermal conductivity in units of $\hbar\, n\, k_B/m$ as

$$\kappa_T \equiv \alpha_\kappa \hbar\, n\, \frac{k_B}{m} \tag{1.20}$$

and determine $\alpha_\kappa$ from the measurements.

The bulk viscosity is related to the changing of the volume and traditionally is considered vanishing for an incompressible flow. Further, it has been proven both theoretically [Son 2007; Hou et al. 2013; Maki and Zhang 2020] and experimentally [Elliott et al. 2014] that in an unitary Fermi gas, the bulk viscosity $\xi$ is zero in the normal fluid regime, while a third component $\xi_3$ can be nonzero in the superfluid regime, which is beyond our purpose in this dissertation.

Although there are plenty of theoretical studies for unitary Fermi gases. These include the behavior of the shear viscosity $\eta$ [Bruun and Smith 2007; Bluhm et al. 2017; Enss et al. 2011; Wlazłowski et al. 2012; Bluhm and Schäfer 2016; Nishida 2019; Hofmann 2020], and the thermal conductivity $\kappa_T$ [Braby et al. 2010; Frank et al. 2020; Zhou and Ma 2021]. However, the transport properties of a unitary Fermi gas are not yet established due to experimental challenges. Measurement of hydrodynamic flow in freely expanding clouds [Cao et al. 2011; Joseph et al. 2015] enables extraction of $\eta$ in the normal fluid regime, but requires a second order hydrodynamics model to properly account for ballistic flow in the dilute edges [Bluhm and Schäfer 2016; Bluhm et al. 2017].

Spectroscopic techniques have also been applied to the study of quantum gases [Vale and Zwierlein 2021]. A recent study on sound modes by two-photon Bragg spectroscopy reveals connection between the damping rate of sound excitation and the shear viscosity just above $T_c$, but it neglects the contribution from thermal conductivity and cannot go fully

into the hydrodynamic regime [Kuhn et al. 2020]. Since the required homogeneous density is realized by tightly focused the Bragg laser on a small region near center of a harmonic trap, the wavelength is too short to investigate hydrodynamic behavior.

## 1.3 Ultracold Gases in Homogeneous Potentials

From the previous subsection we can see a major challenge for studing the transport properties in unitary Fermi gases is that the density is varying in the trap. A proper interpretation of experimental results usually needs some averaging estimations or theoretical corrections.

Ultracold gases have been traditionally produced in harmonic electromagnetic traps and thus had inhomogeneous densities. Recent advances in light shaping technologies pave the way for trapping in flat-bottomed optical box potentials, allowing the creation of homogeneous samples [Navon et al. 2021]. The box potential, which has versatile geometric nature, e.g., rectangle, disk and ring, has been achieved for both Bose and Fermi atomic gases in various dimensionalities [Mukherjee et al. 2017; Ville et al. 2018; Hueck et al. 2018; Tajik et al. 2019; Christodoulou et al. 2021], and even for molecular gases [Bause et al. 2021; Zhang et al. 2021]. The technical advances are utilized by two types of programmable light modulators, i.e., the liquid-crystal spatial light modulators (SLMs) that tune the phase of laser beams and the digital micromirror devices (DMDs) that modulate the amplitudes [Gauthier et al. 2021]. The applications can also involve static light modulators, such as intensity masks and axicons, for their higher power tolerance.

A homogeneous sample in such box traps provides more direct connections with theory. It also allows better quantitative determination of physical properties in experiments.

Recent measurements of the sound diffusivity are obtained by a MIT group [Patel et al. 2020], by observing sound attenuation in a driven, uniform density, unitary Fermi gas. The study constrains $\eta$ and $\kappa_T$, but they are not independently determined [MZT]. The sound diffusivity is also measured in a 2D Fermi gas [Bohlen et al. 2020], but again, $\eta$ and $\kappa_T$ are not independently determined.

Our group started to investigate hydrodynamic transport properties in a box by driving a repulsive periodic optical potential through the uniform sample [Baird et al. 2019], with inspiration from an energy-absorption spectroscopy proposal by Zhang and Yu [2018]. Instead of measuring the energy input, a hydrodynamic linear response model was established to directly analyze the density profile, which allowed us to extract the thermal conductivity $\kappa_T$, assuming a known shear viscosity $\eta$ from the high temperature diluteness expansion fit of

Bluhm et al. [2017] to previous $\eta$ measurements of our group [Joseph et al. 2015]. However, the contributions from $\eta$ and $\kappa_T$ were still not resolved, and only one temperature was used.

Shortly before submission of this dissertation, a study on second sound attenuation in the superfluid regime was reported by Li et al. [2022], in which they successfully extract both $\eta$ and $\kappa_T$. They probe the density response in a uniform sample, using a method similar to the above study of Baird et al. [2019], but employ high-resolution Bragg spectroscopy instead of driving the gas by the DMD. Taking advantage of a very high atom density $n \simeq 1.6 \times 10^{13} c\,m^{-3}$, they are able to suppress the noise and precisely measure the first and second sound attenuations. However, this method is only applicable in the superfluid region for the purpose of determining $\eta$ and $\kappa_T$ independently, since both first and second sound modes are needed for calculating $\eta$ and $\kappa_T$ [Hu et al. 2018]. In contrast, for the normal fluid, only one sound mode exists and the density response spectra cannot distinguish the contributions from the shear viscosity and the thermal conductivity.

## 1.4 Primary Results

The primary results of this dissertation are summarized below. Descriptions of the theoretical model, experimental procedure, data analysis methods and a detailed display and discussion of the results will be covered in the following chapters.

We confine a cloud of $^6$Li atoms in a repulsive box potential, producing a sample of nearly uniform density. A density perturbation is then created by applying a small static optical potential that is spatially periodic along the long axis. After equilibrium is established, the perturbing potential is abruptly extinguished. The atomic gas exhibits an oscillatory decay under the free evolution of hydrodynamic relaxation. Fig. 1.5 shows the false color illustration of the evolution.

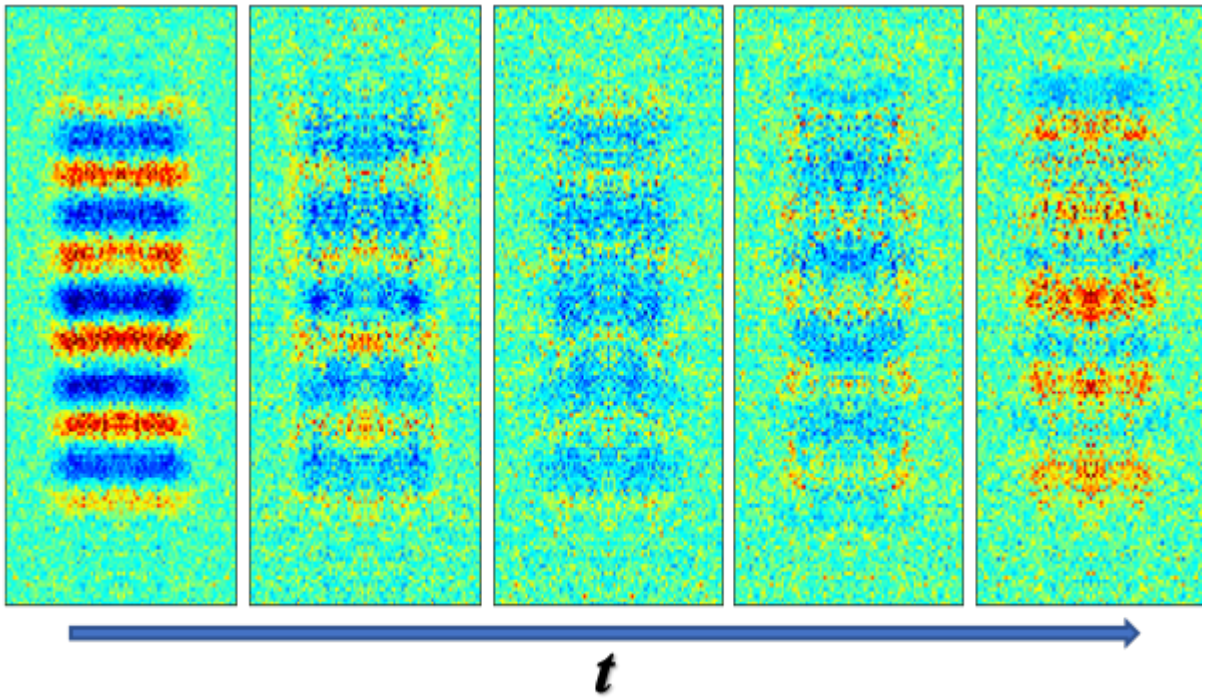


Figure 1.5: Absorption images show the free evolution of the periodic density profile. An oscillatory decay of the ripples is observed.

We measure the time-dependence of the dominant spatial Fourier component of the density, $\delta n(q,t)$, Fig. 1.6, which exhibits an exponentially decaying mode that measures the thermal conductivity and a decaying oscillatory mode that determines the sound speed

and the sound diffusivity.

The data are well fit by a linear hydrodynamics analytic model, as will be discussed in detail in chapter 2,

$$\delta n(q,t) = A_0\, e^{-\Gamma t} + e^{-a\,t}\,[A_1 \cos(b\,t) + A_2 \sin(b\,t)], \tag{1.21}$$

where $A_0, A_1, A_2$ are constrained by initial conditions, and the frequencies $\Gamma$, $a$, and $b$ are related to the isothermal sound frequency $\omega_T$, the adiabatic sound frequency $\omega_S$, and the transport properties $\gamma_\eta \equiv 4\eta\, q^2/(3 n_0 m)$, $\gamma_\kappa \equiv \kappa_T q^2/(n_0 c_{V_1})$, with $c_{V_1}$ the heat capacity per particle at constant volume.

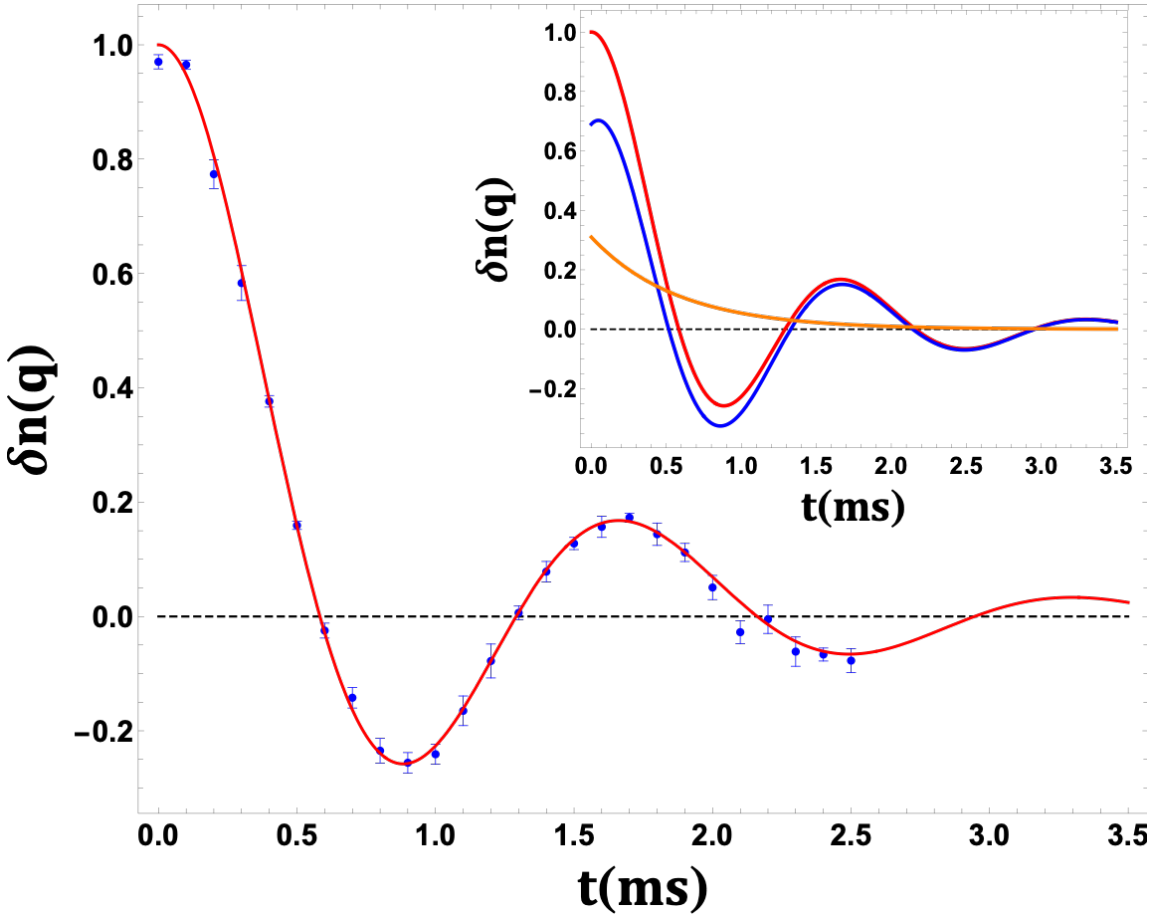


Figure 1.6: Real part of the Fourier transform of the density perturbation $\delta n(q,t)$, normalized to $\delta n(q,0)$, for $q = 2\pi/\lambda$ with $\lambda = 22.7\,\mu$m. The reduced temperature $T/T_F = 0.46$. Blue dots: data; Red curve: analytic hydrodynamics model, Eq. 1.21. Inset shows contributions of thermal diffusion (orange) and first sound (blue). The error bars are statistical.

From the fit, we can determine the shear viscosity $\eta$, the thermal conductivity $\kappa_T$, and also the reduced temperature $T/T_F$ in-situ.

For reduced temperatures $T/T_F > 0.45$, we find that the shear viscosity measured by this free hydrodynamic relaxation in the box is consistent with that extracted from data on expanding clouds Bluhm and Schäfer [2016]; Bluhm et al. [2017], which includes a significant density-dependent contribution. At lower temperatures, $T/T_F < 0.4$, the shear viscosity measured in the box is consistently larger than that of the expanding cloud. The thermal conductivity for $T/T_F > 0.45$ is close to the high temperature limit. In contrast to the shear viscosity, the pure density dependent contribution to the high temperature thermal conductivity appears to be quite small.

These results emphasize the need for rigorous calculations of the leading density-dependent corrections to the two-body high temperature limits. The measured sound diffusivity is self-consistent with a damped oscillator interpretation. Our data can be compared to that of Patel et al. [2020], which is shifted upward relative to ours, but exhibits nearly identical scaling with $T/T_F$ and appears to converge at low temperatures. Figures of all these results are provided in chapter 5.

## 1.5 Significance of Current Work

We have developed a new time-domain, free evolution method for measuring hydrodynamic transport coefficients in a normal fluid unitary Fermi gas. The thermal conductivity and the shear viscosity in a universal normal fluid have been measured independently for the first time.

Confined in a box potential, the dominant spatial Fourier component of a sinusoidal density profile exhibits an exponentially decaying (thermally diffusive) mode and a decaying oscillatory (first sound) mode after the extinguishing of an initial perturbation, enabling independent measurement of the thermal conductivity $\kappa_T$ and the shear viscosity $\eta$ directly from the time-dependent evolution.

The two-mode oscillatory decay of a spatially periodic density perturbation are well-distinguished. For the isothermal static initial conditions employed in the experiments, the thermally diffusive mode comprises $\simeq 32\%$ of the initial total amplitude of the dominant Fourier component, which is readily apparent in the free hydrodynamic relaxation.

This method is complementary to frequency domain techniques, where transport properties of quantum fluids have been determined by measuring the hydrodynamic

linear susceptibility Hohenberg and Martin [1965]; Hu et al. [2018]; Zhang and Yu [2018]; Mukherjee et al. [2019].

Prior to our work, it was not obvious that simply measuring the hydrodynamic decay of a periodic density perturbation, created in a box potential, would enable a clear separation of the contributions of a zero frequency, thermally diffusive mode and an oscillating first sound mode in a normal fluid unitary Fermi gas.

Of particular importance is that our data emphasize the need for rigorous calculations of the leading purely density-dependent corrections to the two-body high temperature limits of the transport coefficients.

## 1.6 Dissertation Organization

In the chapter 2, I will introduce the basic theory of thermodynamics, including unique features for a unitary Fermi gas. Followed by a hydrodynamic linear response model and the analytic solution to the equations in Fourier space, which we use to fit our data. The two mode picture for both the density change and the temperature change over time is discussed here. A damped oscillator model will also be discussed to illustrate the free evolution of the density profile for the atomic gas.

In chapter 3, I will describe the experimental apparatus in our laboratory for creating, cooling, trapping, modulating and watching the $^6$Li atomic gas. I will discuss challenges in previous experimental setup and focus on the new techniques for realizing the box potential and the method to create perturbations.

In chapter 4, I will provide four data analysis methods, starting with data taking and processing procedures. These methods were gradually developed during the research. We start from a straight-forward numerical integration of the hydrodynamic linear response equations. Then as our understanding of the experiment deepens, an analytic model is established, clearly interpreting the two mode physics. Examples of our fit to different data are presented in Sec. 4.2.4, so the readers can see how good our fits are. The calculation of statistical errors and a discussion on the central density will also be covered in this chapter.

In chapter 5, I will present the main results of this dissertation, which are the measurements of the shear viscosity $\eta$, the thermal conductivity $\kappa_T$ and the sound diffudivity $D_1$, following by comparison with existing theoretical prediction and previous experiments. We will also evaluate the consistency of our measured results and estimate systematic errors. Last, a brief discussion about the breakdown of hydrodynamics will be provided to

stimulate further studies on the transport properties, including possible corrections to our measurements.

Finally, in chapter 6, I will briefly summarize this dissertation and provide outlook for future studies.

CHAPTER

# 2

# THEORY

In this chapter, we provide the thermodynamic and hydrodynamic theories we need to describe the evolution of the atomic gas in the box potential. The derivations lead to a hydrodynamic linear response model, with necessary thermodynamic relations, which we use to extract the shear viscosity $\eta$, the thermal conductivity $\kappa_T$ and the first sound diffusivity $D_1$, and to determine the temperature in-situ.

## 2.1 Thermodynamic Theory

Before we derive the hydrodynamic linear response model for the normal fluid regime, we derive the elementary thermodynamic relations that appear in our hydrodynamic model.

### 2.1.1 Thermodynamic Relations

Defining the density $n = 1/V_1$ in terms of the volume per particle $V_1$, the expansivity is

$$\beta \equiv \frac{1}{V_1}\left(\frac{\partial V_1}{\partial T}\right)_p = -\frac{1}{n}\left(\frac{\partial n}{\partial T}\right)_p, \tag{2.1}$$

which has a dimension of inverse temperature.

The isothermal sound speed $c_T$ is defined by

$$m\,c_T^2 = \left(\frac{\partial p}{\partial n}\right)_T = -\left(\frac{\partial p}{\partial T}\right)_n \left(\frac{\partial T}{\partial n}\right)_p, \tag{2.2}$$

where we have used the chain rule. Similarly, the adiabatic sound speed $c_S$ is defined by

$$m\,c_S^2 = \left(\frac{\partial p}{\partial n}\right)_{s_1} = -\left(\frac{\partial p}{\partial s_1}\right)_n \left(\frac{\partial s_1}{\partial n}\right)_p, \tag{2.3}$$

where we have defined $s_1$ as the entropy per particle.

Taking the ratio of Eqs. 2.2 and 2.3, and using $(\partial T/\partial n)_p = 1/(\partial n/\partial T)_p$ and $1/(\partial p/\partial s_1)_n = (\partial s_1/\partial p)_n$, we obtain the well-known relation

$$\frac{c_T^2}{c_S^2} = \frac{\left(\frac{\partial s_1}{\partial p}\right)_n \left(\frac{\partial p}{\partial T}\right)_n}{\left(\frac{\partial s_1}{\partial n}\right)_p \left(\frac{\partial n}{\partial T}\right)_p} = \frac{\left(\frac{\partial s_1}{\partial T}\right)_n}{\left(\frac{\partial s_1}{\partial T}\right)_p} = \frac{c_{V_1}}{c_{P_1}}, \tag{2.4}$$

where $c_{V_1} = T(\partial s_1/\partial T)_n$ and $c_{P_1} = T(\partial s_1/\partial T)_p$ are the heat capacities per particle at constant volume and at constant pressure, respectively.

Next, we find the first order pressure change, $\delta p$, which is needed later in eq. 2.32. We have

$$\delta p = \left(\frac{\partial p}{\partial n}\right)_T \delta n + \left(\frac{\partial p}{\partial T}\right)_n \delta T = \left(\frac{\partial p}{\partial n}\right)_T \left[\delta n + \left(\frac{\partial n}{\partial p}\right)_T \left(\frac{\partial p}{\partial T}\right)_n \delta T\right]. \tag{2.5}$$

The chain rule gives

$$\left(\frac{\partial n}{\partial p}\right)_T \left(\frac{\partial p}{\partial T}\right)_n = -\left(\frac{\partial n}{\partial T}\right)_p = \beta n, \tag{2.6}$$

where we have used Eq. 2.1 for the expansivity $\beta$. With Eqs. 2.5 and 2.2,

$$\delta p = m\,c_T^2(\delta n + \delta \tilde{T}), \tag{2.7}$$

where we have defined

$$\delta \tilde{T} \equiv \beta\, n\, \delta T, \tag{2.8}$$

which has a dimension of density.

For the first order temperature change, we have

$$\delta T = \left(\frac{\partial T}{\partial n}\right)_{s_1} \delta n + \left(\frac{\partial T}{\partial s_1}\right)_n \delta s_1 = \left(\frac{\partial T}{\partial s_1}\right)_n \left[\left(\frac{\partial s_1}{\partial T}\right)_n \left(\frac{\partial T}{\partial n}\right)_{s_1} \delta n + \delta s_1\right]. \tag{2.9}$$

The chain rule gives

$$\left(\frac{\partial s_1}{\partial T}\right)_n\left(\frac{\partial T}{\partial n}\right)_{s_1} = -\left(\frac{\partial s_1}{\partial n}\right)_T, \tag{2.10}$$

which we evaluate as follows. Consider $s_1[T, n(T,p)]$. Then,

$$c_{P_1} = T\left(\frac{\partial s_1}{\partial T}\right)_p = T\left(\frac{\partial s_1}{\partial T}\right)_n + T\left(\frac{\partial s_1}{\partial n}\right)_T\left(\frac{\partial n}{\partial T}\right)_p = c_{V_1} - \beta\, n\, T\left(\frac{\partial s_1}{\partial n}\right)_T, \tag{2.11}$$

where we have used Eq. 2.1. Hence,

$$\left(\frac{\partial s_1}{\partial n}\right)_T = -\frac{c_{P1} - c_{V1}}{\beta\, n\, T}. \tag{2.12}$$

With $(\partial T/\partial s_1)_n = T/c_{V_1}$ and Eq. 2.10, Eq. 2.9 takes the simple form,

$$\delta T = \left(\frac{c_{P_1}}{c_{V_1}} - 1\right)\frac{\delta n}{\beta\, n} + \frac{T\,\delta s_1}{c_{V_1}}. \tag{2.13}$$

Here, the first term is the adiabatic change in the temperature arising from the change in density. For a monatomic gas in the high temperature limit, Eq. 2.1 with $n = p/(k_B T)$ gives $\beta \to 1/T$ and $c_{P1}/c_{V1} - 1 \to 2/3$. Then, $\delta T/T = 2/3\,\delta n/n$, i.e., $T/T_0 = (n/n_0)^{2/3}$ as expected. For a unitary Fermi gas, where $s_1 = k_B f_S(\theta)$, see Eq. 2.17 below, this result holds at all temperatures, since $(\partial T/\partial n)_{s_1} = (\partial T/\partial n)_\theta$, with $T = \theta\, T_F$, and $T_F \propto n^{2/3}$. The second term is the temperature change arising from the heat flow per particle, $T\,\delta s_1 = \delta q_1$.

### 2.1.2 Unitary Fermi Gas Thermodynamics

For the unitary Fermi gas, universality [Ho 2004] requires that the pressure $p$ and the energy density $\mathscr{E}$ are functions only of the density and temperature, related by $p = 2\,\mathscr{E}/3$. Dimensional analysis then shows that the energy density takes the simple form

$$\mathscr{E} = \frac{3}{5} n\, \epsilon_F(n)\, f_E(\theta) \equiv n\, E_1, \tag{2.14}$$

where $E_1$ is the energy per particle and $\theta \equiv T/T_F$ is the reduced temperature with $T_F$ the local Fermi temperature. For a balanced 50-50 mixture of two spin components of total density $n$, the local Fermi energy is

$$\epsilon_F(n) \equiv k_B T_F = m v_F^2/2 = \hbar^2(3\pi^2 n)^{2/3}/(2m). \tag{2.15}$$

The universal function $f_E(\theta)$ has been measured by Ref. Ku et al. [2012], which determines all of the thermodynamic properties. The pressure $p = (2/3)\mathscr{E}$ is then

$$p = \frac{2}{5} n \epsilon_F(n) f_E(\theta). \tag{2.16}$$

The entropy density takes a similar form

$$s = n k_B f_S(\theta) = n s_1(\theta) \equiv n s_1, \tag{2.17}$$

where $s_1$ is the entropy per particle and $f_S(\theta)$ can be determined from $f_E(\theta)$.

The adiabatic sound speed Eq. 2.3 is easily obtained from Eq. 2.16, as Eq. 2.17 requires constant $\theta$ for constant $s_1$,

$$m c_S^2 = \left(\frac{\partial p}{\partial n}\right)_\theta = \frac{2}{3} \epsilon_F(n) f_E(\theta) = \frac{10}{9} E_1, \tag{2.18}$$

where the last form on the right follows from Eq. 2.14.

With $\epsilon_F(n) = m v_F^2/2$, Eq. 2.18 yields

$$c_S^2 = \frac{v_F^2}{3} f_E(\theta). \tag{2.19}$$

The isothermal sound speed, Eq. 2.2, is easily determined from Eq. 2.16, with $p = p[n, \theta(n,T)]$,

$$c_T^2 = \frac{1}{m}\left(\frac{\partial p}{\partial n}\right)_T = \frac{v_F^2}{3}\left[f_E(\theta) - \frac{2}{5}\theta f_E'(\theta)\right]. \tag{2.20}$$

where the $\partial_\theta f_E(\theta) \equiv f_E'(\theta)$.

Eqs. 2.19 and 2.20 yield $c_S(\theta), c_T(\theta)$ from $f_E(\theta)$. Fig. 2.1 shows that for $\theta > 0.25$, $\theta$ monotonically increases with $\tilde{c}_S \equiv c_S/v_F$ and $\tilde{c}_T \equiv c_T/v_F$, as measured by Ref. [Ku et al. 2012]. Eqs. 2.19 and 2.20 can be used as a thermometer to determine $\theta$ from $\tilde{c}_S$ and $\tilde{c}_T$, respectively.

In practice, we use a fit with a cubic polynomial to $\theta(c_S/v_F)$ and $\theta(c_T/v_F)$, which as shown in Figs. 2.1.

The heat capacity per particle at constant volume takes a simple form. Using Eq. 2.14,

$$c_{V_1} = T\left(\frac{\partial s_1}{\partial T}\right)_n = \left(\frac{\partial E_1}{\partial T}\right)_n = \frac{3}{5} k_B f_E'(\theta). \tag{2.21}$$

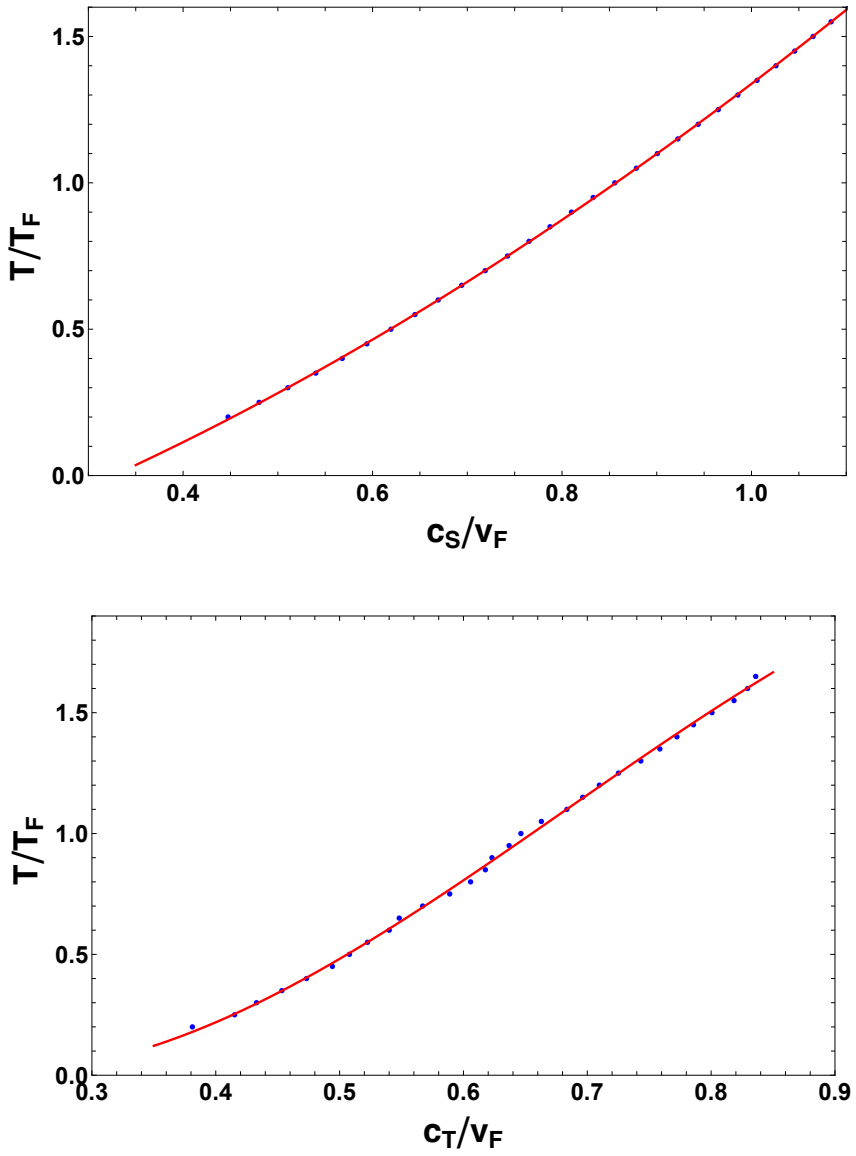


Figure 2.1: Reduced temperature $\theta = T/T_F$ versus adiabatic sound speed $\tilde{c}_S \equiv c_S/v_F$ and isothermal sound speed $\tilde{c}_T \equiv c_T/v_F$. For $\theta > 0.25$, $\theta$ monotonically increases with $\tilde{c}_S$ ($\tilde{c}_T$), showing that the fitted $\tilde{c}_S$ ($\tilde{c}_T$) can be used as a thermometer to determine $\theta$ in the normal fluid region. The blue dots are obtained from the equation of state of Ref. Ku et al. [2012]. The upper (lower) red solid curve shows a fit with a cubic polynomial, $\theta(\tilde{c}_S) = -0.399 + 0.958\,\tilde{c}_T + 0.839\,\tilde{c}_T^2 - 0.059\,\tilde{c}_T^3$, $\theta(\tilde{c}_T) = 0.478 - 4.410\,\tilde{c}_T + 11.688\,\tilde{c}_T^2 - 5.711\,\tilde{c}_T^3$.

Eq. 2.4 then determines $c_{P_1}$ from the ratio $c_{P_1}/c_{V_1} = c_S^2/c_T^2$ using Eqs. 2.19 and 2.20,

$$c_{P_1} = \frac{f_E(\theta)}{f_E(\theta) - \frac{2}{5}\theta\, f_E'(\theta)}\, c_{V_1}. \tag{2.22}$$

Similarly, we use quartic polynomials to fit $c_{V_1}$ and $c_{P_1}$[1], see Fig. 2.2.

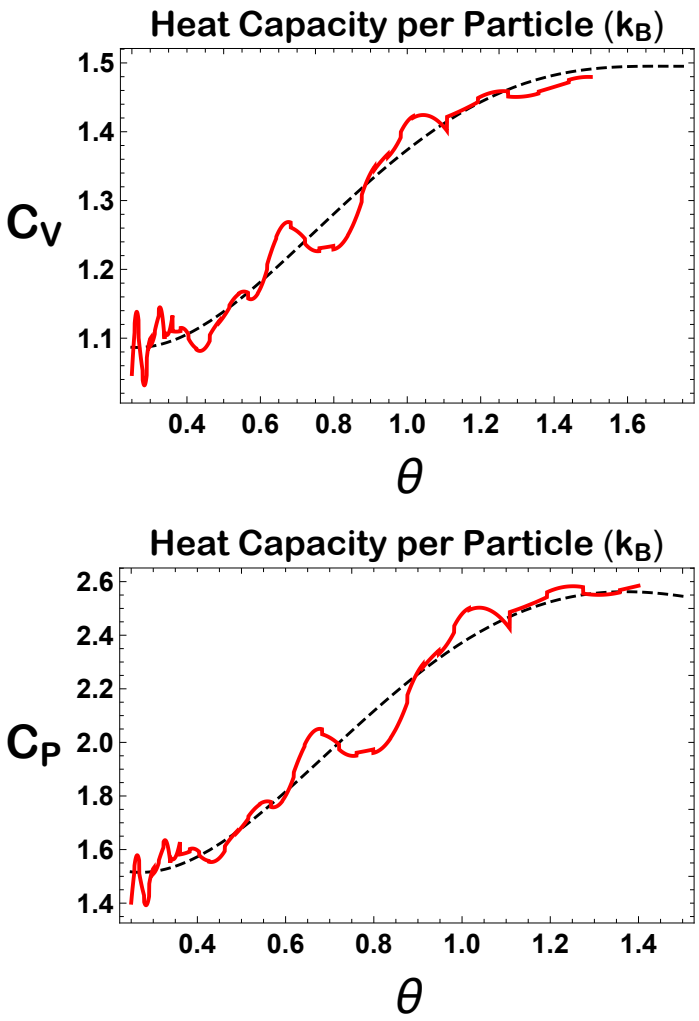


Figure 2.2: Reduced temperature $\theta = T/T_F$ versus the heat capacities per particle at constant volume $c_{V_1}$ and at constant pressure $c_{P_1}$. The red lines are obtained from interpolations of the equation of state of Ref. Ku et al. [2012]. The upper (lower) black dashed curve shows the fit with a quartic polynomial, $c_{V_1} = 1.190 - 0.872\,\theta + 2.160\,\theta^2 - 1.387\,\theta^3 + 0.283\,\theta^4$ ($c_{P_1} = 1.904 - 3.223\,\theta + 7.998\,\theta^2 - 5.500\,\theta^3 + 1.194\,\theta^4$).

[1]We fit the smoothly varying part of $c_{V_1}$ and $c_{P_1}$ by limiting the $\theta$ range from 0.25 to 2. For $\theta = 0.25 \sim 1.5$, we use interpolations of the measurements by Ku et al. [2012]; for $\theta = 1.5 \sim 2$, we use high temperature limits, i.e., 3/2 for $c_{V_1}$ and 5/2 for $c_{P_1}$

Finally, Eqs. 2.21 and 2.22 determine

$$\frac{1}{c_{V_1}} - \frac{1}{c_{P_1}} = \frac{1}{k_B}\frac{2}{3}\frac{\theta}{f_E(\theta)}, \tag{2.23}$$

which appears later in the sound diffusivity Eq. 2.66. With Eqs. 2.15 and 2.16, Eq. 2.23 can also take the form [Ku et al. 2012]

$$\frac{1}{c_{V_1}} - \frac{1}{c_{P_1}} = \frac{4}{15}\frac{nT}{p}, \tag{2.24}$$

with $(5/2)\,\theta / f_E(\theta) = n\,k_B T/p$.

It is also useful to derive the confining potential in a trap from chemical potential $\mu$. We find the force arising from the confining potential along one axis $z$, using a measured density profiles $n_0(z)$. The trapping potential is easily found in the local density approximation from the local chemical potential, $\mu(z)$, where $\mu(z) + U_0(z) = \mu_G$, with $\mu_G$ the global chemical potential. Then,

$$U_0(z) = \mu_G - \mu(z) = \mu_G - \epsilon_F[n_0(z)]\, f_\mu[\theta(z)]. \tag{2.25}$$

Here, $f_\mu(\theta)$ is a dimensionless universal function of the reduced temperature $\theta$, which determines $\mu(n,\theta)$ in terms of the local Fermi energy $\epsilon_F(n)$. $f_\mu(\theta)$ has been precisely measured Ku et al. [2012]. The reduced temperature $\theta(z) = T_0/T_F(n) = \theta_0/[\tilde{n}_0(z)]^{2/3}$, where we determine $\theta_0 = T_0/T_F(n_0)$ from the fitted isothermal sound speed $c_T$ and $\tilde{n}_0(z) = n_0(z)/n_0$, with $n_0$ the central density, which occurs at $z \equiv z_{\max}$. The global chemical potential is then $\mu_G = \epsilon_F(n_0)\, f_\mu(\theta_0)$, so that $U_0(z_{\max}) = 0$ by construction. It is convenient to find $\tilde{U}_0(z) = U_0(z)/\epsilon_F(n_0)$, with $\tilde{\mu}_G = f_\mu(\theta_0)$. Then,

$$\tilde{U}_0(z) = f_\mu(\theta_0) - [\tilde{n}_0(z)]^{2/3}\, f_\mu\big(\theta_0/[\tilde{n}_0(z)]^{2/3}\big). \tag{2.26}$$

## 2.2 Hydrodynamic Theory

We consider a normal fluid Fermi gas, which is a single component fluid with a mass density $\rho \equiv n\,m$, where $n$ is the total particle density (we assume a 50-50 mixture of two spin components) and $m$ is the atom mass. $\rho(\mathbf{r}, t)$ satisfies the continuity equation,

$$\partial_t \rho + \partial_i(\rho\, v_i) = 0, \tag{2.27}$$

where a sum over $i = x, y, z$ is implied. The mass flux (momentum density) is $\rho\, v_i$, with $v_i(\mathbf{r}, t)$ the velocity field.

The momentum density and corresponding momentum flux $\rho\, v_i v_j$ obey [Landau and Lifshitz 1959]

$$\partial_t(\rho\, v_i) + \partial_j(\rho\, v_i v_j) = -\partial_i p - n\,\partial_i U + \partial_j(\eta\,\sigma_{ij} + \xi_B\,\sigma'_{ij}), \tag{2.28}$$

Here, $-\partial_i p - n\,\partial_i U$ is the force per unit volume arising from the pressure $p$ and the externally applied potential $U(\mathbf{r}, t)$. The last terms describe the dissipative forces, which arise generally from the shear viscosity $\eta$ and the bulk viscosity $\xi_B$, with $\sigma_{ij} \equiv \partial_i v_j + \partial_j v_i - 2\,\delta_{ij}\nabla\cdot\mathbf{v}/3$ and $\sigma'_{ij} = \delta_{ij}\nabla\cdot\mathbf{v}$. For generality, we retain $\xi_B$, which vanishes for a unitary gas [Son 2007; Hou et al. 2013; Elliott et al. 2014].

Taking the divergence of Eq. 2.28, and using Eq. 2.27, we obtain

$$-\partial_t^2\rho + \partial_i\partial_j(\rho\, v_i v_j) = -\partial_i^2 p - \partial_i(n\,\partial_i U) + \partial_i\partial_j(\eta\,\sigma_{ij} + \xi_B\,\sigma'_{ij}). \tag{2.29}$$

### 2.2.1 Hydrodynamic Linear Response

We are interested in the hydrodynamic linear response to a perturbing external potential $\delta U(\mathbf{r}, t)$, which leads to first order changes in the density $\delta n(\mathbf{r}, t)$ and pressure $\delta p(\mathbf{r}, t)$,

$$\begin{aligned} n(\mathbf{r}, t) &= n_0(\mathbf{r}) + \delta n(\mathbf{r}, t) \\ p(\mathbf{r}, t) &= p_0(\mathbf{r}) + \delta p(\mathbf{r}, t) \\ U(\mathbf{r}, t) &= U_0(\mathbf{r}) + \delta U(\mathbf{r}, t). \end{aligned} \tag{2.30}$$

Here, $n_0(\mathbf{r})$ and $p_0(\mathbf{r})$ are the equilibrium (time independent) density and pressure arising from confinement in the box trap potential, $U_0(\mathbf{r})$. In equilibrium, the velocity field $\mathbf{v}_0(\mathbf{r}, t) = 0$ and Eq. 2.28 requires balance of the forces per unit volume arising from the box trap and the pressure,

$$-\nabla p_0(\mathbf{r}) - n_0(\mathbf{r})\nabla U_0(\mathbf{r}) = 0. \tag{2.31}$$

Substituting Eqs. 2.30 and 2.31 into Eq. 2.29 and retaining terms to first order in small quantities, we obtain

$$\partial_t^2\delta n = \frac{1}{m}\nabla^2\,\delta p + \frac{1}{m}\nabla\cdot[n_0(\mathbf{r})\nabla\delta U + \delta n\,\nabla U_0] - \frac{1}{m}\partial_i\partial_j(\eta\,\sigma_{ij} + \xi_B\,\sigma'_{ij}). \tag{2.32}$$

Here, the second term on the left side of Eq. 2.29 is negligible, as the velocity field is first order in small quantities, and we also neglect $\delta n \nabla \delta U$, which is also second order in small quantities.

To evaluate the last term in Eq. 2.32, we assume that the dissipative forces are small compared to the conservative forces and that the density $n_0$ slowly varies in the region of interest. Then we can ignore the spatial derivatives of $\eta$, $\xi_B$, and $n_0$, yielding

$$\partial_i \partial_j (\eta \sigma_{ij} + \xi_B \sigma'_{ij}) \simeq \eta \partial_i \partial_j \sigma_{ij} + \xi_B \partial_i \partial_j \sigma'_{ij} \simeq \left( \frac{4}{3} \eta + \xi_B \right) \nabla^2 (\nabla \cdot \mathbf{v}). \tag{2.33}$$

The velocity field is eliminated using $\nabla \cdot \mathbf{v} \simeq -\partial_t \delta n / n_0 = -\delta \dot{n} / n_0$, which follows from Eq. 2.27. With Eq. 2.7, $\delta p = m c_T^2 (\delta n + \delta \tilde{T})$, Eq. 2.32 becomes

$$\delta \ddot{n} = c_T^2 \nabla^2 (\delta n + \delta \tilde{T}) + \frac{1}{m} \nabla \cdot [n_0(\mathbf{r}) \nabla \delta U + \delta n \nabla U_0] + \frac{\frac{4}{3}\eta + \xi_B}{n_0 m} \nabla^2 \delta \dot{n}, \tag{2.34}$$

where $\delta \tilde{T} \equiv \beta\, n\, \delta T$, from Eq. 2.8.

To complete the model, we require the evolution equation for $\delta \tilde{T}$, which is determined from Eq. 2.13,

$$\delta \dot{T} = \epsilon_{LP} \frac{\delta \dot{n}}{\beta\, n} + \frac{T \delta \dot{s}_1}{c_{V_1}}. \tag{2.35}$$

Here, $\epsilon_{LP} \equiv c_{P_1} / c_{V_1} - 1$ the Landau-Placzek parameter, $T = T_0$ is the initial, spatially-uniform, temperature and $n = n_0$ is the initial spatially-uniform density.

The heating rate per particle, $T \delta \dot{s}_1$ is determined to first order in small quantities by

$$T\, \delta \dot{s}_1 = T\, (\partial_t + \mathbf{v} \cdot \nabla)\, \delta s_1 = \frac{\delta \dot{q}}{n_0}, \tag{2.36}$$

where $\delta \dot{q}$ is the heating rate per unit volume. The heating rate arising from the shear viscosity is second order in $v_i$, which is negligible compared to the heating rate arising from heat conduction. Hence, $\delta \dot{q} \simeq -\nabla \cdot (-\kappa_T \nabla \delta T) \simeq \kappa_T \nabla^2 \delta T$, where we neglect the spatial derivatives of $\kappa_T$ and

$$\delta \dot{T} = \epsilon_{LP} \frac{\delta \dot{n}}{\beta\, n} + \frac{\kappa_T}{n_0 c_{V1}} \nabla^2 \delta T. \tag{2.37}$$

Multiplying Eq. 2.37 by $\beta\, n$, we obtain finally

$$\delta \dot{\tilde{T}} = \epsilon_{LP}\, \delta \dot{n} + \frac{\kappa_T}{n_0 c_{V1}} \nabla^2 \delta \tilde{T}. \tag{2.38}$$

Note that by defining $\delta\tilde{T} \equiv \beta\, n\, \delta T$, the temperature terms have units of density, enabling direct comparison with the density perturbation.

Eqs. 2.34 and 2.38 have simple physical interpretations. The $c_T^2$ terms on the right-hand side of Eq. 2.34 correspond to the pressure change. A viscous damping force arises from the shear viscosity, $\eta \equiv \alpha_\eta \hbar n_0$, while the bulk viscosity $\xi_B$ vanishes for a unitary Fermi gas. The final terms in Eq. 2.39 arise from the perturbing and box potentials, where $\partial_z U_0(z)$ is found from the slowly varying background density $n_0(z)$ and $\delta U(z, t > 0) = 0$ for our experiments. The first term on the right-hand side of Eq. 2.38 describes the adiabatic change in the temperature due to the change in density. The last term describes temperature relaxation at constant density due to the heat flux, which is proportional to the thermal conductivity $\kappa_T \equiv \alpha_\kappa \hbar n_0 k_B/m$.

Together, Eqs. 2.34 and 2.38 determine the evolution for the given forces $\nabla U_0$ and $\nabla\delta U$, with the initial conditions $\delta n(z,0)$ (measured), $\delta\dot{n}(z,0) = 0$, and $\delta\tilde{T}(z,0) = 0$.

### 2.2.2 Analytic Solution in Fourier Space

For our experiments, we employ a one-dimensional approximation, where the only spatial dependence is $z$. So $\nabla \Rightarrow \partial_z$. Eqs. 2.34 and 2.38 then become

$$\delta\ddot{n} = c_T^2\,\partial_z^2(\delta n + \delta\tilde{T}) + \frac{1}{m}\partial_z \cdot [n_0(z)\,\partial_z \delta U + \delta n\,\partial_z U_0] + \frac{\frac{4}{3}\eta + \xi_B}{n_0 m}\,\partial_z^2 \delta\dot{n}, \tag{2.39}$$

$$\delta\dot{\tilde{T}} = \epsilon_{LP}\,\delta\dot{n} + \frac{\kappa_T}{n_0 c_{V1}}\partial_z^2 \delta\tilde{T}, \tag{2.40}$$

where $\partial_z U_0(z)$ is a slowly varying function.

Note that in the experiments, we study the evolution after the perturbing potential is extinguished, yielding $\delta U = 0$. Further, we measure in a nominally uniform region along $z$ in the middle of the box, where $U_0(z)$ is a slowly varying function. Further we use a short time scale so that the reflection of sound by the walls does not matter. Hence we have $\partial_z U_0 \simeq 0$.

With $\delta U = 0$, $\partial_z U_0 = 0$, a spatial Fourier transform of Eqs. 2.39 and 2.40 yields coupled time-dependent equations for the Fourier amplitudes $\delta n(q,t)$ and $\delta\tilde{T}(q,t)$,

$$\delta\ddot{n}(q,t) = -c_T^2\, q^2\,[\delta n(q,t) + \delta\tilde{T}(q,t)] - 4\eta\, q^2/(3n_0 m)\,\delta\dot{n}(q,t) \tag{2.41}$$

$$\delta\dot{\tilde{T}}(q,t) = \epsilon_{LP}\,\delta\dot{n}(q,t) - \kappa_T q^2/(n_0 c_{V_1})\,\delta\tilde{T}(q,t), \tag{2.42}$$

where $\epsilon_{LP} = c_{P_1}/c_{V_1} - 1$. Note that the bulk viscosity $\xi_B = 0$ for a unitary Fermi gas [Son 2007; Elliott et al. 2014].

We can express the local shear viscosity in units of $\hbar\, n_0$,

$$\eta \equiv \alpha_\eta\, \hbar\, n_0 \tag{2.43}$$

and determine $\alpha_\eta$ from the measurements. Similarly, we can express the thermal conductivity in units of $\hbar\, n_0\, k_B/m$ as

$$\kappa_T \equiv \alpha_\kappa \hbar\, n_0\, \frac{k_B}{m} \tag{2.44}$$

and determine $\alpha_\kappa$ from the measurements.

To simplify the expressions, we can define $q$-dependent properties — an oscillation frequency $\omega_T$ and two decay rates $\gamma_\eta$, $\gamma_\kappa$ to describe the evolution. Let

$$\begin{aligned} \omega_T(q) &= c_T\, q \\ \gamma(q) &= \frac{\hbar}{m}\, q^2 \\ \gamma_\eta(q) &= \frac{4}{3}\, \alpha_\eta\, \gamma(q) \\ \gamma_\kappa(q) &= \alpha_\kappa\, \frac{k_B}{c_{V_1}} \gamma(q). \end{aligned} \tag{2.45}$$

Eqs. 2.41 and 2.42 then become

$$\delta\ddot{n}(q,t) = -\omega_T^2\, [\,\delta n(q,t) + \delta\tilde{T}(q,t)\,] - \gamma_\eta(q)\, \delta\dot{n}(q,t) \tag{2.46}$$

$$\delta\dot{\tilde{T}}(q,t) = \epsilon_{LP}\, \delta\dot{n}(q,t) - \gamma_\kappa(q)\, \delta\tilde{T}(q,t). \tag{2.47}$$

The above equations have an analytic solution. The general solution for $\delta n(q,t)$ and $\delta\tilde{T}$ consists of

$$\begin{aligned} \delta n(q,t) &= A e^{-s\,t} \\ \delta\tilde{T}(q,t) &= B e^{-s\,t}. \end{aligned} \tag{2.48}$$

Then Eqs. 2.46 and 2.47 require

$$(s^2+\omega_T^2-\gamma_\eta\, s)A+\omega_T^2\, B = 0 \tag{2.49}$$

$$\epsilon_{LP}\, s\, A-(s-\gamma_\kappa)\, B = 0. \tag{2.50}$$

A nontrivial solution is obtained by setting the determinant of the coefficients equal to zero,

$$(s^2+\omega_T^2-\gamma_\eta\, s)(s-\gamma_\kappa)+\epsilon_{LP}\, s\, \omega_T^2 = 0. \tag{2.51}$$

So, we have

$$s^3-s^2(\gamma_\kappa+\gamma_\eta)+s\,(\omega_S^2+\gamma_\kappa\gamma_\eta)-\omega_T^2\gamma_\kappa = 0, \tag{2.52}$$

where $\omega_S^2=(1+\epsilon_{LP})\,\omega_T^2 = c_{P_1}/c_{V_1}\,\omega_T^2$, i.e., $\omega_T = c_T\, q$ and $\omega_S = c_S\, q$.

Eq. 2.52 is a cubic polynomial with real coefficients, which must have one real root $\Gamma$ and one complex pair $a \pm i\, b$, i.e., it factors as $(s-\Gamma)[(s-a)^2+b^2]$. Then,

$$s^3-s^2(\Gamma+2\,a)+s\,(a^2+b^2+2\,a\,\Gamma)-\Gamma(a^2+b^2) = 0. \tag{2.53}$$

Comparing the coefficients of $s^n$ in Eq. 2.53 and Eq. 2.52, we find

$$\Gamma+2\,a = \gamma_\eta+\gamma_\kappa \tag{2.54}$$

$$a^2+b^2+2\,a\,\Gamma = c_S^2\, q^2+\gamma_\eta\,\gamma_\kappa \tag{2.55}$$

$$\Gamma(\,a^2+b^2) = c_T^2\, q^2\,\gamma_\kappa. \tag{2.56}$$

As there are three solutions with three initial conditions, we take the density perturbation to be

$$\delta\, n(q,t) = A_0\, e^{-\Gamma t}+e^{-a\,t}\,[A_1\cos(b\;t)+A_2\,\sin(b\;t)], \tag{2.57}$$

The first initial conditions $\delta\, n(q,0)=A$ requires $A_1 = A-A_0$, and from $\delta\,\dot{n}(q,0)=0$, we can obtain $A_2=[(\Gamma-a)A_0+a\,A]/b$.

With $\delta\,\tilde{T}(q,0)=0$, the third initial condition follows from Eq. 2.46, $\delta\,\ddot{n}(q,0)=-\omega_T^2\,A$. By comparing $\delta\,\ddot{n}(q,0)$ with a direct calculation from Eq. 2.57, this yields the amplitude $A_0$,

$$[(\Gamma-a)^2+b^2]A_0 = (a^2+b^2-c_T^2q^2)A. \tag{2.58}$$

Similarly, the temperature perturbation is given by

$$\delta\tilde{T}(q,t) = B_0\left[e^{-\Gamma t} - e^{-at}\cos(b\,t) + \frac{\Gamma - a}{b}\,e^{-at}\sin(b\,t)\right], \tag{2.59}$$

which satisfies $\delta\tilde{T}(q,0) = 0$ and $\delta\dot{\tilde{T}}(q,0) = 0$, as required by Eq. 2.47 with the initial condition $\delta\dot{n}(q,0) = 0$. From Eq. 2.47, and using $\delta\ddot{n}(q,0) = -\omega_T^2 A$, we also have the additional constraint $\delta\dddot{\tilde{T}}(q,0) = -\epsilon_{LP}\,c_T^2 q^2 A$. Using Eq. 2.59, we find $B_0$,

$$[(\Gamma - a)^2 + b^2]B_0 = -\epsilon_{LP}\,c_T^2 q^2 A. \tag{2.60}$$

We have developed a complete analytic solution for the evolution of $\delta n(q,t)$ and $\delta\tilde{T}(q,t)$, connecting all the coefficients and physical properties. We fit Eq. 2.46 to the data using the three frequencies $c_T q, \gamma_\eta, \gamma_\kappa$, and the amplitude $A$ as free parameters. We can see that the solution consists of two independent modes. One is an exponentially decaying thermal diffusion mode, and the other is a decaying, oscillating first sound mode, see Fig. 2.3. The physics of these two modes is illustrated as follows.

Fig. 2.3 shows the modes that contribute to a typical fit for $T/T_F = 0.46$ data, which sits in the middle of our temperature range. From the fit, we can find the contributions of the first sound mode and thermal diffusion mode to $\delta n(q,t)$ and $\delta\tilde{T}(q,t)$. First, we determine the frequencies $\Gamma$, $a$, and $b$ from the fit parameters $c_T q, \gamma_\eta, \gamma_\kappa$ using Eqs. 2.54-2.56. This is most easily done by finding the real solution $\Gamma$ of Eq. 2.52. Then Eq. 2.54 determines $a$ and Eq. 2.55 yields $b$. Eq. 2.58 then determines $A_0$ in terms of the fitted amplitude $A$ and Eq. 2.60 determines $B_0$. We scale the plots by $A$ to normalize to 1 at $t = 0$.

From Fig. 2.3 we can see the contribution of the zero frequency, exponentially decaying thermal diffusion mode to $\delta n(q,0)$ is initially $\simeq 32\%$. The large amplitude enables independent determination of the thermal conductivity through the decay rate $\Gamma$. In $\delta\tilde{T}(q,t)$, we see that $\delta\tilde{T}(q,0) = 0$ forces the first sound and thermal diffusion modes to be initially 180° out of phase, ensuring an isothermal initial condition.

On the other hand, the first sound mode is described by an oscillating exponential decay. The oscillation frequency gives the first sound speed, which determines the reduced temperature from Eq. 2.19 and the equation of state (see Fig. 2.1). The decay rate gives the usual first sound diffusivity, $D_1 = 2a/q^2 \simeq D_\eta + D_\kappa$, which contains contributions only from the shear viscosity and the thermal conductivity (see Eq. 2.66 below). So the shear viscosity can be extracted by subtracting $D_\kappa$ from $D_1$.

We see that the decay rates of these two distinct modes determine both the thermal

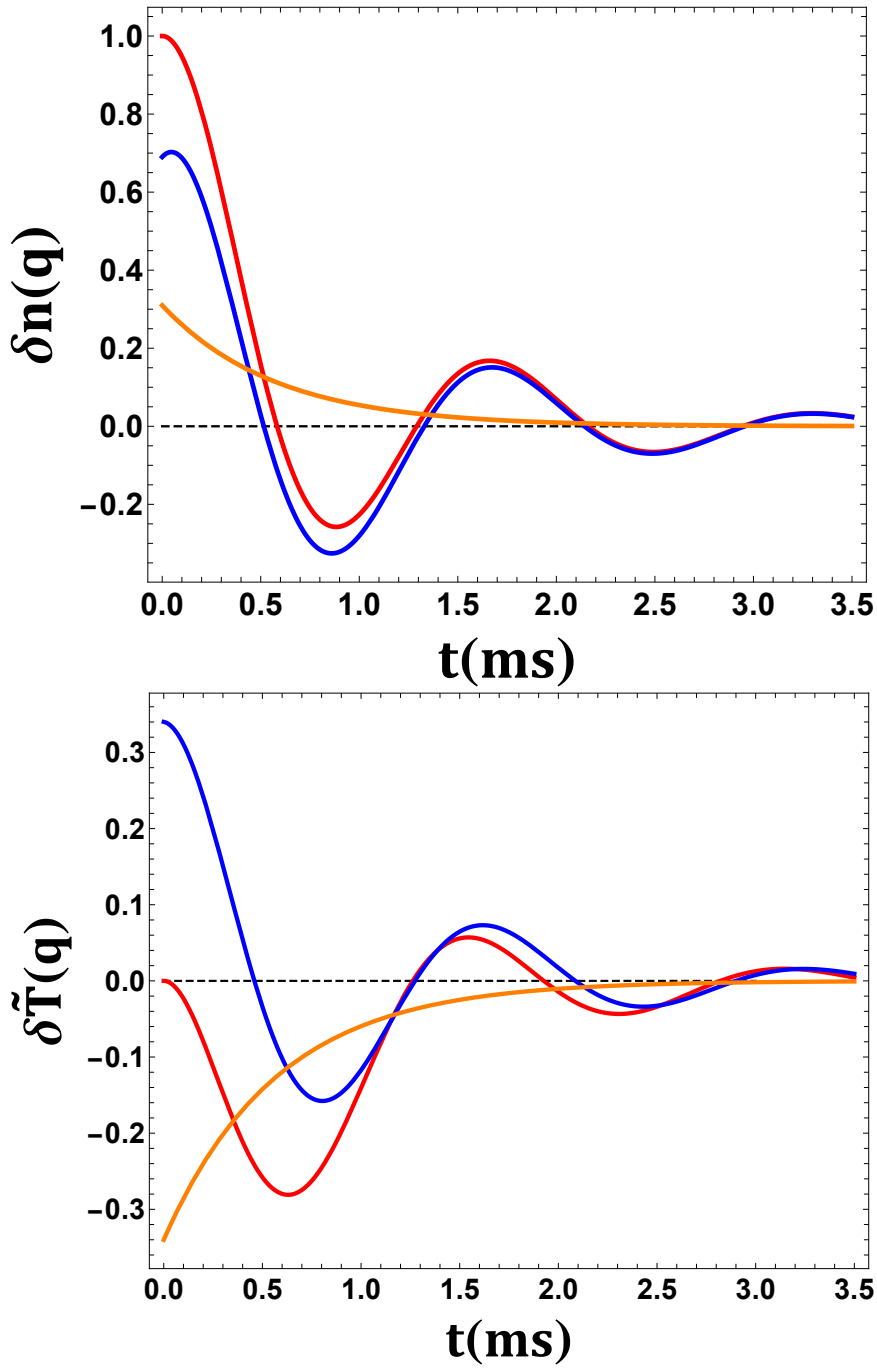


Figure 2.3: Components of the analytic fit function $\delta n(q,t)$ Eq. 2.57 and $\delta \tilde{T}(q,t)$ Eq. 2.59 for a typical data at $T/T_F = 0.46$. Red curve: Total fit function; Orange curve: Zero frequency, exponentially decaying (thermal diffusion) mode; Blue curve: oscillating, exponentially decaying first sound mode. Note that the two components are in phase for $\delta n(q,0)$ and 180° out of phase for $\delta \tilde{T}(q,0)$, ensuring an isothermal initial condition.

conductivity and the shear viscosity.

### 2.2.3 Damped Oscillator

In the previous subsection, we introduce the usual first sound diffusivity $D_1$, which is given by $2a/q^2$ from the first sound mode.

We expect that the first sound mode behaves essentially as a damped oscillator of resonance frequency $\omega_S = c_S q$ and damping rate $2a$, for which the equation of motion is

$$\ddot{x} + 2a\dot{x} + \omega_S^2 x = 0 \tag{2.61}$$

The general solution $x = A\,e^{-s\,t}$ satisfies

$$s = a \pm i\sqrt{\omega_S^2 - a^2} \equiv a \pm i\,b. \tag{2.62}$$

In this case, the damped oscillation frequency is $b \simeq \sqrt{\omega_S^2 - a^2}$, so that $\omega_S$ should be closer to $\sqrt{a^2+b^2}$. Actually from our measurements, for $T/T_F = 0.28$, 0.46 and 0.63, we find that $\omega_S/\sqrt{a^2+b^2}$ is 1.006, 1.015, and 1.008, nearly unity as expected.

We can understand this result using Eqs. 2.54 and 2.55, and rewrite them in the following way

$$a^2 + b^2 = \omega_S^2 + \gamma_\eta\gamma_\kappa - 2\,a\,\Gamma = \omega_S^2 + \gamma_\eta\gamma_\kappa - \Gamma(\gamma_\eta + \gamma_\kappa - \Gamma) = \omega_S^2 + (\Gamma - \gamma_\kappa)(\Gamma - \gamma_\eta), \tag{2.63}$$

where $a^2 + b^2 \simeq \omega_S^2$. In the high temperature classical limit, where the decay rates are largest, the last term is evaluated as follows,

$$\Gamma - \gamma_\kappa = \gamma_\kappa(\frac{\omega_T^2}{\omega_S^2} - 1) = \gamma_\kappa(\frac{c_{V_1}}{c_{P_1}} - 1).$$

Taking the high temperature limit of $c_{V_1} \simeq (3/2)\,k_B$, $c_{P_1} \simeq (5/2)\,k_B$ and $\kappa_T \simeq (15/4)(k_B/m)\eta$ [Braby et al. 2010], we can write $\Gamma$ in terms of $\gamma_\eta$ and obtain $\Gamma - \gamma_\eta = (1/8)\gamma_\eta$. Together, we then have,

$$(\Gamma - \gamma_\kappa)(\Gamma - \gamma_\eta) \simeq -\gamma_\eta\gamma_\kappa/20 \ll \omega_S^2. \tag{2.64}$$

A similar conclusion that $(\Gamma - \gamma_\kappa)(\Gamma - \gamma_\eta) \ll \omega_S^2$ for lower temperatures can be easily made since the decay rates are even smaller.

Hence, we can take $a^2 + b^2 = \omega_S^2 = c_S^2 q^2$ in Eq. 2.56. With $c_T^2/c_S^2 = c_{V_1}/c_{P_1}$ and $\gamma_\kappa/q^2 =$

$\kappa_T/(n_0 c_{V_1})$, we obtain,

$$\frac{\Gamma}{q^2} = \frac{\omega_T^2}{\omega_S^2}\frac{\gamma_\kappa}{q^2} = \frac{\kappa_T}{n_0\, c_{P_1}} = D_T, \tag{2.65}$$

with $D_T$ the thermal diffusivity. With Eq. 2.65 and $\gamma_\eta/q^2 = 4\eta/(3n_0 m)$, Eq. 2.54 shows that the measured $2\,a/q^2$ is, to a very good approximation, the usual first sound diffusivity [Landau and Lifshitz 1959],

$$D_1 = \frac{2\,a}{q^2} = \frac{4}{3}\frac{\eta}{n_0 m} + \left(\frac{1}{c_{V_1}} - \frac{1}{c_{P_1}}\right)\frac{\kappa_T}{n_0} = D_\eta + D_\kappa\,. \tag{2.66}$$

Eq. 2.65 shows that the decay rate $\Gamma$ of the thermal diffusive mode determines the thermal conductivity $\kappa_T$. Measurement of the decay rate $2a$ of the first sound mode determines $D_1$ in Eq. 2.66, and yields $\eta$.

CHAPTER

# 3

# EXPERIMENTAL METHODS

In this chapter, I will discuss the preparation of an ultracold degenerate gas of $^6$Li atoms, and the optical system for applying the perturbing potentials. The atoms are trapped and cooled to a temperature near absolute zero ($T \sim$ 10-100 nK) before being transferred into a box shaped potential. The basic technique and the experimental apparatus used in our lab to trap and cool the atoms are well described in detail in the theses of our previous group members, and this will only be briefly described here. Readers are encouraged to refer to O'Hara [2000]; Gehm [2003]; Kinast [2006]; Joseph [2010]; Jagannathan [2016]. The main part of this chapter will be focused on the new techniques to create a stable and relatively strong box potential by utilizing a digital micro-mirror array (DMD) and a diffracting "top-hat" (TH) beam shaper.

## 3.1 Atom Trapping and Cooling

There are several stages for preparing an ultracold atoms samples for our studies. $^6$Li atoms are solid at room temperature in our source. First, we need to heat a sample of lithium to create an atom gas flux. Then the atoms need to be captured and evaporatively cooled to

low temperature. Last, we need to put them into the box potential, which is our final trap, without additional heating.

The experimental apparatus contains a locking region and a main system. Each of these is comprised of a vacuum system with an oven as atom source. Both ovens are heated to approximately 400°C to supply the atoms for our experiments.

The locking region is a system to generate laser beams with required frequencies in the experiments. In this system, the frequency of a Coherent 899 dye laser, pumped by a Coherent Verdi V10 diode pumped solid state laser, is refered to an atomic resonance of $^6$Li near 671 nm, providing a stable "main beam" with a power of about 800 mW. This main beam is then directed through different beam paths to the main system. Within each path the frequency is modulated by one or more acousto-optic modulator (AOMs), which acting as a grating to modulate the angle and frequency of the non-zeroth order passing-through beams. We use the first order beams deflected outward from the AOM, and the frequency is controlled by an applied driving voltage. With such a setup, we are able to tune the individual laser beams to different desired frequencies, for atom trapping, cooling, and imaging.

The main system makes use of two different physical mechanisms to trap and cool atoms. The first mechanism is absorption and emission of photons and the second mechanism is electric dipole interactions. The first mechanism applies to the setup of a Zeemann slower, a magneto-optical trap (MOT) and another MOT optical beam called the "repumper", which will be discussed shortly. Fig. 3.1 shows the system set up for these trapping and cooling stages.

The atoms initially travel at high velocity and they are quickly slowed and captured by a slower beam. Photons in this red-detuned near-resonant counter-propagating beam is absorbed by the atoms traveling towards the beam, with the Doppler effect shifting their frequency to resonance. The atoms then emit photons in random direction, thus the atoms slow down as a result of momentum conservation. Moreover, a magnetic field generated by the Zeeman coils produce a spatially varying Zeeman shift to the energy levels of the atoms to keep cooling them, compensating for the reduced Doppler effect when atoms slow down. Together, this setup is called the Zeeman slower.

Then a magneto-optical trap or MOT traps the atoms near the center region of the vacuum chamber and provides additional cooling. The MOT is a combination of 3 pairs of retro-reflected beams and magnetic fields. It provides Zeeman shifts and Doppler shifts, by the same mehanism as the Zeeman slower, but in all six directions. Also, the MOT beams are polarized in a way to provide restoring forces when atoms move away from the center.

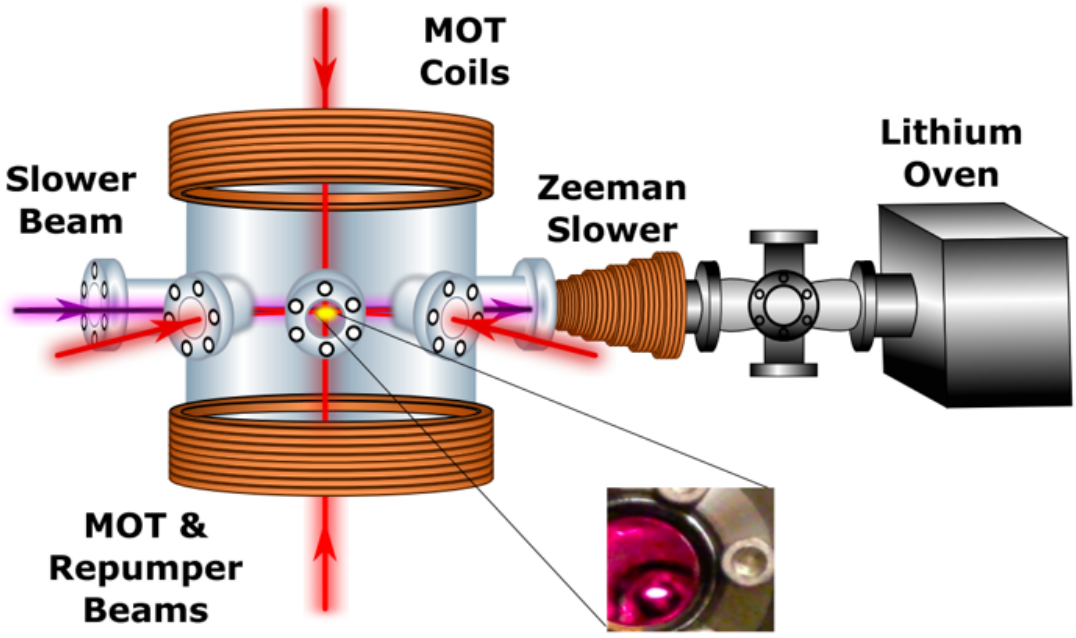


Figure 3.1: Experimental setup for initial cooling of $^6$Li atoms by the Zeeman slower and the slower beam and precooling by the MOT beams, repumper beams and MOT coils. MOT and repumper beams are overlapped and are shown together in red. Inset shows fluorescence from the atoms trapped in the MOT. *This figure is directly taken form thesis of Jagannathan [2016] for demonstration purpose.*

In our lab, about 300 million atoms are cooled to the Doppler limited temperature of 140 $\mu$K in the MOT[1].

The first mechanism cannot further cool the atoms below the Doppler limited temperature of about 140 $\mu$K [Kinast 2006]. To further cool the atoms, we load a far off resonance trap or FORT generated by a ultra-stable Coherent DEOS LC100-NV $CO_2$ laser (140 W) beam and perform evaporative cooling. The cigar like shape FORT provides an electric dipole potential that confines the atoms in space. The dipole potential is written as

$$U_{dip} = -\frac{2\pi}{c}\alpha I, \tag{3.1}$$

where $I$ is the intensity of the laser beam. The $CO_2$ laser beam has a cylindrically symmetric

[1]In order to cool the atoms in both $F = 1/2, 3/2$ states, an additional beam called "repumper beam", tuning 228 MHz lower than the MOT beam, co-propagates with the MOT beam

gaussian profile, so the intensity can be written as,

$$I(r,z,\phi) \quad = \quad \frac{I_0}{1+(z/z_0)^2}\exp\left\{-\frac{2r^2}{w^2}\right\}, \tag{3.2}$$

where $I_0$ is the peak intensity, $z_0$ is the Raleigh length and $\omega$ is the $1/e^2$ radius of the beam.

Here, the polarizability for the ground state of $^6$Li is

$$\alpha = \alpha_0 \frac{\omega_0^2}{\omega_0^2-\omega^2}, \tag{3.3}$$

where $\alpha_0$ is the static polarizability for frequencies far below resonance, taking the form of $2\mu_{eg}^2/\hbar\,\omega_0$.

The wavelength of the $CO_2$ beam is 10.6 $\mu$m, which is much larger than resonant wavelength of the atom $\sim$ 671 nm. So from Eq. 3.1 - 3.1 we can easily find that the FORT potential is attractive, deeper in the center.

In the FORT, we use a bias the magnetic field to tune to the strongly interacting regime, and the atoms collide with each other, sharing energy and rethermalizing. The hot atom escape the trap and the colder atom effectively cool down after rethermalization. A passive evaporative cooling with full $CO_2$ trap depth is called the free evaporation, during which the atoms can be cooled to $\sim 50\,\mu$K. After this stage, a forced evaporation by lowering the trap depth provides the final cooling. We use a lowering curve,

$$U(t) = U_0\left(1+\frac{t}{\tau}\right)^{-1.44}, \tag{3.4}$$

which ensures efficient evaporative cooling while, at same time, keeping the most atoms in the trap [O'Hara et al. 2001], where $t$ and the lowering constant $\tau$ can be adjusted for different final trap depth.

The lowering of the FORT is realized by controlling the applied RF voltage on the $CO_2$ AOM, which acts as a beam intensity modulator here. We applied two RF signals (40 MHz and 32 MHz) on the AOM to maintain the total RF power during the lowering to ensure temperature stability in the AO, avoiding beam angle changes. The output beam modulated by the 40 MHz RF signal is what we use for the FORT. At the end of the forced evaporation stage, the temperature of the atoms can be as low as 10 nK.

Finally, the atoms are slowly transferred into a box potential, which comprises six sheets of replusive blue-detuned light, created by two digital micromirror devices (DMDs). The

top and bottom sheets employ a 669 nm beam from a diode laser. The four vertically propagating sheets are produced by a 532 nm diode laser beam, which passes through a diffractive optical element and an imaging lens to produce a “top-hat” shaped intensity profile on the surface of the DMD array.

With the flexibility of the DMD (we will discuss in Sec.3.3.2), we are able to transfer the atoms from the FORT smoothly to the box without moving in space, which avoids losing or heating the atoms. The repulsive dipole force confines the atoms inside the box with nominally uniform or slowly varying density profiles in all three directions. The “walls” built by the repulsive force are designed to be strong enough to hold the atoms of various temperatures, without noticeable atom loss during the experimental time scale. This provides an ideal platform to measure thermodynamic and transport properties.

## 3.2 Imaging

After the atoms are cooled and trapped in the final box potential, the vertical 532 nm beam crafted by the DMD is used to generate a spatial periodical perturbing potential for experiments (see Sec.3.4.2). After re-reaching thermal equilibrium, the perturbing potential is turned off and the atoms then undergo free evolution inside the box.

To observe the atom evolution, we use absorption imaging to extract the density profile of the atom cloud. This technique uses a pulse of resonant light to image the atom cloud, the transmitted intensity profile is then recorded on a CCD camera. The density profiles can be obtained by reconstructions of the images.

Fig. 3.2 shows the beam setup for the box and the referencing frame (x-y-z). We have two cameras to look at the atom cloud: one views the horizontal (y) direction and the other views the vertical (x) direction.

The imaging beams for these cameras are differ in frequency by about 76 MHz away, so each of them can image one spin species of the mixture in-situ. Note that we use a 50-50 mixture of spin-up ($|1\rangle$) and spin-down ($|2\rangle$) atoms. Their energy difference at high field of 832 G is calculated to be about 76 MHz. By tuning the frequencies of two imaging beams 76 MHz apart, we are able to use two cameras, with each of them viewing one spin species of the mixture. Since the imaging beam only resonantly absorbed by one spin state without interrupting the other spin state, this yields in-situ imagery of both spins.

The images we take are processed by a converting code, which relates the extracted column density to the photon counts in each pixel and some camera characteristics to

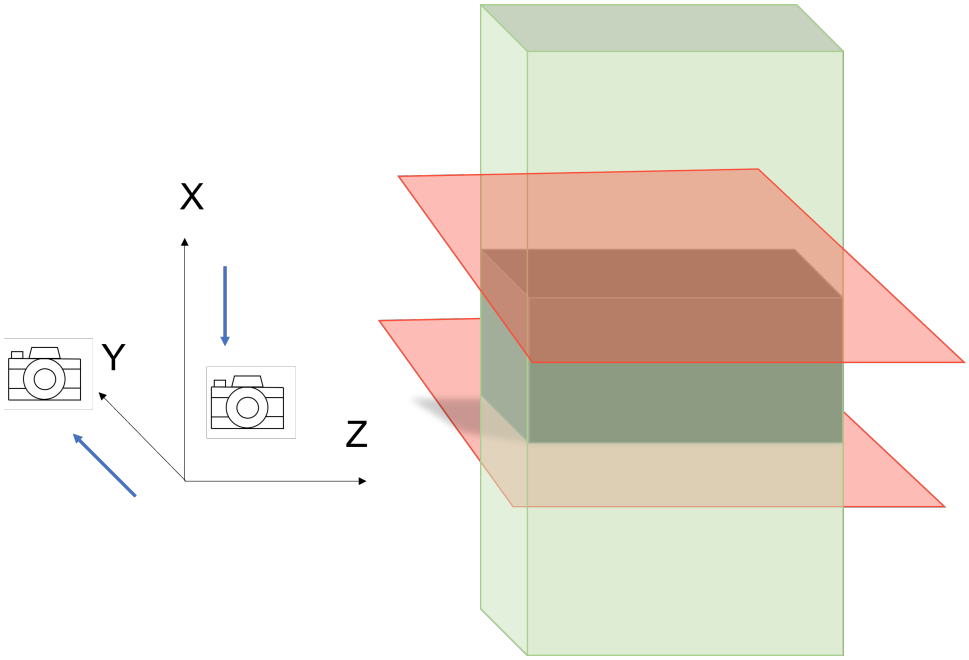


Figure 3.2: Illustration of the box trap. A 532 nm beam propagating in the vertical (x) direction provides 4 vertical walls of the box. A 669nm beam propagating in the horizontal plane (y-z) provides the top and bottom sheets. Two CCD cameras view through x and y directions at each of the two spins, enabling in-situ imagery for both spins.

give us 2D density profiles of the atoms as function of position. Then we use a "spline" method 1-D interpolation to smoothly covert the density profiles to be in units of microns (atoms/$\mu$m).

## 3.3 Optical Box

Many previous studies of quantum gases are limited by the trapping beam shapes, which is usually a gaussian profile in space. One downside of the gaussian shaped trap is that the density of the trapped atoms varies near the cloud edges, which makes theories hard to test. To investigate the properties of the gases more properly, beam-shaping techniques are essential for creating controlled profiles for different applications.

As I mentioned in the introduction, a uniform sample of unitary Fermi gases in a box is the ideal platform for studying hydrodynamic transport properties. A good way to realize uniform density distribution is to transfer the cold atoms from FORT to another trap, which has the geometry of a rectangular box. By carefully aligning the position of the box in the

center of the magnetic bowl, formed by gradient of the bias magnetic field (see Sec. 3.3.4), once the FORT is turned off, the only trapping potential arises from the 6 walls of the box. The atoms can then flow almost freely to uniformly occupy the space inside the box.

It was not easy to build a box potential with sharp edges and strong confinement in the past. However, by combining some new technology, a good box potential is accomplished in our lab. The basic apparatus includes 2 blue-detuned laser beams, 2 Digital Micromirror Devices (DMDs), a "top-hat" beam shaper with adjustable telescopes and two wavelength selecting optics. A schematic of the optical setup is shown in Fig. 3.3.

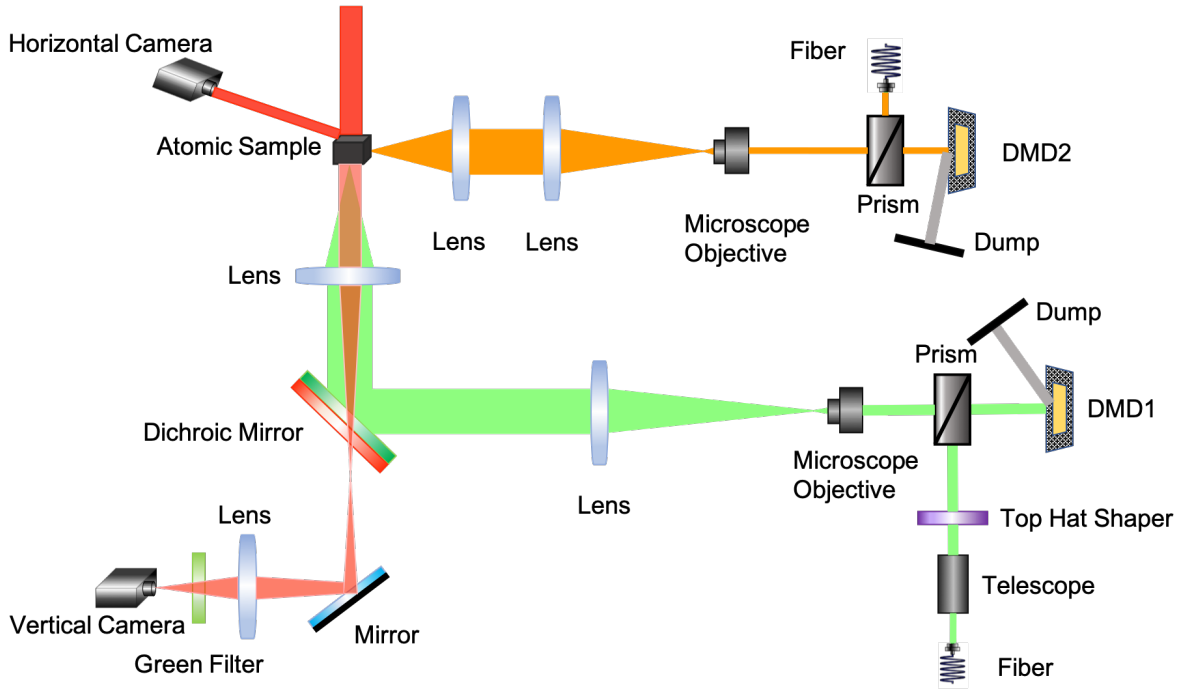


Figure 3.3: Box beam path along with the main chamber and imaging system. Top(bottom) orange(green) colored shapes represent a 669 nm gaussian (532 nm "top-hat") laser beam. Red colored shapes represent the imaging beams.

While the details of these new techniques will be described later, it is useful to know some basic concepts to understand the system setup. The DMD is a dynamic spatial light modulator that can reshape the incoming light. It puts an arbitrary pattern on the incoming beam and projects the pattern onto the atoms, with a de-magnification by a microscope objective. Also, a diffractive optic, called "top-hat" beam shaper, is used to make the incoming beam intensity flat on the DMD, increasing the box potential (the reasons are explained

in following subsections).

### 3.3.1 Box Beam

To build a box for the atoms, the first question one naturally asks is what's the material for the "walls". We learn from the previous section that electrical dipole forces can be used to trap the atoms without resonant interactions. Similarly, we can use pure optical beams for box trapping. However, we need a repulsive beam here.

After the forced evaporation, the atoms reach the desired temperature in the FORT. We can then release the atoms to the box potential, constructed by 6 repulsive laser beam sheets, taking advantage of dipole forces. As we discussed in Sec. 3.1, the dipole potential takes the form of

$$U_{dip} = -\frac{2\pi}{c}\,\alpha_0 \frac{\omega_0^2}{\omega_0^2-\omega^2}\,I. \tag{3.5}$$

It is obvious that we need a beam frequency $\omega$ higher than the resonant frequency $\omega_0$, in other words, a blue-detuned light, to give us a repulsive potential.

We want to build a strong box trap with the capability of holding atoms with a variety energies. The depth of the optical potential should be at least few times of the typical Fermi energy in experiments, which is $\sim 0.2\mu$K. Since the optical potential scales roughly as inverse of $\omega_0^2-\omega^2$, tuning closer to the resonance frequency would provide a deeper box. Meanwhile, we also need to be careful not to use a beam too close to the atomic line. Even for a box trap setup, where most of the beam does not directly shine on the atoms, if the wavelength is close enough to the resonance, light scattering will heat the gas and cause loss.

Taking these ideas into consideration, a diode laser centered around 669 nm is a very good choice for our box beams. This wavelength is about 2 nm away from atomic resonance, which gives strong dipole force without too much light scattering. For a typical Toptica diode laser tuned at 669 nm, the output power is around 200 mW. With power losses through the necessary optical elements, this power is still sufficient to provide a trap of a few $\mu$K when it's focused on the atoms. This energy is much bigger than the nominal Fermi energy $\simeq 0.2\mu K$, so the optical trap depth is very good.

To create a 3D box, we need two perpendicularly propagating beams to form 6 sheets for the walls. A straight forward choice is to use the 669 nm beams for both propagating directions. However, we also need to think about the separation of imaging beams, which are at 671 nm.

We have two CCD cameras taking images for the horizontal and the vertical views. For our vacuum chamber, there is only one pair of window ports for beams in the vertical direction. Notice that the MOT configuration needs three perpendicularly propagating beams, so one of the MOT beams has to co-propagate with the vertical image beam. This is not a problem since we always take pictures after the MOT procedure is done. So a simple electronically controlled flipper mirror can separate those two vertical beams and turn each on in a sequence. However, for the box beam, we cannot use the same method.

For the best measurements, we always want to take in-situ images so that we minimize any disturbance to the properties we study. This means the imaging beams need to be turned on when the box beams are present. To solve the problem, we can use dichroic beam splitters. Dichroic mirrors or beam splitters can spectrally separate light by transmitting and reflecting light as a function of wavelength. Lowpass dichroic mirrors have a transmission and reflection band that are divided by a cut-on wavelength. This type of dichroic is highly reflective below the cut-on wavelength and highly transmissive above it. It allows us to separate the box beam from the imaging beam right outside of the vacuum chamber. Now, we look back at our candidate beam of 669 nm. It's only 2 nm away from the imaging beam which is tuned to resonance. This makes it extremely hard to find a dichroic mirror that can separate them.

Also, let's think more about the general ideas of the experiment. We want to build a versatile platform that can conduct different kinds of experiments in a uniform box potential. Besides building a box, we also want to apply some perturbing potentials on the atoms, either static or moving. To make the apparatus not too complicated, we prefer to use the same laser beam for the box and perturbing potentials. If the optical force is too strong, we will lose dynamic range for designing an spatially varying perturbations. This will be discussed in detail in Sec. 3.3.2.

Another disadvantage of a near resonance beam is that we cannot shine the beam on atoms for long time without exciting the atoms. Indeed, for the purpose of holding the perturbing potential long enough for reaching a thermal equilibrium, we would rather use a far off resonance light.

Based on the two concerns above, it is better to choose a wavelength further away from resonance for the vertical box beam. But with limitation of the damage threshold of the DMD, we cannot go too far away from the resonance where a very high power is required for a strong trap. We use a Coherent Verdi V10 diode-pumped laser to generate a high power stable green beam at 532 nm. This wavelength is well below the atomic resonance, which allows us to effectively separate it from the imaging beam using a dichroic beam splitter.

Although the dipole polarizability is smaller compared to that of the 669 nm beam, the output power of Verdi can go up to 10 W, which is much higher than the power of the 669 nm beam. This compensates for the overall strength of the force, making a strong enough force for the box walls and not too strong for the perturbing potentials.

Another fact we need to take into consideration is the effect of bias magnetic field curvature, which inevitably exerts forces on the atoms inside the box. Without going deeply to this topic, a brief conclusion is that the force is repulsive in the vertical direction and attractive in the horizontal plane. Both are small but not negligible compare to optical potential. So we would prefer the horizontal box beams to be stronger to give additional vertical confinement against the magnetic force, for the top and the bottom sheets.

Fig. 3.4 shows the beam setup for the box. We chose to build our box with two different beams. A horizontal red 669 nm beam provides stronger top and bottom walls; a vertical green 532 nm beam provides the other four walls, as well as creating perturbing potentials. The red beam propagates in a path that does not overlap with imaging beams. The green beam shares part of the vertical path with the imaging beam, and they are separated by a longpass dichroic mirror. Additionally, since the selective efficiency of a dichroic mirror is not 100 %, a lowpass filter is placed in front of the camera to minimize green light transmission.

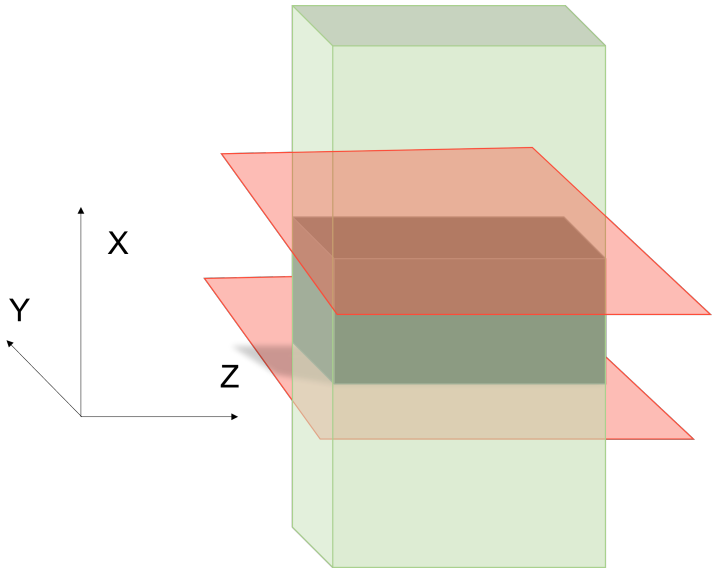


Figure 3.4: Illustration of the box trap. A 532 nm beam propagating in the vertical (x) direction provides 4 vertical walls of the box. A 669nm beam propagating in the horizontal plane (y-z) provides the top and bottom sheets.

### 3.3.2 Digital Micromirror Devices

With the laser sources of the box beams chosen, let us move forward to discuss the beam shaping. Some beam shapes can be generated from passive approaches, such as a diffractive phase plate, refractive aspheric lens or axicon pairs, or a binary-transmissive metal mask. However, these methods cannot adjust for variations in input beam profiles due to imperfect optical systems or produce different types of output beam profiles on demand. Spatial light modulators (SLMs), on the other hand, provide a programmable modulation of phase and/or amplitude. It opens possibilities for arbitrary beam shape designs. Furthermore, if a programmable SLM is able to update patterns fast enough, the beam shapes can be controlled in both space and time, which allows us to dynamically control the optical potentials [Gauthier et al. 2021].

The digital micromirror array (DMD) emerges as a versatile tool for arbitrary beam shaping and dynamical control. The TI-DLP chipset has been used in image display, industrial and medical applications, for high resolution and high speed spatial light modulation. However, recently it has been applied to laser beam shaping and atom trapping in research. The DLP chipsets utilize highly reflective aluminum micromirrors, known as a digital micromirror device (DMD).

Each DMD contains up to 8 million individually controlled micromirrors built on top of an associated CMOS memory cell. During operation, the DMD controller loads each underlying memory cell with a “1” or a “0”. Next, a mirror set pulse is applied, which causes each micromirror to be electrostatically deflected about a hinge to the associated +/- 12 degree state, defining as “on” and “off”. The deflection angle of these two valid states is very repeatable due to a physical stop against two spring tips [DMD]..

There are two types of patterns that can be realized by the DMD: binary and grayscale. Binary patterns are created by direct display of black and white pictures. Grayscale patterns are created by programming the on/off duty cycle as functions of time for each mirror, which allows additional flexibility for pattern design.

In our system, the ‘on’ state beam is reflected to the main vacuum chamber and the ‘off’ state beam goes to a beam damp (black paper board). This acts as an intensity mask on the original beam, which is a “top-hat” beam in our case (Sec. 3.3.3, to reshape the light. The designed patterns are programmable, and they are stored in the CMOS memory cell in the form of image files. The displayed pattern on the mirrors constructed by ‘on’ and ‘off’ pixels can be held or changed by receiving internal or external triggers. This allows dynamical control of the light in a very precise way.

In our application, we chose a DLP 6500 to shape the horizontal beam for its fine pixel size and DLP 7000 to shape the vertical beam for its fastest pattern rate. Reasons for this selection will be discussed in detail later.

In our applications, we have some specific requirements for the beams. The DMD chipset models and the way to program them need to be carefully considered. First of all, the device needs to handle relatively high beam intensity for forming a deep box trap. However, since the primary applications of DMD were for displays, they were not originally designed for high power handling. In order to do laser beam shaping safely, we need to carefully check the thermal responses of the DMD. According to the general DMD data sheets, the average power density (peak power density • duty cycle) cannot exceed the specification of 25 W/cm$^2$ for all DMDs. So we don't have the flexibility to choose a higher power DMD.

However, we use some methods to increase power without damaging the device. First, when we don't need the box beam, instead of turning the DMD to the "off" states while keeping the laser beam on, we chose to turn off the AOM for the 532 nm beam and direct the input beam to a beam dump. This way we keep the active duty cycle short to give the device enough time to cool down. Second, we expand our laser beam and chose a relatively large area on the DMD to illuminate for lower intensity on it, and then de-magnify the beam to hit the atoms. This also gives the advantage of using more pixels on the DMD for higher pattern resolution. Third, we make the intensity profile of the 532 nm beam almost uniform on the DMD surface, by using the "top-hat" technique, to avoid possible local damage near the high intensity gaussian peak. Note that we do not apply such technique to the 669 nm beam, since its power is much lower than the 532 nm beam.

Now, let us look at two key features of the DMD, the pixel size and the highest pattern rate. The DMD mirrors has two states: on and off, so the pattern on the DMD is binary. A smaller pixel (mirror) size grants us more pixels to use for grayscale pattern designs, which improves their resolution and fidelity. Indeed, all of the DMD chipsets have very small mirror sizes, from 5.4 $\mu$m to 13.6 $\mu$m. That is where the name "micromirror" comes from. A nominal input beam size is roughly about 1 mm, so either DMD gives good number of useful pixels for creating patterns.

Now we look at the highest pattern rates. From the company's product descriptions, for an 8-bit pattern, the DLP portfolio offers max pattern rates from 60 Hz to 4069 Hz. For our application (binary), the rate is 8 times larger. Considering the system we study, typical hydrodynamic characteristic frequencies are several thousand rad/s. In order to study hydrodynamic properties thoroughly, we prefer to have the capability to drive or

perturb the system at frequencies from well below to well above those frequencies. So with a reasonable size of the micromirrors, we want to choose the fastest chipset we can find for the direction (vertical) we apply modulations. And for the horizontal direction, we are more flexible to choose any handy model.

Based on the considerations above, we build our vertical direction beam shaping system by a DLP 7000 DMD, with key features of 13.68 $\mu$m micromirror pitch and a 32552 Hz pattern rate. It crafts the 532 nm beam for building the four vertical walls of the box, as well as for applying spatial perturbations on the atoms. For the horizontal 669 nm beam shaping, we use a DLP 6500 DMD, with key features of 7.56 $\mu$m micromirror pitch and a 11574 Hz pattern rate. The biggest reason for chosing this DMD is very simple: much cheaper!

Now with right DMD chosen, we need to think about the alignment. It is not easy to set up a DMD since its mirror orientations are tilted (mirrors flip by $\pm 12^\circ$ along diagonal direction of the array). Usually the incoming beam and reflected beam are nearly overlapping. A neat optic called a total internal reflection (TIR) prism is helpful for an easier setup, since it allows us to introduce the incoming beam at a surface almost perpendicular to the reflected beam. A high power fiber collects the beam from the laser side of the optical table and sends the beam to the TIR prism. Since the DMD is basically nothing other than a 2D array of mirrors, it acts as a diffraction grating, where there is more than one order of beam diffracted. It is important to adjust the blaze angle to get the most power out of the zero order diffracted beam. From the specifications, the maximum diffraction efficiency can reach 86 %. We optimized the angle by placing a power meter right after the DMD and maximizing the power. The application of the TIR prism also makes this process easier. It is worth mentioning that we use an IRIS-like aperture to block any other orders of the diffracted beams. The reflected beam from the DMD goes to a microscope objective for de-magnification. A roughly 1-to-1 lens system then projects the de-magnified image onto the atoms. The lens closest to the vacuum chamber is sitting on a 3-axis translation stage to provide fine adjustment for positioning.

With all the hardware setup for the DMDs described, now is a good time to explain how they are programmed in our experiments. Generally, we use our vertical (532 nm beam) DMD for building the four sides of the box and for dynamic perturbing potentials. The horizontal (669 nm beam) DMD is only used to create top and bottom sheets of the box. The DMD displays images pre-uploaded to its CMOS memory cell; one at a time based on triggers. The triggers can be either internal or external. While internal trigger mode is slightly more accurate, external trigger mode is more programming friendly, since it can be easily integrated to our MATLAB timing controls. So, we use external triggers for the

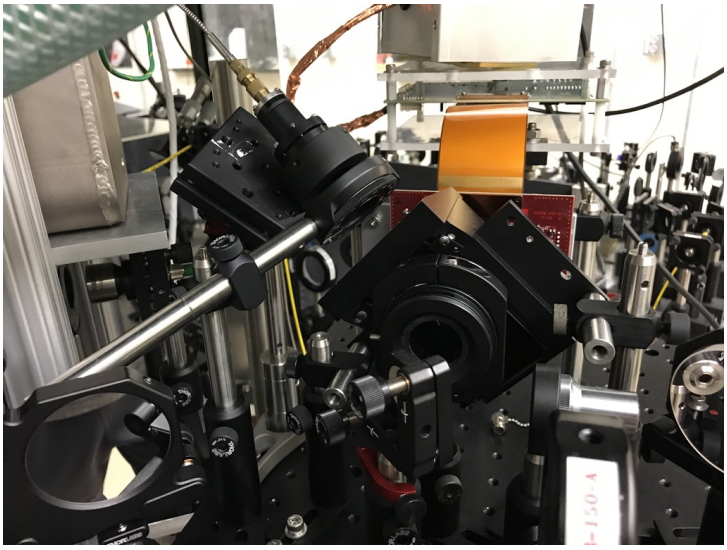

(a) DMD setup

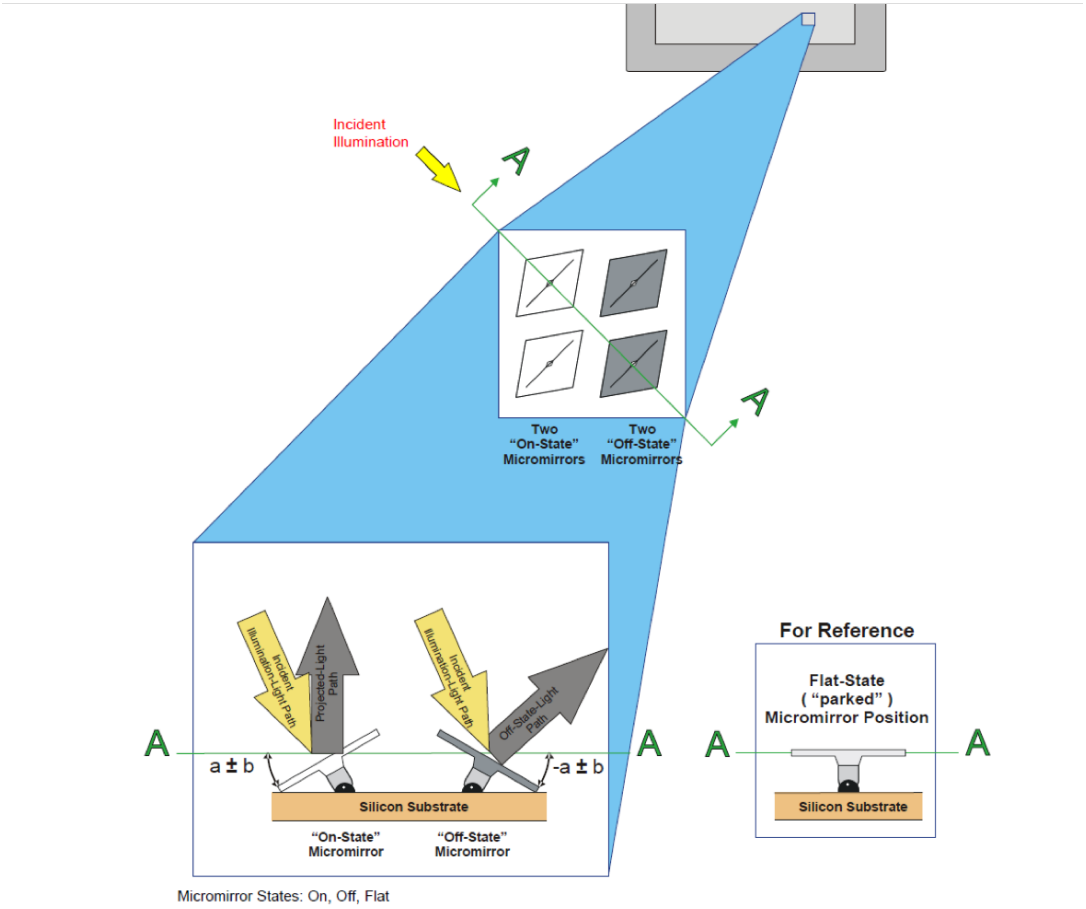


(b) DMD mirror array

Figure 3.5: (a) Setup of the horizontal DMD, key elements including a high power fiber, the DMD, a higher order diffraction beam block, a microscope objective and lenses. (b) Micromirror landed position and light paths [DMD], the orientation of the mirrors are diagonal respect to the DMD chip frame.

vertical DMD.

In our experiments, we use a sequence of different patterns to display on the DMD. These patterns are binary images of which pixel number is the same as the DMD's mirror number. We use MATLAB code to generate patterns for different boxes and perturbing potentials. There are several display modes for the DMDs, and the patterns switch differently for different modes. For the experiment, it is important to make sure we are applying a stable trapping and perturbing potential on the atoms without extra heating. So ideally, we don't want the mirrors to tilt off and back on when we switch the patterns. We carefully chose a setting called "slave mode". In this mode, when we trigger a next pattern, the mirrors remaining in the same state ("ON" or "OFF") do not move. Only those that need to change state tilt correspondingly. This guarantees constant box walls through the whole experiment, avoiding unwanted heating or atom losing. Our shortest time interval for switching between different patterns is 1 ms, which is slow compare to this DMD's maximum rate. However, we would like to know how fast the mirrors can respond to a trigger to complete a stage change. In the experiment, we want to measure the free decay of the gas, so it's important to know when the decay begins. The response time of mirrors is important since it tells us how well we know the beginning of the evolution.

We measured the response time by using a photodiode to detect the change of light signal before and after the triggers. The result shows that in the "slave mode", the response times, both from "on" to "off" and "off" to "on" are less than 10 $\mu$s The mirrors do not change orientation without a trigger.

For comparison, another measurement with the photodiode shows internal refreshes of the mirrors, when the DMD is in a "no dark time" mode. The internal refresh is caused by a setting of "picture time". It occurs even if a external trigger is not present, see Fig. 3.6. This comparison shows the importance of programming the DMD in the correct way.

Our typical data taking time interval is 100 $\mu$s and our typical evolution to watch time is 3000 $\mu$s. Since the response time is 10 $\mu$s, we can assume an instant release when we trigger the perturbation off in the "slave mode".

Now we have a clear picture of how the DMD works. The only thing left to do is to draw the patterns. The horizontal DMD is used to create the top and bottom sheets for the box. So, we simply draw two parallel bars with a spacing equals to the desired box width. The vertical DMD is used for building the other 4 sheets which I call the box frame, as well as the perturbing potential inside the frame. The rectangular frame is rotated by a small angle on the DMD to match the orientation of the FORT. Before we talk about some more details of the patterns, we need to take a look at some other technical details. Some special

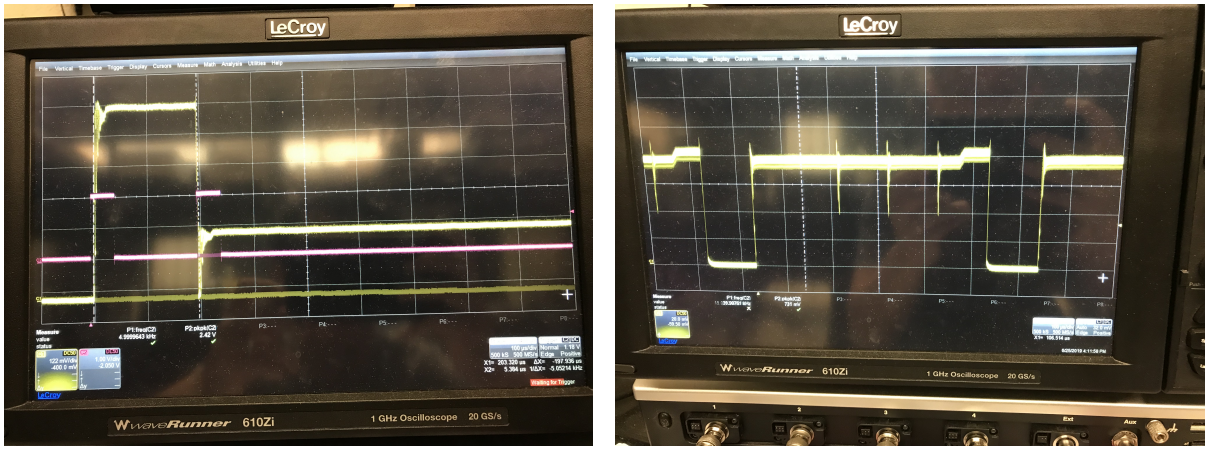


(a) Slave Mode (b) No Dark Time Mode

Figure 3.6: Left: In the proper trigger "slave mode", mirrors only respond to external triggers. Right: Example of another mode, where the mirrors refresh at a fixed time interval.

considerations for the patterns will be described in Sec. 3.4.

### 3.3.3 The "Top-Hat" Beam Shaper

With the correct laser wavelength and DMD choices, we have the foundation to build our box. However, due to some limitations of the apparatus, we need to take additional measures to make the box better.

The biggest problem for building a box of light is the spatial profile of the input beam intensity. For a single mode laser beam, the intensity distributed as a gaussian in space. On any surface the light shines, the intensity peaks in the center and decreases to the edge. With the use of DMDs, we can effectively put a transmissive mask on the beam to create a 2D box frame. In this case, we do not change the intensity distribution of the input beam. This fact can cause two problems. First, we are not utilizing all of the power of our light source, which in practice is only limited by the damage threshold of the high power fiber. Remember that we need a strong box potential to hold the Fermi gas at different temperatures. For a gaussian beam, the intensity region used by the DMD for projecting the box frame is only a small portion of the region near the peak. With a fixed input beam width, the bigger the box is, the lower the intensity. Fig. 3.7 show a gaussian beam on a long box frame, we can see the intensity decreases rapidly for the long sides.

For the longest box we use in the experiment, the intensity of the box walls is only about 25 % of the peak. Notice that damage threshold of the DMD is still set by the peak intensity,

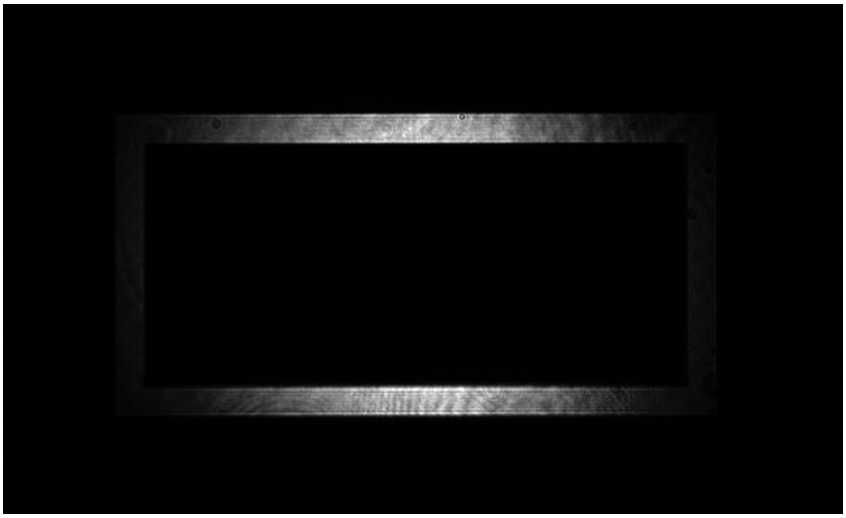

Figure 3.7: Grayscale image of a box made by the DMD with a gaussian input beam, taken by a ThorLabs CMOS camera. The light intensity varies and decrease rapidly for the long side.

since the mirrors in the beam for both “on” or “off” state. In other words, we would waste substantial power to build a strong box by using a Gaussian beam directly.

So, we want to reshape the gaussian input beam before it reaches the DMD. Our goal is to increase power efficiency for the box, so let's look at the geometry of the box first. The box is designed to be long in the axial direction (z) and relatively short in the two radial directions (x and y) for three reasons. First, this is similar to the shape of the FORT, which makes the loading from the FORT to the box easier.

Second, uniformity is the most important condition we want to realize for the studies of 3D hydrodynamic transport properties, especially for the directions we integrate through. In our relaxation experiment, the imaging beam is integrating through the atom sample (y direction) to give a 2D density profile. We then integrate through the radial (x) direction, which is along the perturbing potential, to get a 1D density profile. Hence these two directions need to be very uniform. Due to the confining effect of the magnetic curvature (see Sec. 3.3.4), the longer the box, the more density variations of the atom cloud. Also, we need to maintain a high atom density to ensure the relaxation is in the hydrodynamic region. So a shorter box dimension in the x and y directions is preferred.

Third, the box should be long in the axial (z) direction, since we apply the periodical perturbing potential across the sample in this direction. The perturbation needs to be at least of a few spatial periods, as needed for a good data analysis. The perturbing wavelength cannot

be too short due to limited DMD dynamic range. Also, the hydrodynamic requirements (the long wavelengh limit, see chapter 5) prefer long perturbing wavelength. Moreover, although we can model the evolution of the gas by considering the edge reflection of the box walls, it is much more convenient to focus on a central region, where the walls have no affect (see chapter 4). This again requires a longer z direction length for the box since we can then leave off the close-to-box region for modeling.

Based on these considerations, we chose the x and y width of the box to be about 50 $\mu$m, for good uniformity and high gas density. The width is slightly bigger than the radial diameter of the FORT after forced evaporation (the diameter varies a little depending on different final trap depth), so that we can load the atoms from the FORT into the box without radial clippings. The z length of the box actually varies in our experiment, depending on desired temperature, density, and spatial perturbation wavelengths. We actually use a box length from 110 $\mu$m to 180 $\mu$m in the experiments. Fig. 3.8 shows the geometry of the box with respect to the bias magnetic coils.

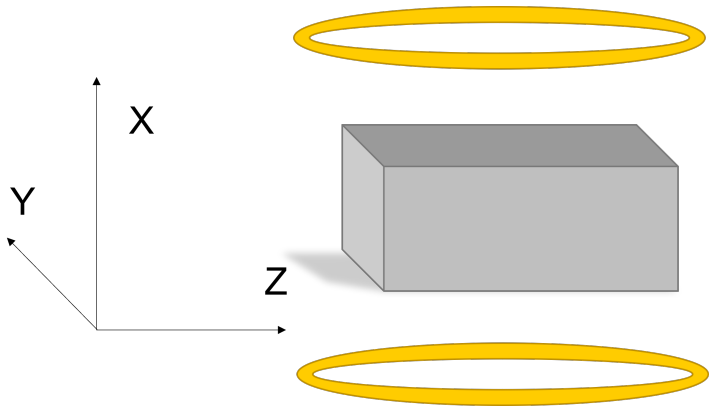


Figure 3.8: Illustration of the box position, with respect to the magnetic coils proving high field (832 G).

To realize a more efficient setup for the box shape above. We first tried is to use a cylindrical telescope to expand the gaussian beam in one direction (for the long side of the box). This application improves the power efficiency for building longer boxes. For a

gaussian beam, the spatial intensity distribution takes the form of:

$$\begin{aligned} I(r,z,\phi) &= \frac{I_0}{1+(z/z_0)^2}\exp\left\{-\frac{2r^2}{w^2}\right\} \\ I_0 &= \frac{2P_0}{\pi w^2}, \end{aligned} \tag{3.6}$$

where $w$ is the $1/e^2$ radius of the beam and $r$ is distance from the propagating axis.

Fig. 3.9 shows simple calculations of the relative intensity at a fixed distance $r$ as function of the ratio of $w/r$. We can find an expanded gaussian beam increases the intensity far away from the peak.

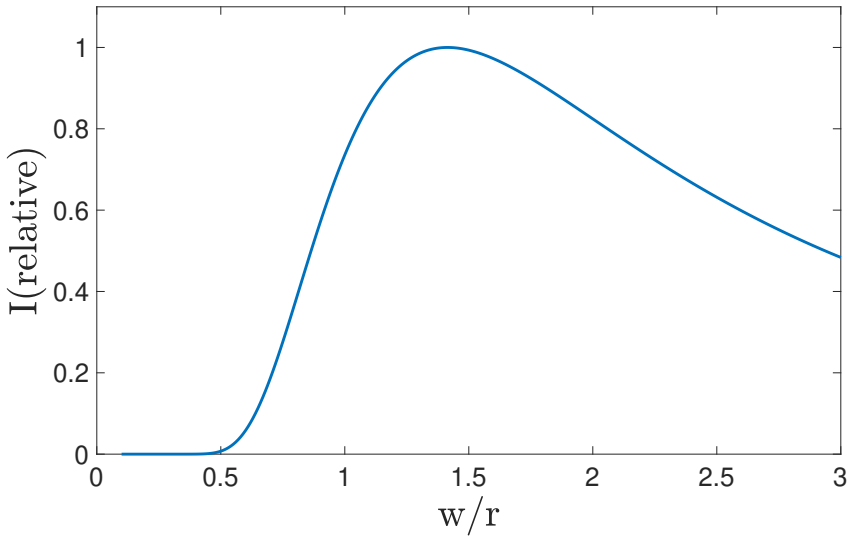


Figure 3.9: A simulation of the relative intensity, as a function of the ratio of the radius(distance to the center) to the gaussian width. A certain radius prefers one optimal width; for radius larger than the Gaussian width, expanding the beam will increase intensity.

However, this method has two shortcomings. First, the beam profile is still a gaussian in each of the perpendicular directions, which means the peak intensity is still in the center. Second, one cylindrical telescope with a fixed magnification only works best for one box length. When we use boxes of different sizes in the experiments, some of them are not optimized.

Fortunately, we found a newly developed optical element that can make the beam much

better for our box. The "Top-Hat" (TH) beam shaper is a phase element, mainly based on diffractive technology (Diffractive Optical Element - DOE). This shaper is used to transform a near-gaussian (TEM00) incident laser beam into a uniform-intensity spot. Based on different diffractive structures for the element, the spot can be either round, rectangular, square, line or other custom shapes with sharp edges in a specific work plane. This is a perfect choice for our beam shaping with two advantages. First, by transforming a gaussian spot to a uniform one, it increases the power efficiency significantly. When we focus the uniform spot on the DMD, the intensity of light for the box walls is the peak intensity. This allows us to utilize maximum power handling of the DMD to build a strong box.

The second advantage is that a uniform input beam profile makes optical potential crafting much easier. When we design the patterns for applying a perturbing potential on the DMD, for a gaussian incoming beam, we need to consider the gaussian envelope. The desired potential should be the desired pattern multiplied by the gaussian profile of the incoming beam. However, for a uniform spot, the desired potential is the same as the DMD pattern.

There are two types of TH beam shapers in terms of the focal point. One focuses at infinity and one focus at a fixed focal point depending on a build-in lens. Also, each TH beam shaper is designed for one particular input beam size, wavelength and output spot shape and size.

Fig. 3.10 demonstrates a typical setup for the application of the TH beam shaper. Note that we use a *round* spot in our experiments instead of the squared one shown in Fig. 3.10. This figure is only for demonstration.

We use a Holo/Or TH-228-Q-Y-A "Top-Hat" beam shaper. It takes a Gaussian beam of 3 mm width and transforms it to a round uniform spot with 1.5 mm diameter near its focus. A simulation tool made by the company helps us to find this element, which best fits our application. The simulation result for the designed intensity profile is shown in Fig. 3.11.

The TH beam shaper is designed for highly uniform images and superb accuracy output shape. For better performance, some considerations are needed for setting up the beam path. The element is

(a) Sensitive to X-Y displacement;

(b) Sensitive to input beam diameter;

(c) Sensitive to working distance;

(d) Requires $M^2 < 1.3$ (higher value will result in poorer results), where $M^2$ is the quality factor;

(e) Some designs are rotation sensitive (mainly, non-radial designs).

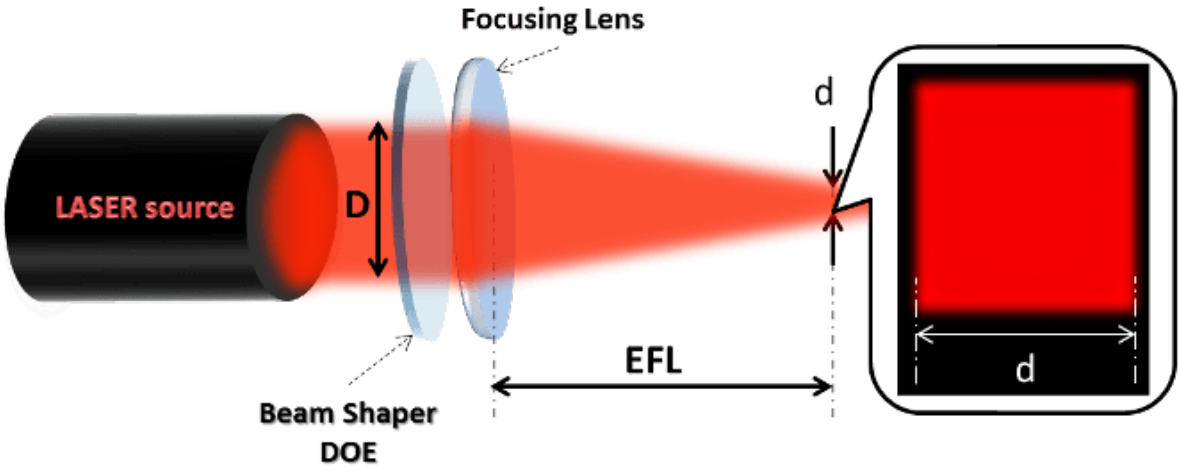


Figure 3.10: Typical setup for the "Top-Hat" beam shaper, including a collimated laser beam, a beam shaper element, a focusing lens and a focal plane for the application [THS]. EFL is effective focal length, $D$ is the input beam size, $d$ is the spot size. Figure only for demonstration, we actually use a round spot in the experiments.

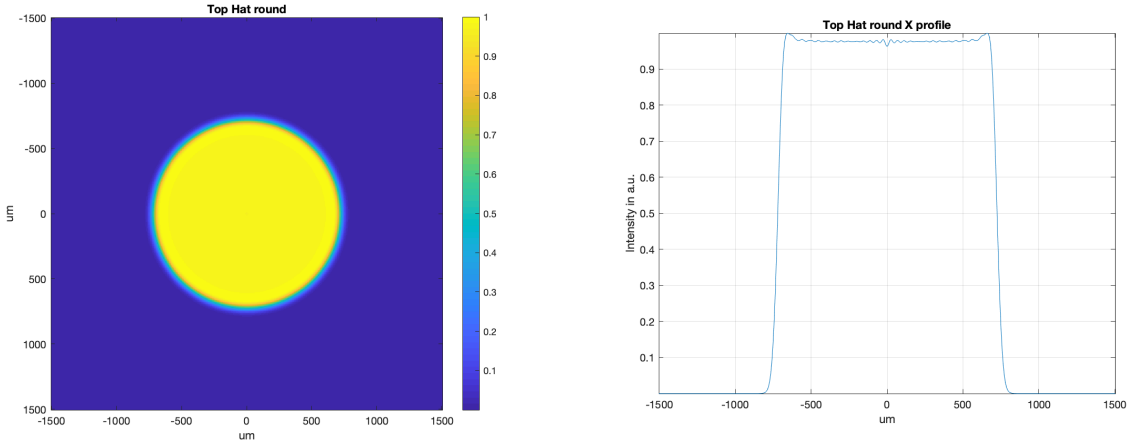


(a) 2D spot profile

(b) Intensity along radial axis

Figure 3.11: Simulation results for the designed intensity profile for a TH-228-Q-Y-A "Top-Hat" beam shaper, with 3 mm input beam size and a perfect alignment. Image of the actual spot in experiments is shown in Fig. 3.12.

The solutions for our optical system to fulfill those requirements are

(a) We put the element on a X-Y-Z micrometer translation stage.

(b) We use custom high power fiber collimators for ideal output beam size, and we use an adjustable beam expander for fine controls.

(c) An additional long Z translation stage provides larger range for axial positioning.

(d) We use high quality Toptica diode laser and high power fiber.

(e) The element is mounted in a premium mirror mount for fine tilt control. We use *round* spot shape for better flexibility for box orientations.

With these added features to a basic TH beam shaper setup, we actually have the ability to customize the final spot for the DMD. In practice, we align the TH beam by placing a ThorLabs DCC1545M CMOS camera ($\sim 5.3\mu$m pixel resolution) at the focal plane of the microscope objective, which we use to de-magnify the DMD pattern (see Fig.3.3). We first turn the DMD to an all on state, so it acts as a mirror. We adjust the expanding telescope until we see a nice round spot with clear edges on the camera. Notice that the intensity distribution may not be uniform at this point. We then pick up the X-Y-Z position and the rotation of the TH beam shaper to carefully distribute the intensity, making it uniform, see Fig. 3.12.

Next, we use the DMD to generate the pattern for our box frame, and watch how it overlaps with the TH spot. The position of the box pattern can be changed digitally by editing the uploaded image, and the TH beam can also be moved across the DMD surface. By adjusting both ways, we can realize a very good near uniform TH spot, with a little more intensity on the outer edge on purpose. Examples of a good TH beam profile and a box frame made by the TH beam combined with the DMD are shown in Fig. 3.12. These images are $\sim 250\mu$m long, about the same size as those on the atom cloud. The axial diffraction pattern on the TH spot is an artifact of the camera.

Actually, with our setup described above, we can intentionally change the input beam size, tilt or defocus the TH beam shaper to put more intensity on the box walls. We can also use this trick to make the most power efficient configuration for each box of different size. Since we have an adjustable expanding telescope, the most convenient way to modify the spot profile is to change the input beam size. With the other conditions being ideal, we use the simulation tool to predict effect of beam size change on the spot profile. The result shows when the input beam size changes, at the same focal plane, the profile in radial direction varies from a gaussian-like one for smaller beam to a hollow one for bigger beam (see Fig. 3.13).

By using the top hat beam shaper with an adjustable beam expander, we make the best use of the DMD as a dynamical spatial light modulator to build a strong optical box.

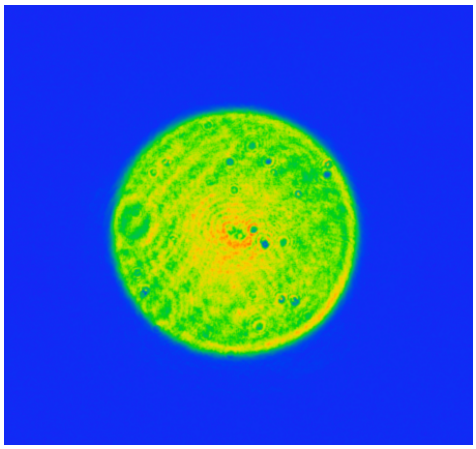

(a) Top Hat beam profile.

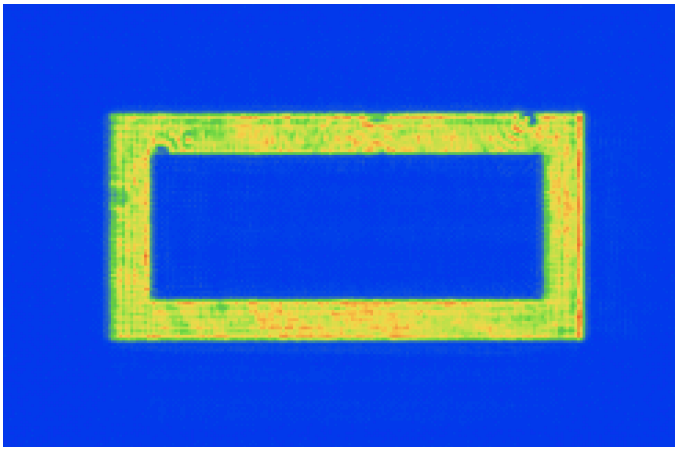

(b) A box pattern on the TH beam, shaped by the DMD.

Figure 3.12: CMOS camera images of typical Top Hat beam applications. The disk in (a) is about 250 $\mu$m in diameter. The box pattern in (b) is about 200 by 95 $\mu$m. This figure is just to show our capability of making very shape edges, the box we actually use in experiments are much thicker to prevent atoms from accumulating outside of it and affecting the image (see Sec. 3.4).

### 3.3.4 Alignment of the Box

We have all the optical elements to make the box now. The only remaining question is where to position the box in the main chamber. Recall that during the entire trapping procedure, the atoms are loaded to three different traps: the MOT, the FORT and the box. Since the box is the final trap where we perform the experiment, we need to carefully position it in the best place to make the other traps overlap with it.

At high field, the magnetic field is generated by two coaxial coils running parallel current. The coils generate a large field (832 G), on top of the dipole trap. The finite size and distance of the coils result in a slowly varying field, which has a cylindrical symmetry. Here, a potential is generated by the magnetic field due to the field curvature. Let us consider a virtual move of the atom cloud in the bias magnetic field. Based on the geometry of the field, if we assume the trapped atom cloud is located in the center. When it moves along the x axis, the magnetic field it experiences will increase; and when it moves in the y-z plane away from the x-axis, the magnetic field drops.

To understand the magnitude and direction of the magnetic force, we need to review the basic atomic structure for the $^6$Li. Note that we use a $|1\rangle, |2\rangle$ mixture of the lowest ground states. These states are highfield seeking, i.e., when placed in a magnetic gradient,

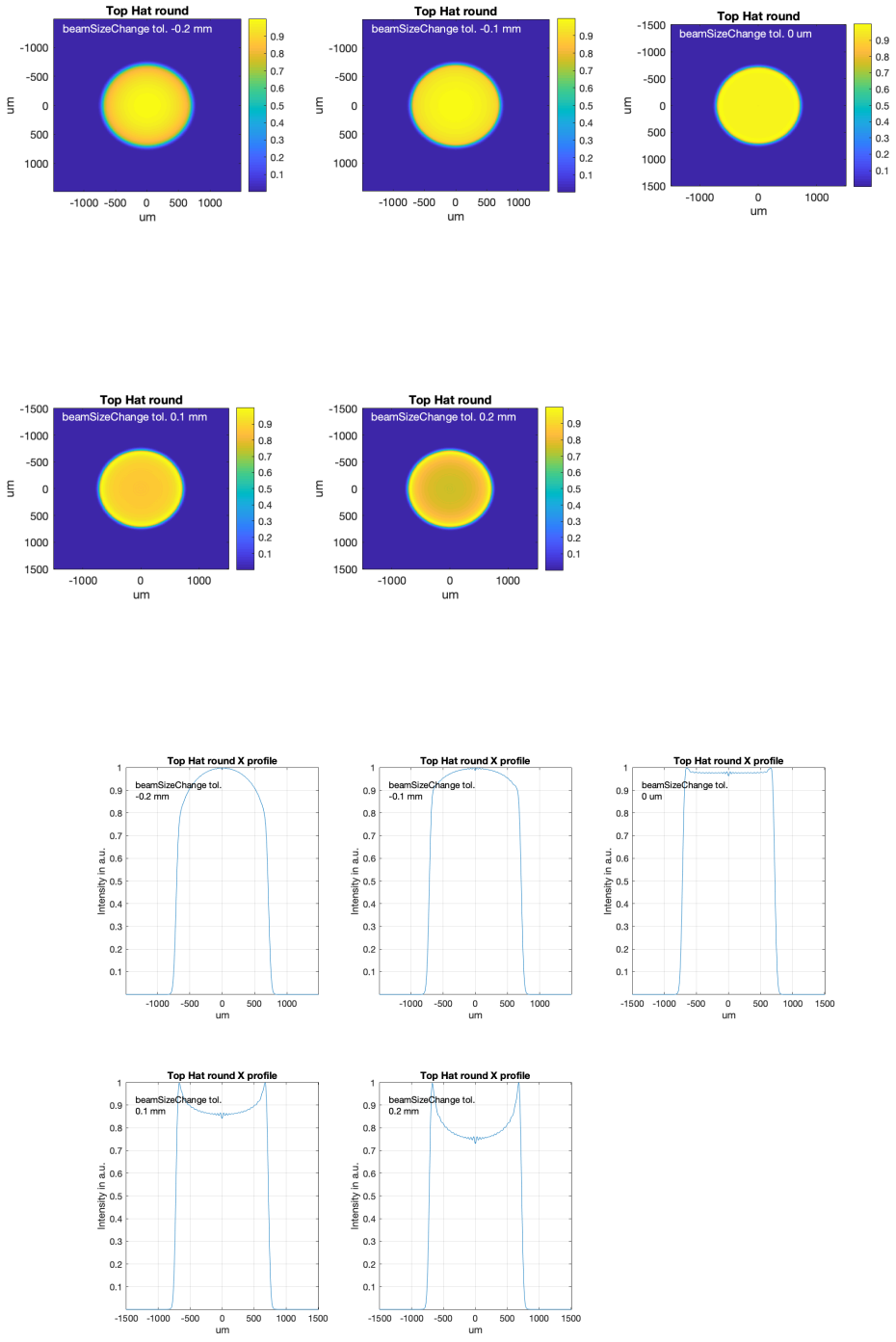


Figure 3.13: Simulation results for a beam width departs from 3 mm. A larger beam is transformed to a hollow top and a smaller beam is transformed to a gaussian-like top. Above are 2-D spots at focal plane; Bottom are radial intensity profiles.

they are drawn to regions of high field. As a result, the potential is attractive in the plane perpendicular to the axis of the magnet coils (horizontal y-z plane) and repulsive along the axis of the coils (vertical x-axis), see Fig. 3.8. The net magnetic potential can be written as harmonic oscillator potentials for a simple magnetostatic treatment:

$$U_{mag} = \frac{m}{2}(-\omega_{mx}^2 x^2 + \omega_{my}^2 y^2 + \omega_{mz}^2 z^2). \tag{3.7}$$

The magnetic dipole moment $\boldsymbol{\mu}$ of the atom will align itself with the local magnetic field direction, so we have $U_{mag} = -\boldsymbol{\mu}\cdot\boldsymbol{B} = -\mu B$. Maxwell's equations require $\nabla^2\boldsymbol{B} = 0$, and comparing the two forms of U we have,

$$\nabla^2\boldsymbol{B} = \nabla^2(\frac{-U_{mag}}{\mu})\,\hat{x} = 0 \tag{3.8}$$

$$-\omega_{mx}^2 + \omega_{my}^2 + \omega_{mz}^2 = 0. \tag{3.9}$$

From cylindrical symmetry, we have $\omega_{my}^2 = \omega_{mz}^2 = \frac{1}{2}\omega_{mx}^2$, hence the vertical magnetic force is twice as big as the horizontal force.

Also, note that our magnetic field gradient is small, so the effect of gravity cannot be ignored since it's comparable to the magnetic force. Together, the total potential due to gravity and magnetic force is referred as the "magnetic bowl".

We need to align our box in the center of the magnetic bowl, where the horizontal magnetic force is minimized and radially symmetric on the atom cloud. The vertical position can be set a little off the geometric center, so the magnetic force is pushing the cloud center up to cancel the gravity. In such a configuration, the net force on the cloud is minimum and the density along x (vertical) is roughly symmetric along the center. We hereby can call this location the "center" of the magnetic bowl.

The way to center the box in such position is to do a so called "Slosh Mode" experiment, which is to release the atom from the optical trap to the magnetic bowl. It is obvious that we always want to overlap the box with the FORT for the best loading. So we can start the best-position search with atoms releasing from the FORT. For the horizontal plane, when we release the gas from a position that is not centered, the gas will migrate towards the magnetic potential center. The center of mass motion can be monitored by eye coarsely and by computer finely to direct us to the center of the magnetic bowl. The magnetic coils are fixed so we can move the $CO_2$ beam focal point by translating focusing lens to change the FORT position. Repeating so leads us to center the FORT in the magnetic bowl. For the vertical direction, we basically follow the same procedure, but it's a bit harder since the

atom cloud expands in a repulsive potential. However, since the vertical magnetic force is twice bigger than the horizontal forces, the vertical alignment of the box is more critical. A better way for adjust the position finely is to load the gas to the box from a good FORT position and measure its density profile. The x profile obtained by the horizontal view camera should be symmetric about the vertical center, and a little curved to the top and bottom when the box is in the correct position. We can also use this method to find the horizontal center better.

Note that for different final depths of the forced evaporation stage, which determines the temperature, the atoms are actually sitting at different places due to thermal effects on the focusing optics. So for each different final FORT depth, we need to repeat the search procedure and re-align the $CO_2$ beam.

## 3.4 Box Loading and Perturbation

Before I describe how to load the atoms to the box, there is another consideration for the box potential. We have a good understanding and control for the atoms inside the box now, but the atoms outside the box could also affect our observations. For our imaging system, the CCD camera integrates through the whole optical path and cannot distinguish the atoms inside the box from the atoms outside.

From the example of the slosh mode experiment, we know that without any other confinement, the magnetic force will push the atoms away from the vertical center and attract them to the center of the magnetic bowl in the horizontal plane. When we load the atoms from the FORT to the box, we cannot catch all the atoms in the long axial direction for high temperature cases, since the FORT is longer at higher depth. For such situations, we need a repulsive potential to keep the atoms away from the box walls.

This can be done simply by creating proper DMD patterns for both directions. For the vertical DMD, we can turn all the mirrors on except those inside the box. Although the box frame width does not affect atom trapping since the trapping potential only depends on how sharp the edge is, a wider frame repels the atoms outside the walls to prevent them from entering the imaging path of the box. On the other hand, for the horizontal DMD, we can make the length of the top and bottom bars barely longer than the box, so the atoms outside of the box can escape easily.

Actually, with the possible capability to edit an arbitrary optical potential. The DMD - TH beam shaper system can be utilized to create a balancing potential of the magnetic

bowl. The density variation caused by the magnetic curvature can therefore be improved or eliminated, giving us a one level more uniform box for the next generation experiments. To realize this, I have two constructive ideas. The dynamic range of the DMD is limited by the area illuminated on the array, so it may not be enough for the current optical setup, since the magnetic potential is small compared to the box depth. So, one could design an appropriate duty circle[2] for the mirrors to apply a grayscale projection, which effectively increases the dynamic range. The other idea is to adjust the beam expanding telescope for the top hat beam shaper to generate a somewhat hollow intensity profile. This would help since we need more repulsive force further away from the center of the magnetic bowl to cancel the stronger magnetic force.

### 3.4.1 Box Potential

With the box set up and positioned properly, the last quest to prepare our sample is to load the atoms to the box $U_0(\boldsymbol{r})$ and generate a perturbing potential $\delta U(z)$ in the long axial direction.

The box loading procedure comprises releasing the atoms from the FORT and capturing them by the box beams. Regarding general expansion dynamics, atom clouds confined in optical traps expand more rapidly as the optical trap oscillation frequencies are increased. Since the region we are interested in is at very low temperature, we always use very shallow FORTs (low frequencies), where the gas expands slowly. Also, our box walls are very close to the atom cloud in the FORT. So the atoms will flow gently into the box when the FORT is extinguished, and there is no need for controls slow release.

Hereby, for the release, we simply turn off the RF signals applied on the $CO_2$ AOM. This makes all the $CO_2$ beam goes to a beam dump, thus extinguishing the FORT. We use an RF switch to turn off both the 40 MHz and 32 MHz signals to ensure that there is no $CO_2$ beam, diffracted by the AOM, leaks to the box and affect the cloud.

For the box beams, we need to treat the 532 nm beam for the frame and the 669 nm beam for the top-bottom sheets differently. Notice that an atom cloud in the FORT is long in the z direction and short in the x-y directions, see Fig. 3.14.

When aligning the box with the FORT, we can make the x and y-side of the box wider than the FORT, while the z-side is shorter or comparable to the FORT. This is due to our system limitation for the box length, and also to obtain high atom density. Since the box

[2] A duty circle is to create a serials of DMD patterns with desired holding times. For a observation time scale much longer than the holding time for each pattern, the observer sees an averaged image of those patterns.

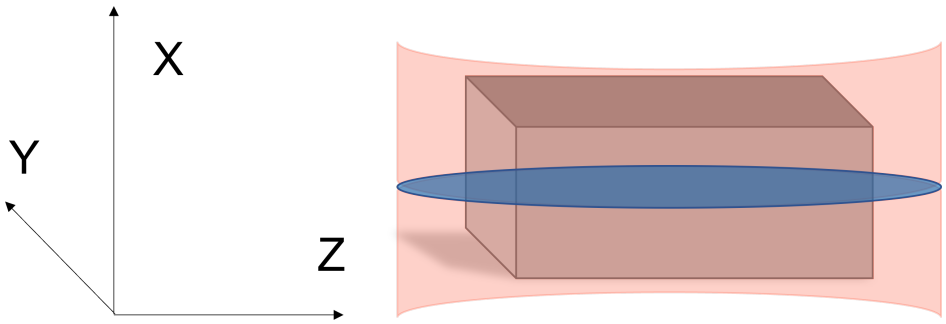


Figure 3.14: Relative position of the box, the FORT and the atom cloud during the box loading. Blue: atom cloud; Pink: FORT at final depth of forced evaporation; Gray: the optical box.

potential is partially overlapped with the FORT, it is better to ramp up the box beam slowly to avoid abrupt kicks on the atoms. We ramp up the power of both 532 nm and 669 nm beams from 0 to maximum in 0.5 second while the FORT is sitting at its final trap depth.

Note that our 669 nm beam is only 2 nm away from atomic resonance. Although it doesn't resonantly interact with the atoms when used for box trapping as mentioned previously, we need to be careful not to let any red beam go to the main chamber before the box loading stage. We use a mechanical shutter to block the red beam before we trigger the ramping. Since a mechanical shutter has a finite response time, we want to open it a little earlier (50 ms) than when the beam is needed. We put an "all off" pattern on the DMD for 100 ms before switching to the two bars pattern to ensure no light leak to the atom cloud.

With these methods, we are able to load the atom cloud from the FORT into the box without a significant change of temperature or atom number. Before the gas re-thermalizes in the box, there is an optional step. Sometimes we want to study the gas in a smaller box for higher density. We can use our longest box to catch as many atoms as we can from the FORT, and then perform a near isothermal compression by squeezing the box slowly. Such a step can be accomplished by using the dynamic feature of the DMD. Instead of using a static pattern of a box frame, we generate a series of shrinking boxes that share the same center position for the vertical beam DMD. By choosing an appropriate display-switching interval, we can effectively squeeze the box. Here, again thanks to the application of the top-hat beam shaper, we don't need to worry about a varying beam intensity that would affect this process.

After loading the atoms into the box, we allow 50 ms for the gas to reach thermal equilibrium. The box potential $U_0(\boldsymbol{r})$ yields a rectangular density profile with typical dimensions

$(x, y, z) = (52 \times 50 \times 150)\,\mu$m, see Fig. 3.15. The density varies slowly in the direction of the long ($z$) axis, due to the harmonic confining potential $\propto z^2$ arising from the curvature of the bias magnetic field, which has little effect on the shorter $x$ and $y$ axes. The typical total central density is $n_0 = 4.5 \times 10^{11}$ atoms/cm$^3$, with the Fermi energy $\epsilon_{F0} \equiv k_B T_F = k_B \times 0.22\,\mu$K and Fermi speed $v_F \simeq 2.5$ cm/s. The box depth $U_0 \simeq 1.1\,\mu$K.

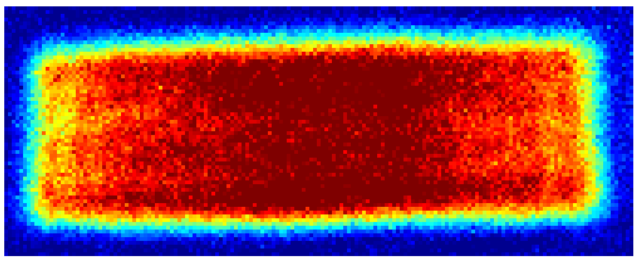

(a) Horizontal view of the box.

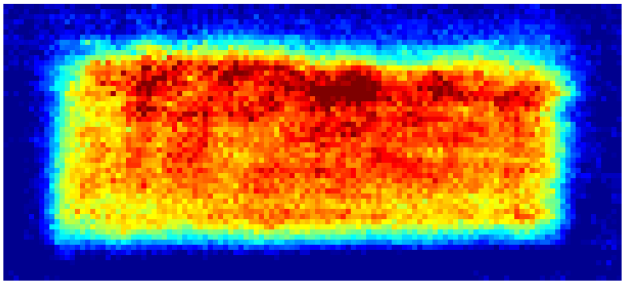

(b) Vertical view of the box.

Figure 3.15: 2D absorption images from the horizontal and vertical directions. The box dimension is roughly 52 (x) by 50 (y) by 160 (z) $\mu$m. Upper(lower) image pixel size, which is the camera pixel size divides by magnification, is 1.06(1.34) $\mu$m.

Fig. 3.15 shows typical 2D column density views for a long box (160 $\mu$m). Ideally, we would like to do all the experiments in the same box with the same density, and only change the reduced temperature $T/T_F$ and the perturbing potential $\delta U(z)$. However, in the real world, it is difficult to keep the density the same for different temperatures, since our atom cooling technique is dependent on the degree of evaporative cooling. A lower temperature

is realized by more evaporations which also results in fewer atoms remaining in the FORT. Also, our current box potential $U_0 \sim 1\mu$K, limited by the DMD damage threshold, is not enough to hold atoms of both high density and high temperature.

So changing the box size and the way to load the atom from the FORT is a more practical way to do the experiment. In fact, the box length we use is from 110 $\mu$m to 160 $\mu$m. A bigger box yields lower density, which helps us investigate the gas at higher reduced temperate. Meanwhile, we need to keep the density high enough for staying in the linear hydrodynamic region (see Sec. 5.3), as well as for good imaging signal to noise ratio. Accordingly, a variety of density, from about $3 \times 10^{11}$ to $6 \times 10^{11}$atoms/cm$^3$, is studied.

### 3.4.2 Perturbing Potential

In our hydrodynamic relaxation experiments, the initial condition is set by applying a small perturbing potential $\delta U(z)$ onto the atom cloud and waiting for equilibrium. The sinusoidal periodic optical potential is created by the vertical beam DMD, and takes the form

$$\delta U(z) = \epsilon [1 + \cos(qz + \phi)]. \tag{3.10}$$

Here, $\epsilon$ is a small amplitude coefficient, which determines how strong the maximum perturbation is. $q = w\pi/\lambda$ is the spatial frequency of the modulation and $\phi$ is a phase factor for positioning the perturbation relative to the box. These values are set as programmable input parameters to generate the DMD patterns. Note that this perturbing potential $\delta U(z)$ is built only inside the box.

We only use the binary display feature of the DMD during the experiment. For a proper interpretation of the sinusoidal potential, we need a method to write the binary pattern that works effectively as a grayscale image. A reprographic technique called "halftone" finds great usage here. Halftoning is a method for creating the illusion of continuous-tone output with a binary device. It simulates continuous-tone imagery through the use of dots, varying either in size or in spacing, thus generating a gradient-like effect. For our application, we use a "Jarvis Halftone", in which an input grayscale image is converted into a halftone image of same size using Jarvis's Error Diffusion Method (see Appendix).

Also, due to the finite aperture sizes of the projection system, the projected pattern on the atom cloud is blurred compared to the original one on the DMD. Usually blurring is an adverse effect for an imaging system. However, it actually helps us in smoothing the perturbing potential, see Fig. 3.16. The blurred halftone pattern is very similar to the desired

pattern.

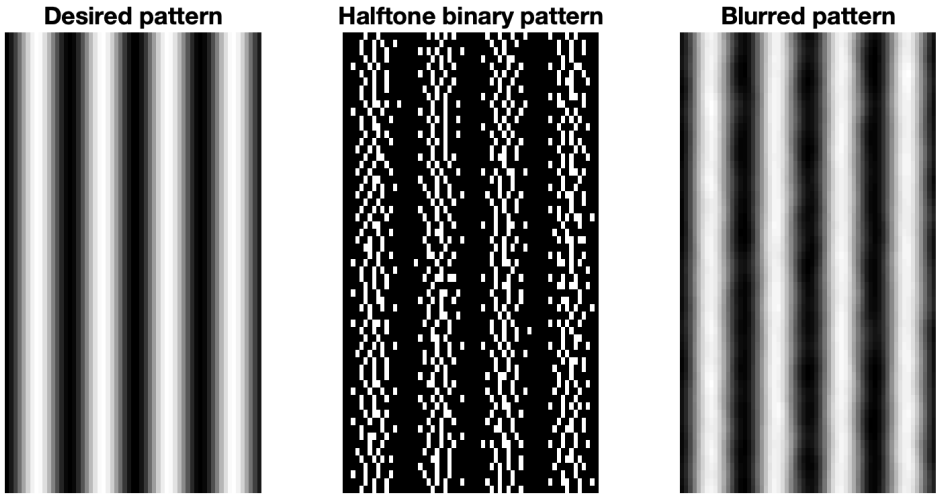


Figure 3.16: For a sinusoidal potential, the desired pattern (left); the digital halftoned binary pattern (middle); and the blurred halftoning pattern (right). A Jarvis Halftoning operation and the blurring effect of the projecting system, together, make the optical potential close to ideal.

As we mentioned in the previous subsection, we do not want to turn on a potential abruptly. In contrast, by ramping up the perturbation slowly, we are able to compress the gas almost isothermally, creating the initial density profile without changing temperature. To do so, however, the most straight-forward way of changing the beam power does not work, since the perturbing potential and the box share the same laser beam and DMD pattern. Alternatively, we can make use of the high dynamic range of the DMD to create a series of patterns for different modulation amplitudes. We divide the programming parameter $\epsilon$ to 10 segments (from $0.1\epsilon$ to $1\epsilon$) and use each of them to generate a corresponding pattern. Those patterns share the same box frame. Then we upload them to the DMD in ascending order of $\epsilon$ and set the holding times for them. In experiment, we display each pattern for 1000 $\mu$s before triggering the next to simulate a slowing ramping perturbation. The last potential is held for 36 ms to ensure sufficient thermalization.

A typical pattern for the box and the ramped up perturbation is shown in Fig. 3.17. The DMD pattern shown here has greater modulation amplitude than those we actually use in experiments for better visibility to the reader. The measured modulation amplitudes

$\delta n/n_0$ range from 7% to 22%.

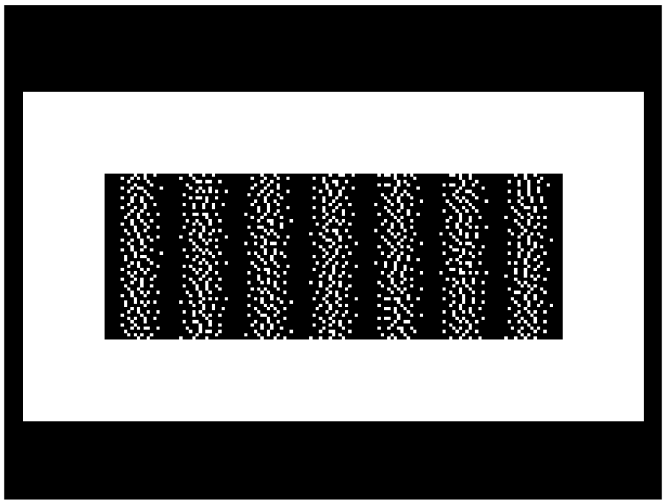

(a) DMD pattern design.

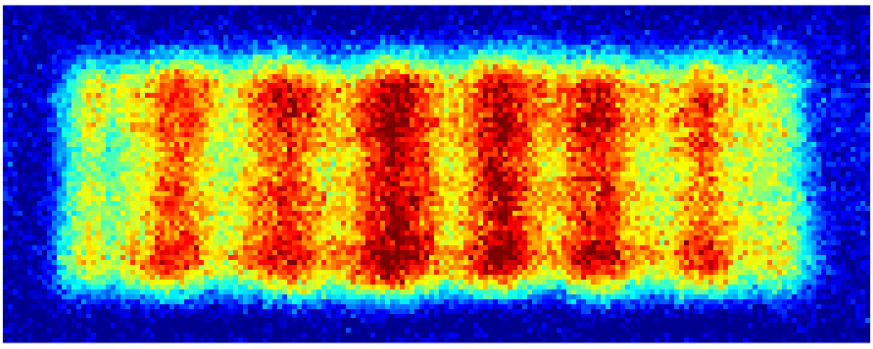

(b) Atom cloud hold by the box and perturbing potential.

Figure 3.17: Design of a sinusoidal perturbing potential (7 spatial periods of 23 $\mu$m wavelength), and the observed column density of the atom cloud from the horizontal view CCD camera.

The wavelength in Fig. 3.17 is for demenstration only so it is irrelevant. In the experiments, we use several perturbation wavelengths, from 18 $\mu$m to 42 $\mu$m to check the $q$-dependence of our measured results, which will be discussed in detail in Chapter 5. We

find that a perturbation wavelength $\lambda \simeq 23\,\mu$m yields good dynamic range for decay measurements over time scales that avoid perturbing $\delta n(z,t)$ in the measured central region by reflections from the walls of box potential, which then can be neglected (see Sec. 4.2). So most of our experiments are using a perturbation wavelength of $23\,\mu$m.

The perturbing potential is then turned off abruptly (within $10\mu$s) while the box potential stays on. The gas begins a free oscillatory decay subsequently, and absorption images are taken at desired time intervals (usually every 100 $\mu$s) to study the evolution.

CHAPTER

# 4

# DATA ANALYSIS METHODS

In this chapter, I will show the measured results of the hydrodynamic relaxation experiments and how we extract the transport coefficients. The experimental methods have been covered in the previous chapter. Here, I will start with data taking procedures and some necessary data processing methods.

## 4.1 Data Taking and Processing

After the small perturbing potential is turned off, we measure the free evolution of the atom cloud as a time varying density profile $n(\boldsymbol{r}, t)$. We need to measure the background $n_0(\boldsymbol{r}, t)$ as well, since what we study is the density perturbation $\delta n(\boldsymbol{r}, t) = n(\boldsymbol{r}, t) - n_0(\boldsymbol{r}, t)$.

A typical observation duration for the relaxation is from about 2 ms to 4 ms. So an appropriate time step to take each image is 100 $\mu$s or 150 $\mu$s. For the background, we need to be a little careful.

A perfect background $n_0(\boldsymbol{r}, t)$ should be taken at the same time as $n(\boldsymbol{r}, t)$ with all the conditions identical to it, except that there is no perturbation. However, this is impossible to do in real life. The best approximation is taking an image of the same amount of atoms at the

same temperature in the same box at the same time without perturbation. For convenience, let me call the experiment of measuring perturbed $n(\boldsymbol{r}, t)$ as the relaxation run, and that of unperturbed $n_0(\boldsymbol{r}, t)$ as the background run. We first try to measure the background in a separate background run aside from the relaxation run, by only turning the box potential on and taking images at several different times. These times are chosen to be within the range when we take images for the relaxation run. The advantage of doing so is to minimize the time difference between those two runs, so that the measured background $n_0(\boldsymbol{r})$ is close to what we want.

However, later on we noticed that there is a significant shortcoming of this method. Even though we have shown that the stored energy in the initial perturbation is very small (see Sec. 5.2.2), we find the gas has slightly different density profiles before and long after (to ensure rethermalization) application of the perturbation. Since our optical box potential is static, as is the magnetic bowl, $n_0(\boldsymbol{r}, t)$ can be treated as a time-independent quantity $n_0(\boldsymbol{r})$. Therefore we can take the background at any time as long as the gas is in thermal equilibrium. Hereby, it is better to measure the background within the relaxation run, after the oscillation dies out and thermal equilibrium is re-established. In the experiments, we usually take 20 to 30 background shots, randomly from 7 ms to 17 ms after releasing the gas, and do an average. Although those images are taken over a large time span, the density profiles show no obvious difference from each other.

Note that we have two cameras to look at the atom cloud: one views the horizontal direction and the other views the vertical direction. The imaging beams differ in frequency by about 76 MHz, so each of them can image one spin species of the mixture in-situ[1]. The images we take are processed by a converting code, which relates the extracted column density to the photon counts in each pixel and some camera characteristics to give us 2D density profiles of the atoms as function of position. Then we use a "spline" method 1-D interpolation to smoothly covert the density profiles to be in units of microns (atoms/$\mu$m).

Images taken by the vertical view camera are only used to calculate the central density in the box (see Sec. 4.3.2). The images from the horizontal view, on the other hand, are used for data analysis, as the spatial resolution is better and the images are of higher quality than those of the vertical view camera. Fig. 4.1 shows the 2D column density evolution for our coldest sample. An oscillatory decay can be seen.

Since we are only interested in the z direction where the density varies, we first integrate

[1]Note that we use a 50-50 mixture of spin-up ($|1\rangle$) and spin-down ($|2\rangle$) atoms. Their energy difference at high field of 832 G is calculated to be about 76 MHz, so each of the imaging beams is resonantly absorbed by one spin state without interrupting the other spin state, yielding in-situ imagery of both spins

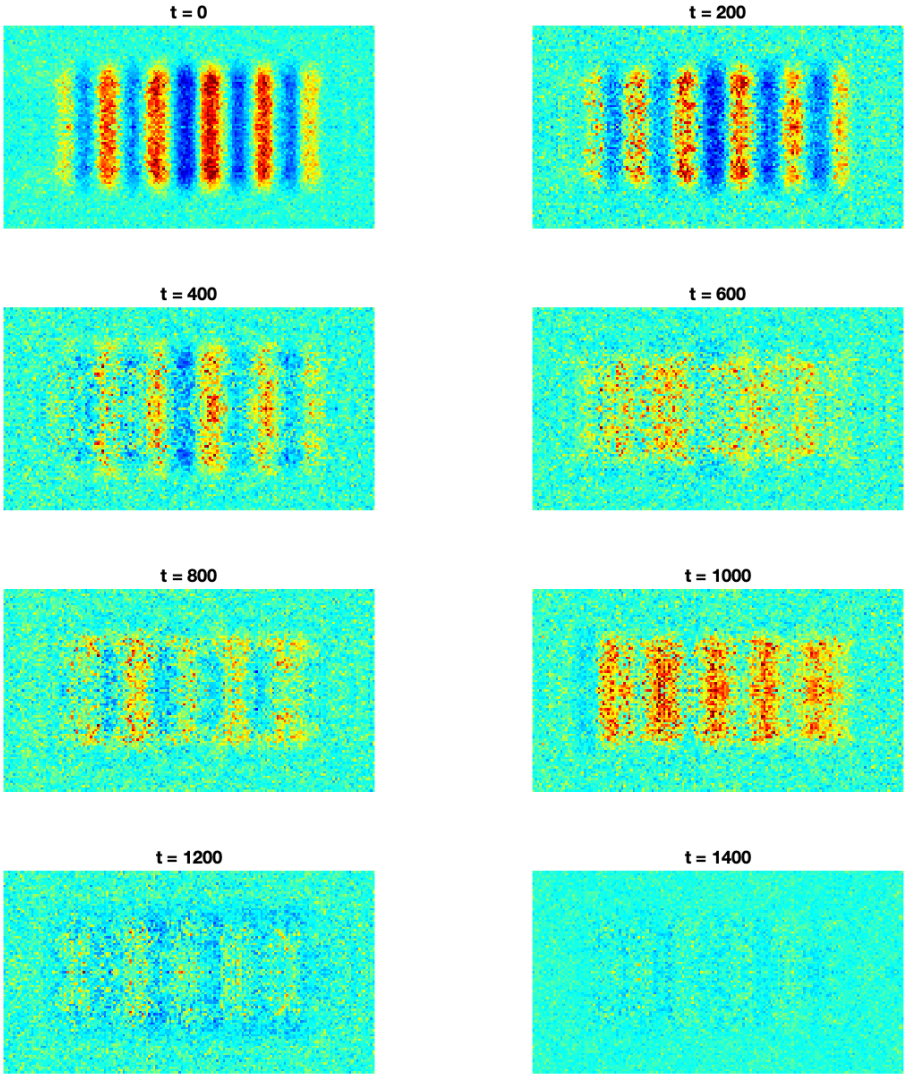


Figure 4.1: Evolution of the atom cloud in the first 1400 $\mu$s is shown as 2D column density images (using a MATLAB 'jet' colormap with a shifted zero-color for better look). An averaged background is subtracted from each image to show better contrast of the perturbations. Also, each image is averaged by a vertical-flipped "mirror" image to show better vertical symmetry. Clearly we see a oscillatory decay.

through the x direction to get 1D density profiles $n(z,t)$, $n_0(z,t)$. Actually, we find the center of the box in the x direction by a fitting and choose a region of ± 20 pixels (43.5 $\mu m$) to integrate through, since we want to avoid the edges.

Note that in real world experiments, the atom number for each run always fluctuates. To obtain $\delta n(z,t)$ correctly, we need to normalize the 1D profiles of $n(z,t)$ and $n_0(z,t)$ to the total atom number before subtraction. Also, the atom number fluctuations of the system result in statistical errors characterized by $\sigma_{n(z,t)}$, which are used later in the data analysis. Since we take a large number of backgrounds, $\sigma_{n_0(z,t)}$ can be neglected for convenience. In this dissertation, we always assume $\sigma_{\delta n(z,t)} = \sigma_{n(z,t)}$.

## 4.2 Data Analysis Methods

We have developed four methods for data analysis based on different assumptions. These methods reveal different physical insights and have their own pros and cons in practice. I will first introduce all of them and then focus on those we prefer, which enable better interpretation of the physics and are easier to use. Some results of our study are shown here to illustrate these methods.

### 4.2.1 Numerical Integration of the Complete Equations

We have already shown all the derivations leading to our hydrodynamic linear response model in chapter 2. Here, we start our data analysis from the complete time dependent hydrodynamic linear response equations for $\delta n$,$\delta T$

$$\delta \ddot{n} = c_T^2 \partial_z^2(\delta n + \delta \tilde{T}) + \frac{1}{m}\partial_z[n_0(z)\partial_z \delta U + \delta n\, \partial_z U_0] + \frac{4\eta}{3n_0 m}\partial_z^2 \delta \dot{n} \tag{4.1}$$

$$\delta \dot{\tilde{T}} = \epsilon_{LP}\, \delta \dot{n} + \frac{\kappa_T}{n_0 c_{V1}} \partial_z^2 \delta \tilde{T}. \tag{4.2}$$

Here, $c_T$ is the isothermal sound speed, $\eta$ is the shear viscosity, $\kappa_T$ is the thermal conductivity, $\epsilon_{LP} \equiv c_{P_1}/c_{V_1} - 1$ the Landau-Placzek parameter, where $c_{P_1}$ is heat capacity per particle at constant pressure and $c_{V_1}$ is heat capacity per particle at constant volume. $n = n_0$ is the initial spatially-uniform density, obtained from the central region of the atomic cloud (see Sec. 4.3.2).

Note that we have employed a one-dimensional approximation, i.e., the only spatially varying direction is z. We have also omitted the bulk viscosity term since $\xi_B = 0$ in unitary

Fermi gases [Son 2007; Elliott et al. 2014].

These equations are space-time coupled, so there is no easy way to solve the differential equations analytically. We developed a numerical integration method to simulate the density response according to these two coupled equations (see Appendix).

In the numerical integration, we vary $c_T$, $\eta$ and $\kappa_T$ as global fit parameters to find the best fit to the experimental data. $c_{V_1}$ and $\epsilon_{LP} \equiv c_{P_1}/c_{V_1} - 1$ are obtained by the equation of state, since $c_T$ is a known function of $T/T_F$ from Eq. 2.20, and $T/T_F$ yields $c_{V_1}, c_{P_1}$ from Eqs. 2.21 and 2.22 (see Sec. 2.1.2). $\delta U$ is 0 in our case, and $U_0$ will be discussed shortly.

The initial condition $\delta n(z,0)$ is given by the measured initial density profile; the initial $\delta \dot{n}(z,0) = 0$, due to static equilibrium, and the isothermal condition requires $\delta \tilde{T}(z,0) = 0$. Usually we do 5 to 8 trials for each data. However, the data at t=0 is particularly important since it sets the initial condition for solving those differential equations, so we take a total of 25 to 40 shots here to make the best measurement.

We obtain the static box potential $U_0(z)$ from the background density profile. To reduce noise and statistical errors, we do not simply use one measured background density profile. Instead, we fit our averaged 1-D background density with an analytic function (see Fig. 4.2).

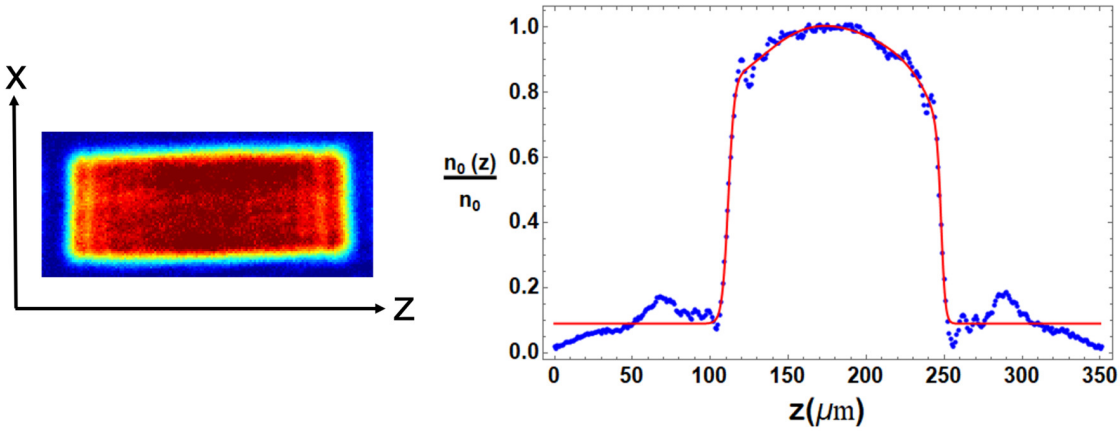


Figure 4.2: Column Density $n_0(x,z)$ and 1D background density $\tilde{n}_0(z)$ (blue dots). Red curve: Fit of Eq. 4.3.

When working on a 1-D density profile, it is convenient to refer the density to a fixed value, which we choose to be the peak density $n_0$. Note that actually we define our 1-D $n_0$ as the average density of the central 35 micron region.

The analytic function for fitting $\tilde{n}_0(z) = n_0(z)/n_0$ is a tanh function multiplied by a polynomial,

$$h(z) = \frac{\tanh[(z-z_{10})/w_1] - \tanh[(z-z_{20})/w_2]}{2} \sum_n a_n z^n. \tag{4.3}$$

The difference of the tanh functions produces a top-hat shape of nominal width $z_{20} - z_{10}$ and slopes on each side determined by $w_1$ and $w_2$. The flat top is modulated by the multiplying polynomial. Fig. 4.2 shows a typical fit using a fifth order polynomial. The density offset arises from atoms trapped outside the box, in between the repulsive sheets and the magnetic confining potential arising from the bias magnetic field.

With a smooth density profile obtained from the fit, we can now use the equation we derived in Sec. 2.1.2 from the chemical potential $\mu = \epsilon_F(n) f_\mu(\theta)$,

$$\tilde{U}_0(z) = U_0(z)/\epsilon_F(n_0) = f_\mu(\theta_0) - [\tilde{n}_0(z)]^{2/3} f_\mu\big(\theta_0/[\tilde{n}_0(z)]^{2/3}\big), \tag{4.4}$$

to obtain $U_0(z)$ in unit of $\epsilon_F(n_0)$, as shown in Fig. 4.3.

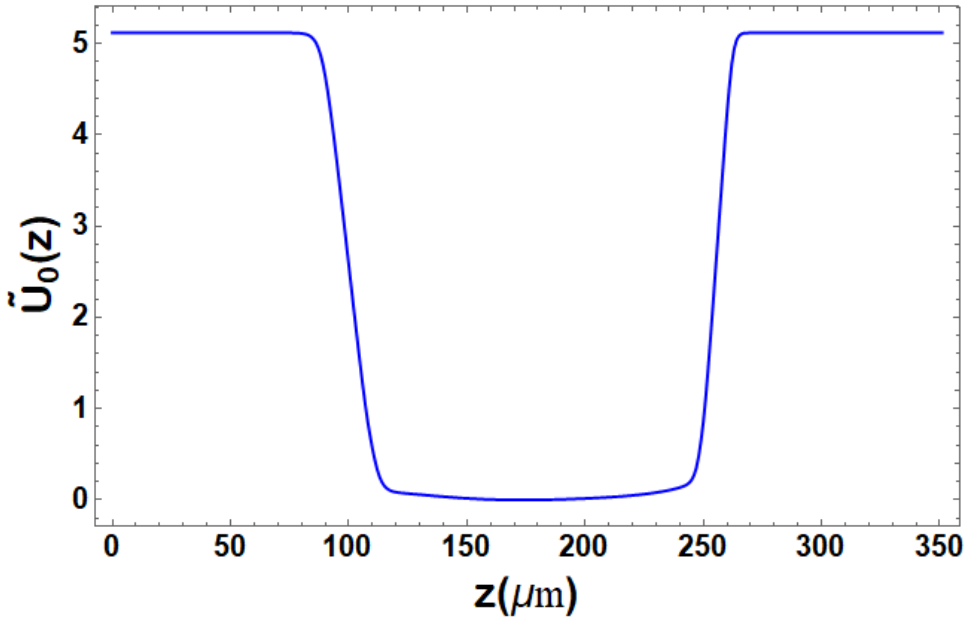


Figure 4.3: Box potential in units of local Fermi energy $\epsilon_F(n_0)$ for the central density $n_0$. The potential is determined from the measured background density $n_0(z)$ using Eq. 4.4. Note that the curvature at the bottom of the box potential energy arises from curvature in the bias magnetic field, which produces a small confining harmonic potential. A typical $\epsilon_F(n_0) \simeq 0.2\,\mu$K, and the box depth $U_0 \simeq 1.0\,\mu$K.

For finding the box potential from Eq. 4.4, the density offset in Fig. 4.2 is subtracted so that the density smoothly vanishes at the walls of the box and the peak density is scaled to 1. The central 3D density $n_0$ is determined as described below in Sec. 4.3.2. The reduced temperature $\theta_0 = T_0/T_F(n_0)$ is determined from the isothermal sound speed $c_T$, which is one of the fit parameters for the $\delta n(z,t)$ data. The box potential then determines the corresponding force $-\epsilon_F(n_0)\partial_z \tilde{U}_0(z)$ for use in Eq. 4.1. In our experiments, where $\epsilon_F(n_0) \simeq 0.2\,\mu$K, the box depth $U_0 \simeq 1.0\,\mu$K.

In our data analysis, we usually avoid the effects of the walls by choosing a central region of the atom cloud for $\delta n(z,t)$ measurement. It is worth mentioning that, for this method, including the wall potential gives us almost identical results to those without walls. However, due to finite imaging resolution and background noise, the calculation of the box depth is not precise, so it is better to avoid the walls.

Now we have everything we need for the simulation. Here, the beauty of a free evolution experiment can already be seen from this data analyzing method. The initial condition is directly measured without any approximation or involvement of free fit parameters. Comparing this method with our previous approaches of investigating hydrodynamic linear response [Baird et al. 2019], the number of fit parameters reduces by two (avoids fitting for $\delta U$ and $U_0$). Therefore, the sensitivity to the transport coefficients increases.

Starting from the spatial density profile, see Fig. 4.4, we can find the numerical integration simulates the evolution of the density profile well and we are able to catch the overall shapes of the perturbation. However, we also notice that it is easily effected by noise, some artificial pattern such as imaging diffraction and the effect of walls, especially at where the oscillation amplitude is small. A common trick to improve the performance of fittings is to apply a noise filter (low-pass filter or band-pass filter) to the data.

We take a $T/T_F = 0.28$ case as an example to show what a filter does for the fittings, see Fig. 4.4. The region of interest (ROI) for the numerical integration is chosen to be sufficiently long to cover the entire box and even outside of the box. Although the region out side of the box does not matter, it is interesting to see how the simulation evolves.

The filter we use is a band-pass filter, which selects a range of Fourier components near the peak in frequency space. When the filter is applied, it is on both the data and the initial condition $\delta n(z,0)$ for a smooth simulation. Note that we obtain the static potential term $\partial_z U_0(z)$ from a poly-tanh fitting, so it's already a smooth function that does not need a filter.

As we can see in Fig. 4.4, the band-pass filter smooths the data and the simulation, yielding a much better agreement between them. Applying a filter also restrict the changes in the density profile, so we don't run into troubles of a diverging integral or some artificial

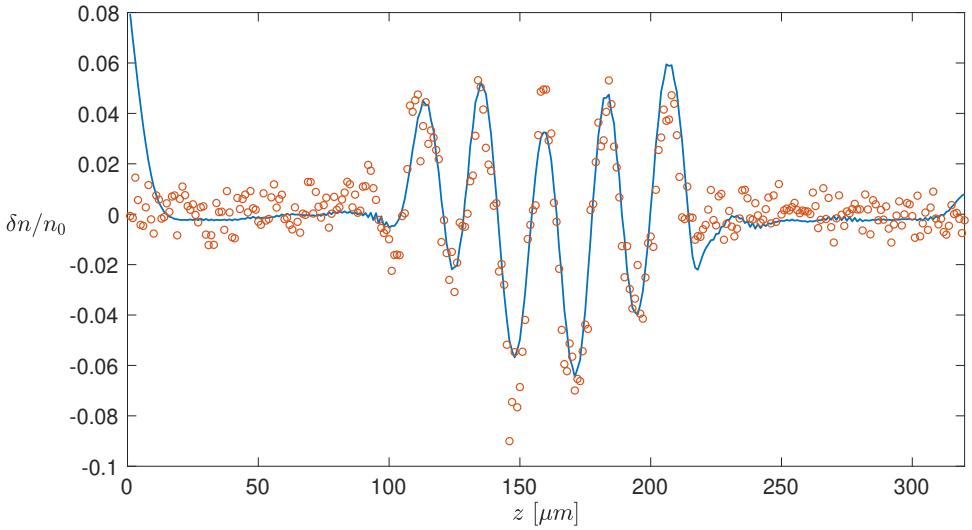


(a) No filter.

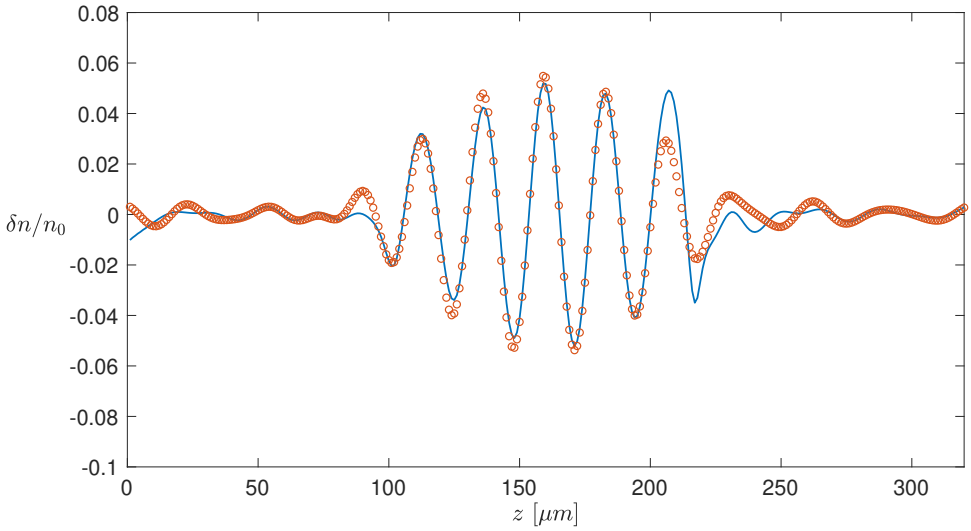


(b) With filter.

Figure 4.4: Spatial profile of measured data and numerical simulation of $\delta n(z,t)$ for the $T/T_F = 0.28$ case at $t = 0.9$ ms, with (b) or without (a) a band-pass filter based on dominant spatial frequencies. In (b), the filter is applied on both the data and the initial condition for the simulation.

walking away near edges of the region of interest.

Clearly a noise filter helps us to better extract useful information from the data. Let us think a little further. What a noise filter does for a spatial function is selecting some Fourier component in the frequency domain and transferring it back to space. However, since we

watch the evolution of a sinusoidal density perturbation, it has a well-defined wavelength.

We find that it is better to look at only the dominant Fourier component $q$, which contains most useful information, see Fig. 4.5. Also, since the evolution of the density profile can be regarded as a damped oscillator, whose characteristic frequencies and decay rates are q-dependent functions, using this method gives us clearer physical interpretations and comparisons.

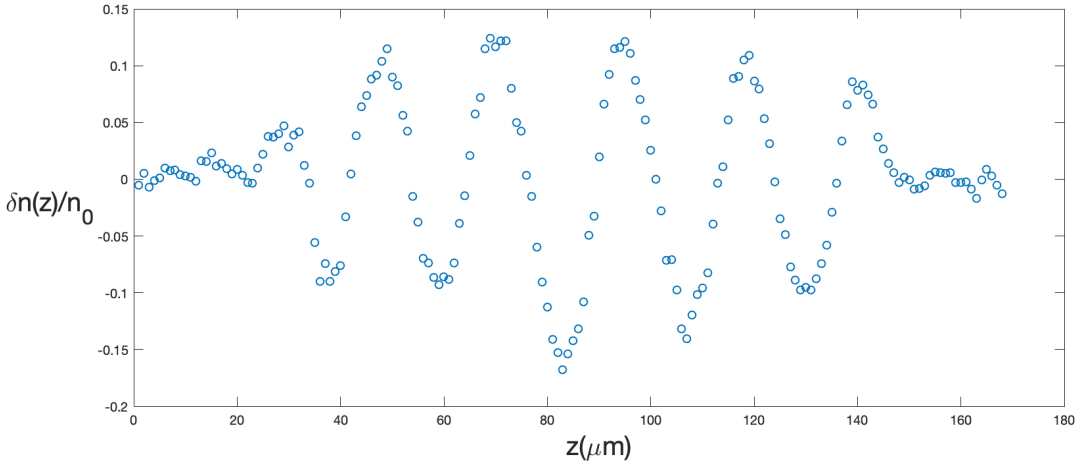


(a) $\delta n(z)/n_0$ profile.

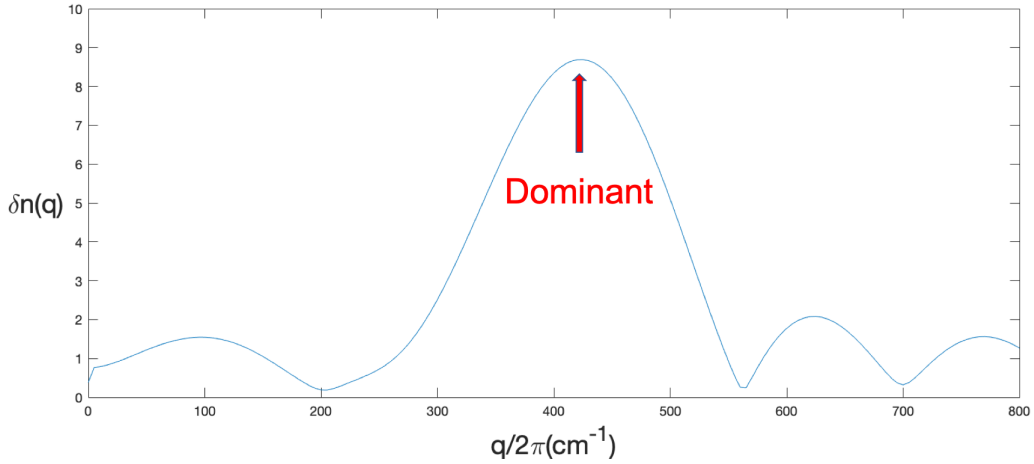


(b) $\delta n(q)$ spectrum.

Figure 4.5: Spatial profile and absolute values of the Fourier transformed spectrum at $t = 0.2$ ms for a $T/T_F = 0.28$ data. Here, q is in unit of $\mathrm{cm}^{-1}$ for convenience, since most of our calculations are in the cgs units.

We perform a fast Fourier transform of the measured density perturbation $\delta n(z,t)$ to obtain the Fourier component $\delta n(q,t)$. The wave vector $q$ is obtained by doing an averaged "findpeak" search from the data taken at first few times, when the periodic structures are clearest. The $q$ is then fixed for all the other data and for the simulations. The predicted time-dependent $\delta n_{Pred}(z,t)$, obtained by the numerical integration of Eqs. 4.1 and 4.2 can also be Fourier transformed, yielding $\delta n_{Pred}(q,t)$, which is used in a $\chi^2$ calculation to compare with the measured $\delta n(q,t)$ at each time,

$$\chi^2(q) = \sum_{t_i} \frac{(\delta n(q,t_i) - \delta n_{Pred}(q,t_i))^2}{\sigma^2_{\delta n(q,t_i)}}. \tag{4.5}$$

Here, each prediction of $n_{Pred}(q,t_i))^2$ is obtained from the simulation trial of given $c_T, \eta, \kappa_T$ as described previously. $\chi^2(q)$ has been summed over all the measurement times $t_i$.

There are different ways to obtain information from the Fourier transform. The most straightforward way is to look at the magnitude of the dominant Fourier component, which is done by taking an absolute value. However, the magnitude of a well-defined periodic function should come solely from the real part of its transform. The imaginary part contains the phase information, which ideally should be a constant. So, if we carefully choose a integer number of spatial periods to transform and set the phase to minimize the imaginary part, we can study only the real part of the Fourier transform. This yields less statistical uncertainty by getting rid of the noise in the phase. Hence, the $\sigma_{\delta n_{real}(q,t)}$ obtained this way is smaller for calculating the $\chi^2$.

We start from some reasonable guess of the fit parameters and do some coarse searches to narrow the range down. Then a multi-loop integration of fine-spaced fit parameters yields a best global fit by minimizing the $\chi^2$. The best fit is used to extract the transport coefficients, as well as the reduced temperature (given directly from $c_T$, $n_0$ and the equation of state, see Sec. 2.1.2).

To speed up the fitting process, we use the data taken at a few early times of the evolution to get a good estimate of $c_T$. The reason why we can do in this way is that $c_T$ sets the overall oscillation frequency of $\delta n(q,t)$ which can be easily determined (the evolution can be modeled as a damped oscillator, as shown in Sec. 4.2.3). $c_T$ is relatively uncorrelated with other fit parameters. Then we set $c_T$ as a constant to find the corresponding minimal $\chi^2(\eta,\kappa_T)$ by running parallel "for-loop" computations of an array of finely spaced $\{\eta,\kappa_T\}$ values. Varying the value of $c_T$ with our approximated range will lead to the global $\chi^2$ minimum. A typical surface plot of $\chi^2(\eta,\kappa_T)$ is showed in Fig. 4.6.

From the $\chi^2$ surface plot, we can see this method shows good sensitivity to both $\eta$

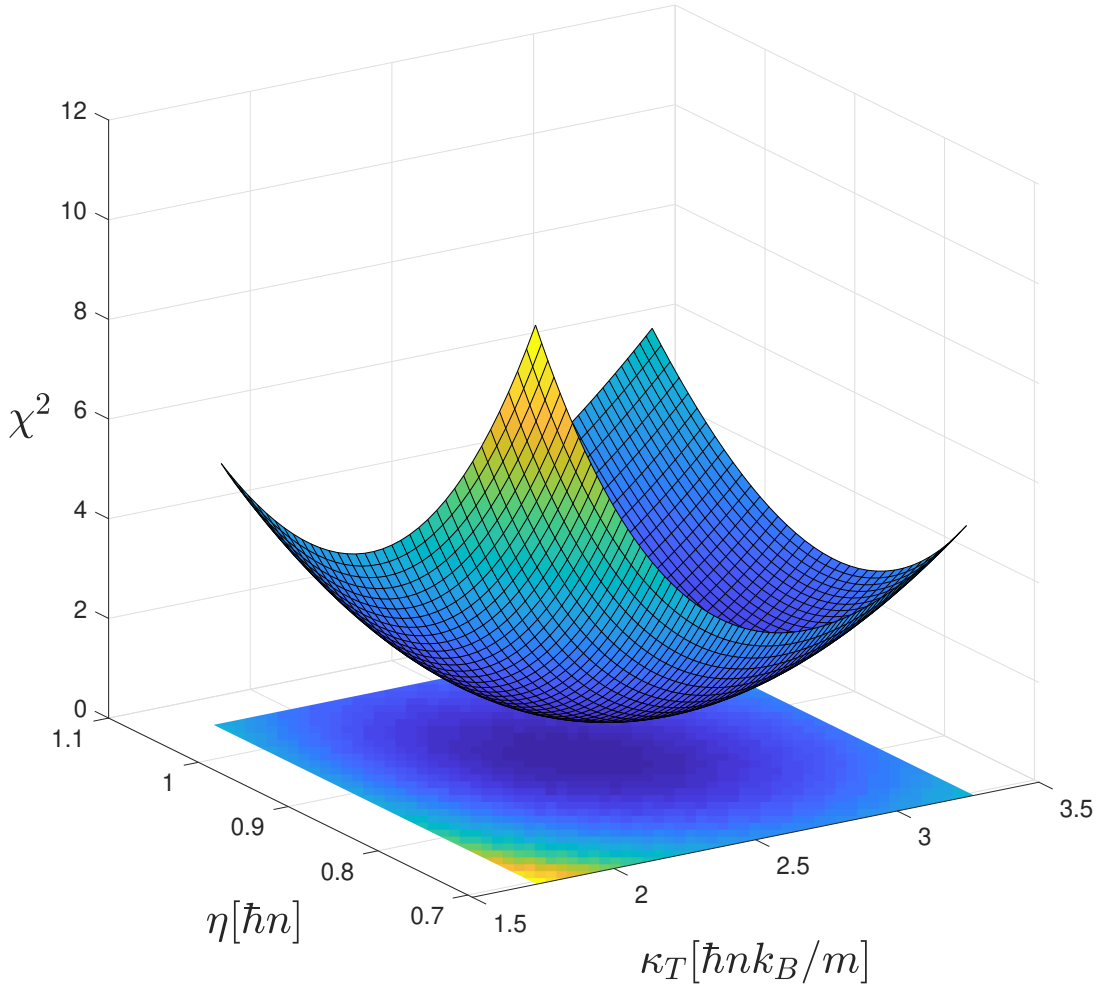


Figure 4.6: A surface plot of $\chi^2$ as function of $\eta$ and $\kappa_T$. Each $\delta n_P(q,t)$ for the $\chi^2$ calculation is obtained by performing the numerical integration for a given set of $\{\eta, \kappa_T\}$ , with $c_T$ fixed. $\chi^2$ shown here is per number of measurement times, which is summed over all the times we take measurements and divided by total number of measured times.

and $\kappa_T$. Although they are somewhat correlated, the very small number of fit parameters needed (only three) in the fitting makes it possible to extract these two important transport coefficients independently[2].

It is interesting to see how the simulations deviate from the data after a longer time

[2]Actually the physics is there are two modes evolving quite differently, which will is illustrated by the analytic fit model in chapter 2 and in later this chapter.

when we choose a region of interest close to the walls. For a low temperature $T/T_F \simeq 0.28$ data, we compare the data range of a central region of 70 micron (3 spatial periods) with one of a whole range of 112 micron (5 spatial periods), Fig. 4.7. Using this complete solution, we can see that the best fit for the first 2.5 ms holds for both cases, and deviates a little for the 112 micron case due to the effect of walls.

Also, here we can see that the simulations, with, and without, including the walls are almost identical. We see that even if the walls have influence on the atoms nearby, a Fourier transform helps us to filter out the high frequency sharp response at the walls, which makes the overall dominant q component almost unaffected.

The numerical integration method makes use of the complete hydrodynamic linear response equations of $\delta n(z,t)$ and $\delta T(z,t)$. It includes the spatially dependent box potential $U_0(z)$, so it works well even without the uniform density assumption for the z direction. It should also work for the case that the region of interest is close to or including the walls.

Although we don't use this the numerical method for our final measurements on the transport coefficients, it helps to determine the time scale over which the box potential has a negligible effect on the spatial region of interest, enabling the determination of an analytic fit function for $\delta n(q,t)$, which we will discuss later. While this method already works well for our study, we are motivated to develop some other methods for three reasons.

First, this method is very slow. This numerical integration is done by step by step calculations, or in other words, by "brute force". The number of iterations can be huge for a fine-step simulation towards a long end time, with finely spaced fit parameters. In fact, during practice, we are interested to investigate what different fitting regions both in space and time could affect our results, so we may need to run the simulation many times for a single peace of data. Therefore, we prefer much faster methods.

Second, this method relies significantly on an accurate measurement of the density profile at $t = 0$, which sets the initial condition for the integration. In principle, we could add a free fit parameter to compensate for a small uncertainty in $\delta n(q,0)$. However, this could reduce the performance of the fitting and will definitely make it even slower. So, to make the method work better, we need to take more data at $t = 0$ to get the best average of the density profile.

Third, although this method is able to extract the shear viscosity coefficient $\eta$ and the thermal conductivity $\kappa_T$ independently, it does not provide clear physical insights why we can distinguish these parameters. We would like to unravel the contributions for each of them to the evolution of the gas.

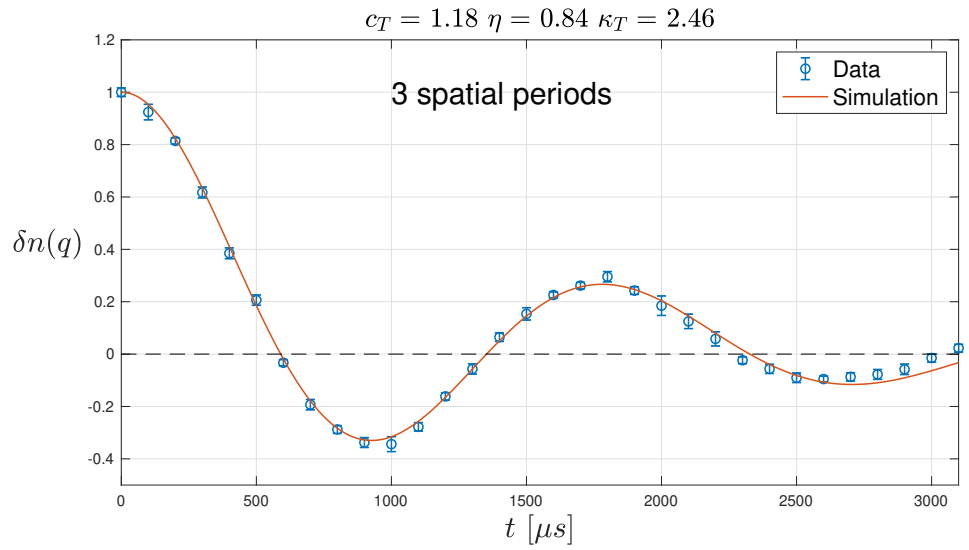


(a) Central 3 periods.

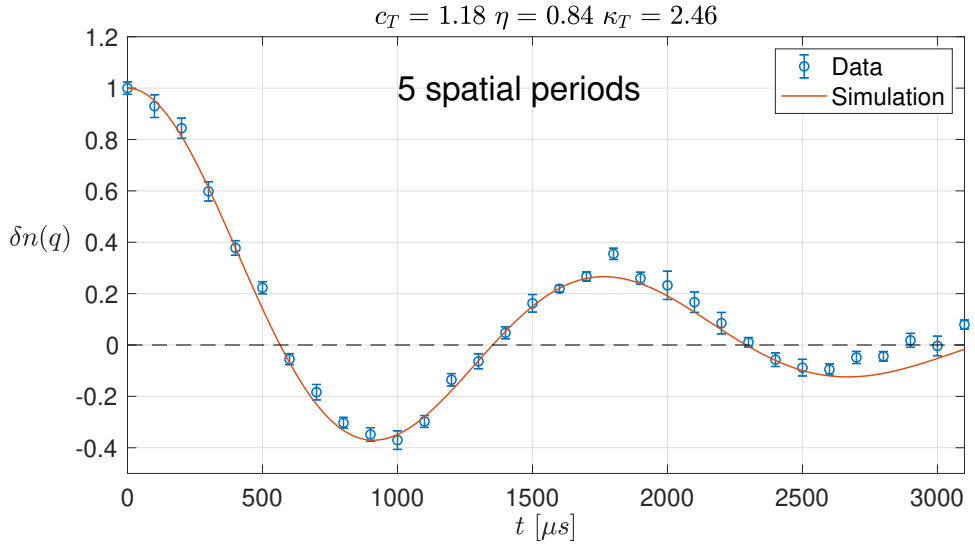


(b) All 5 periods.

Figure 4.7: Evolution of $\delta n(q)$ as function of time, where $T/T_F = 0.28$ and $q = 2\pi/\lambda$, with $\lambda = 23.5\,\mu$m, for the 3 central spatial periods, compared with all 5 spatial periods. Here, $\eta$ is in units of $\hbar\, n_0$ and $\kappa_T$ is in units of $\hbar\, n_0\, k_B/m$. The best fit simulation works for both cases in the first 2.5 ms, and deviates from the 5 periods data after 2.5 ms due to effect of walls. Error bars are statistical (see Sec. 4.3.1).

### 4.2.2 Solving Ordinary Differential Equations

The quest for a faster and better method lead us to think about how to simplify the hydrodynamic linear response equations Eqs. 4.1 and 4.2, which we repeat here

$$\delta\ddot{n} = c_T^2\,\partial_z^2(\delta n+\delta\tilde{T})+\frac{1}{m}\partial_z\cdot[n_0(z)\,\partial_z\delta U+\delta n\,\partial_z U_0]+\frac{4\eta}{3n_0 m}\,\partial_z^2\delta\dot{n} \tag{4.6}$$

$$\delta\dot{\tilde{T}} = \epsilon_{LP}\,\delta\dot{n}+\frac{\kappa_T}{n_0 c_{V1}}\partial_z^2\delta\tilde{T}, \tag{4.7}$$

where $\delta U = 0$ for $t > 0$ in our experiment.

These equations are slow to solve since they are coupled partial differential equations (PDEs) with respect to $t$ and $z$. However we can perform a Fourier transform on these equations to extract information of the dominant frequency component $\delta n(q,t)$.

In practice, we can choose to limit the spatial region for the Fourier transform to the region near the center of the box, where the background density varies very slowly within about 10%. Further, the phase of the transform is selected so that the Fourier amplitudes are real, by choosing an integral number of periods for the length of the transformed region. When the evolution is measured over short enough time scales, the box potential makes a negligible contribution to the time-dependent density profile in the region of interest, so that we can safely ignore it. Therefore, within such range, we can let $\nabla U_0 = 0$.

Actually, a Fourier transform will convert these linear PDEs with constant coefficients to ordinary differential equations (ODEs). For Eqs. 4.6 and 4.7, the z-partial derivatives become $-q^2$ after a Fourier transform, thus greatly simplifies the equations.

As shown in Sec. 2.2.2, applying a spatial Fourier transform on Eqs. 4.6 and 4.7 yields coupled time-dependent equations for the Fourier amplitudes $\delta n(q,t)$ and $\delta\tilde{T}(q,t)$,

$$\delta\ddot{n}(q,t) = -\omega_T^2[\,\delta n(q,t)+\delta\tilde{T}(q,t)\,]-\gamma_\eta(q)\,\delta\dot{n}(q,t) \tag{4.8}$$

$$\delta\dot{\tilde{T}}(q,t) = \epsilon_{LP}\,\delta\dot{n}(q,t)-\gamma_\kappa(q)\,\delta\tilde{T}(q,t). \tag{4.9}$$

with $\epsilon_{LP} = c_{P_1}/c_{V_1} - 1$, and

$$\begin{aligned} \omega_T(q) &= c_T\, q \\ \gamma(q) &= \frac{\hbar}{m} q^2 \\ \gamma_\eta(q) &= \frac{4}{3}\alpha_\eta\, \gamma(q) \\ \gamma_\kappa(q) &= \alpha_\kappa \frac{k_B}{c_{V_1}} \gamma(q), \end{aligned} \tag{4.10}$$

where by definition

$$\eta \equiv \alpha_\eta\, \hbar\, n_0 \tag{4.11}$$

$$\kappa_T \equiv \alpha_\kappa \hbar\, n_0 \frac{k_B}{m}. \tag{4.12}$$

Here, we see that Eqs. 4.8 and 4.9 are now ordinary differential equations with respect to time. It is very easy to solve them numerically with given initial conditions, i.e., $\delta n(q,0) \neq 0$ (measured), $\delta \dot{n}(q,0) = 0$ and $\delta \tilde{T}(q,0) = 0$.

We use a MATLAB ODE 45 solver to solve these second-order equations numerically. Notice that the MATLAB ODE solvers only solve first-order equations. We need to rewrite higher-order ODEs as an equivalent system of first-order equations using the generic substitutions.

We vary $\omega_T$, $\gamma_\eta$ and $\gamma_\kappa$ as fit parameters to run a similar $\chi^2$ search for finding the global minimum. Then the shear viscosity coefficient $\alpha_\eta$, thermal conductivity coefficient $\alpha_\kappa$ can be obtained from Eq. 4.10, and with the isothermal sound speed $c_T = \omega_T/q$, again, the reduced temperature $T/T_F$ can be obtained (see Sec. 2.1.2).

So far, our second data analysis method, solving time-dependant ODE method, has been established. Let us see what we have gained.

The first benefit is that it's much easier to write the code this way. With a well-developed MATLAB solver can be used directly, the code for solving the equations can be written in just 10 lines. Applying the solutions to our search loop for the numerical integration method easily works.

Second, the speed is much faster than the previous method mainly because we eliminate the space dependence. Also, the ODE 45 solver uses an algorithm faster than the "brute force" method for the PDE's. For comparison, we run a same size of search points with the two methods. It takes 525 seconds for the numerical integration method, while only taking

2.5 seconds for the solving ODE method[3].

Solving the ODE for $\delta n(q,t)$ is built on the assumption that $\nabla U_0 = 0$, so it is worth comparing the results of the two methods. We look at some typical cases we measured. For the $T/T_F = 0.28$ case, the extracted $\alpha_\eta$ differ by 9.5% (solving ODE is bigger) and $\alpha_\kappa$ differ by 0.9% (solving ODE is bigger). For the $T/T_F = 0.52$ case, the extracted $\alpha_\eta$ differ by 3.7% (solving ODE is bigger) and $\alpha_\kappa$ differ by 3.0% (solving ODE is bigger).For the $T/T_F = 0.63$ case, the extracted $\alpha_\eta$ differ by 3.0% (solving ODE is bigger) and $\alpha_\kappa$ differ by 2.0% (solving ODE is smaller).

We can see that there is no big difference. Considering the accumulated deviation from the different algorithms for the two methods, the actual difference should be even smaller.

By taking the derivative term of potential $\nabla U_0$ out of the equation, we make the hydrodynamic linear response equations even neater. The direct implementation is that solving by the ODE method speeds up the fitting process significantly. However, there is no change in the physical interpretation. Also, a well-measured initial density profile is still needed.

### 4.2.3 Analytic Fit Function

Let us take another look at our time dependent ordinary differential equations 4.8 and 4.9. Instead of solving them numerically, we can try to find an analytic solution, as shown in Sec. 2.2.2).

The density and reduced temperature perturbation can be written as

$$\delta n(q,t) = A_0\, e^{-\Gamma t} + e^{-a\,t}\,[A_1 \cos(b\ t) + A_2 \sin(b\ t)], \tag{4.13}$$

and

$$\delta \tilde{T}(q,t) = B_0 \left[ e^{-\Gamma t} - e^{-a\,t} \cos(b\ t) + \frac{\Gamma - a}{b}\, e^{-a\,t} \sin(b\ t) \right], \tag{4.14}$$

where the coefficients are connected by

$$\begin{aligned} \Gamma + 2\,a &= \gamma_\eta + \gamma_\kappa \\ a^2 + b^2 + 2\,a\,\Gamma &= c_S^2\, q^2 + \gamma_\eta\, \gamma_\kappa \\ \Gamma(a^2 + b^2) &= c_T^2\, q^2\, \gamma_\kappa. \end{aligned} \tag{4.15}$$

with $\gamma_\eta$, $\gamma_\kappa$ given by Eq.4.10.

[3]The elapsed time is for a single given $c_T$ with a typical data length of 26 different times. The actual time we spend to search for the global minimal is much longer.

Restriction are set by the initial conditions of Eqs. 4.13 and 4.14, as follows. For the density perturbation, the initial condition $\delta n(q,0) = A$ requires $A_1 = A - A_0$, and from $\delta \dot{n}(q,0) = 0$, we can obtain $A_2 = [(\Gamma - a)A_0 + a\,A]/b$. With $\delta \tilde{T}(q,0) = 0$, the third initial condition yields the amplitude $A_0$ should follow

$$[(\Gamma - a)^2 + b^2]A_0 = (a^2 + b^2 - c_T^2 q^2)A. \tag{4.16}$$

Similarly, the temperature perturbation satisfies $\delta \tilde{T}(q,0) = 0$ and $\delta \dot{\tilde{T}}(q,0) = 0$. From Eq. 4.9, we have the additional constraint

$$(\Gamma - a)^2 + b^2]B_0 = -\epsilon_{LP}\, c_T^2 q^2\, A. \tag{4.17}$$

Here, we have developed an analytic solution for the evolution of $\delta n(q,t)$, connecting all the coefficients and the physical properties. We see that the solution consists of two independent modes, i.e., thermal diffusion and first sound.

Actually, the analytic solution method unravels the physics of why we can measure the shear viscosity and the thermal conductivity independently. The thermal diffusion mode, described by an exponential decay rate $\Gamma$, determines the thermal conductivity, which is proportional to the temperature relaxation rate.

On the other hand, the first sound mode is described by an oscillating exponential decay. The oscillation frequency gives the first sound speed, which determines the reduced temperature from the equation of state. The decay rate $2a$ gives the usual first sound diffusivity $D_1 = 2a/q^2 \simeq D_\eta + D_\kappa$, which contains contributions only from the shear viscosity and the thermal conductivity (see Eq. 2.66). So the shear viscosity can be extracted from subtracting $D_\kappa$ from $D_1$.

Hereby, the decay rates of these two distinct modes determine both the thermal conductivity and the shear viscosity. The contributions of the two modes to $\delta n(q,t)$ are illustrated by an example of our fit for the $T/T_F = 0.46$ data in Fig. 4.8. The contributions to $\delta \tilde{T}(q,t)$ is also shown in Fig. 2.3 in chapter 2.

With enough interpretation of the analytic solutions, let us now move forward to discuss how to use this method practically.

The straight-forward way is to do a 4-parameter fit to the $\delta n(q,t)$ equation: Eq. 4.13. Three of the parameters are $\Gamma, a, b$, relate to the three frequencies $c_T q, \gamma_\eta, \gamma_\kappa$ we want to find from Eq. 4.15. The other parameter is the amplitude $A$, which also gives $A_0$ by Eq. 4.16. To get the best fit, we construct a $\chi^2(q,t)$ , similar to the previous two methods, and use a

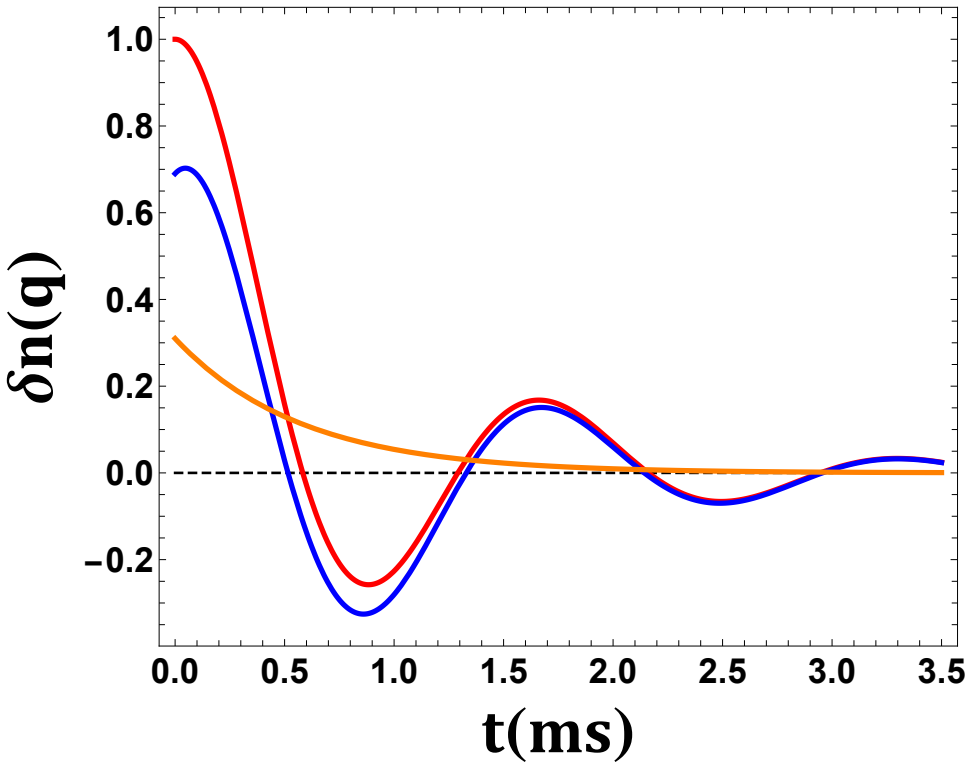


Figure 4.8: Components of the analytic fit function $\delta n(q,t)$ Eq. 4.13 for a typical data in the middle temperature range of our measurements, where $T/T_F = 0.46$ and $q = 2\pi/\lambda$, with $\lambda = 22.7\,\mu$m. Red curve: Total fit function; Orange curve: Zero frequency, exponentially decaying (thermal diffusion) mode; Blue curve: oscillating, exponentially decaying first sound mode.

"fminsearh" MATLAB function to return us the corresponding fit parameter for the global minimum[4]. One can use other algorithms for the same purpose.

Then solving Eq. 4.15 numerically and using Eq. 4.10 gives us the shear viscosity $\eta$ and the thermal conductivity $\kappa_T$ and the isothermal sound speed $c_T$, which we use to get the reduced temperature $T/T_F$ since $T/T_F$ is a known function of $c_T$ (Sec.2.1.2).

For the sound diffusivity $D_1$, although we could calculate it from Eq. 2.66 with known $\eta, \kappa_T$, the more straight-forward way is to get $D_1$ directly form the fit parameters $a$. Note that by definition, the measured sound diffusivity $D_1 = 2\,a/q^2$ [Landau and Lifshitz 1959] (a detailed discuss about the measured sound diffusivity is shown in Sec. 2.2.3).

There are also alternative ways to use the analytic function. Actually, even though we know the restriction on $A_0$, which is given by Eq. 4.16, we can construct a 5-parameter fit ,

[4] "fminsearch" is programmed to find real local minimum of unconstrained multi-variable function using derivative-free method. In our case, the local minimal is the global minimal, so no additional search is needed.

with both $A$ and $A_0$ as fit parameters. This method fits our data reasonably well, especially for good data, yielding a $A_0/A$ almost same as Eq. 4.16. It shows the analytic fit method has potential for future applications on more complicated systems, in which more fit parameters are needed[5].

Also, although our fit function works well when $A$ is set to be a fit parameter, notice that the initial condition requires $\delta n(q,0) = A$, where $\delta n(q,0)$ can be measured. So we can force $A$ to be our measured $\delta n(q,0)$, then the fit becomes a 3-parameter fit. One should find that doing so immediately makes the analytic fit function method equivalent to the solving $\delta n(q,t)$ ODE method[6].

Here, we can see one beauty of the analytic fit function method is that it does not require a very well-measured initial density profile. A perfectly measured profile, on the other hand, could slightly increase the sensitivity to other fit parameters.

The speed of this method is the fastest among all our methods. It takes less than 1 second for both the 4-parameter fit and the 5-parameter fit, for our largest data set including 32 different times. In practice, it's about 5000 times faster than the numerical integration method (the slowest), and it is easy to program.

The analytic fit function reveals physically why we can distinguish the shear viscosity and the thermal conductivity in the evolution of the atomic density profile, i.e., the two independent modes of thermal diffusion and first sound, which evolve differently. However, we can still improve it for practical purpose.

### 4.2.4 Exact Analytic Fit Function

Followed by the previous subsection, while the fit parameter $A$ is just an amplitude, the useful fit parameters directly from the analytic fit function are $a$, $b$ and $\Gamma$. Then we need to use Eq. 4.15 to solve for $\gamma_\kappa, \gamma_\eta$ and $c_T$. Actually we can use the latter three directly as fit parameters to avoid accumulated solver inaccuracies in the numerical solving process for Eq. 4.15.

We write down an analytic fit function in terms of the two decay rates $\gamma_\kappa, \gamma_\eta$ and the oscillation frequency $\omega_T$. We rewrite Eq. 4.15 in frequencies $\omega_S \equiv q\, c_S$, $\omega_T \equiv q\, c_T$ for

[5]It is important to mention that we should not use the 5-parameter fit in practice, since there are too many free parameters for getting a reliable result. However, seeing a good agreement between the 5-parameter fit and the 4 or 3 parameters fit for some well measured data shows a promising potential for applying the method to more complicated systems, e.g., where the equation of state is unknown.

[6]Actually the two methods still differ in terms of chosen fit parameters. Changing the fit parameters from $(a, b, \Gamma)$ to $(c_T, \gamma_\eta, \gamma_\kappa)$ lead to the so-called "exact analytic fit function", which we will discuss shortly.

convenience

$$\begin{aligned} \Gamma + 2\,a &= \gamma_\kappa + \gamma_\eta \\ a^2 + b^2 + 2\,a\,\Gamma &= \omega_S^2 + \gamma_\eta\,\gamma_\kappa \\ \Gamma(\,a^2 + b^2) &= \omega_T^2\,\gamma_\kappa, \end{aligned} \tag{4.18}$$

where $\omega_S^2 = (1+\epsilon_{LP})\,\omega_T^2 = c_{P_1}/c_{V_1}\,\omega_T^2$, $\epsilon_{LP} \equiv c_{P_1}/c_{V_1} - 1$, $\gamma_\eta = (4\hbar q^2/3m)\,\alpha_\eta$, $\gamma_\kappa = (k_B\hbar q^2/c_{V_1}\,m)\,\alpha_\kappa$ (see chapter 2 for complete derivations).

The decay rate $\Gamma$ is obtain by finding the real solution to the cubic polynomial

$$s^3 - s^2(\gamma_\kappa + \gamma_\eta) + s\,(\omega_S^2 + \gamma_\kappa\gamma_\eta) - \omega_T^2\gamma_\kappa = 0. \tag{4.19}$$

Solving for $a$ and $b$, we have

$$\begin{aligned} a &= \frac{1}{2}(\gamma_\kappa + \gamma_\eta - \Gamma) \\ b &= \sqrt{\omega_S^2 + (\Gamma - \gamma_\kappa)(\Gamma - \gamma_\eta) - \frac{1}{4}(\gamma_\kappa + \gamma_\eta - \Gamma)^2}. \end{aligned} \tag{4.20}$$

Also, from the initial conditions, we have

$$\begin{aligned} A_0 &= \frac{a^2 + b^2 - \omega_T^2}{(\Gamma - a)^2 + b^2}\,A \\ A_1 &= A - A_0 \\ A_2 &= [(\Gamma - a)A_0 + a\,A]/b. \end{aligned} \tag{4.21}$$

Now, with Eqs. 4.20 and 4.21, we can fit the analytic function, repeating here:

$$\delta\,n(q,t) = A_0\,e^{-\Gamma t} + e^{-a\,t}\,[A_1\cos(b\,t) + A_2\,\sin(b\,t)] \tag{4.22}$$

using the three frequencies $\omega_T, \gamma_\kappa, \gamma_\eta$, and the amplitude $A$ as free parameters.

We define this method as the "exact analytic fit function", since it uses exactly what we want to extract as fit parameters. We use this method for obtaining the final results we published in our paper [Wang et al. 2022].

To practice, we first perform fast Fourier transfers (FFTs) on our 1-D density profiles at each time during the evolution, which gives us both $\delta\,n(q,t_i)$ and $\sigma_{\delta\,n(q,t_i)}$. The $q$ value is found by performing a MATLAB "findpeak" search on the Fourier spectrum for each of the

first five $t$, and then doing an average. We define the $\chi^2$ function as

$$\chi^2 = \sum_{t_i} \frac{(\delta n(q,t_i) - \delta n_{Pred}(q,t_i))^2}{\sigma^2_{\delta n(q,t_i)}}, \tag{4.23}$$

where $\delta n(q,t_i)$ and $\sigma_{\delta n(q,t_i)}$ are measured, $t_i$ is the range of times we want to sum over, which is nominally for all the data we take. However, there are cases we choose to omit some data points, which show large deviations.

To compute the above $\chi^2$, we need to know $\delta n_{Pred}(q,t_i)$, which is obtained from the "exact analytic fit function" with given $\omega_T$, $\gamma_\kappa$, $\gamma_\eta$, $A$, $\omega_S$, $\Gamma$ (see Appendix).

Here, we define $\omega_T, \gamma_\kappa, \gamma_\eta$ and $A$ as free fit parameters. $\Gamma$ can be obtained by solving the cubic polynomial Eq. 4.19. $\omega_S$ is related to $\omega_T$ by $\omega_S^2 = c_{P_1}/c_{V_1}\,\omega_T^2$, with

$$\frac{c_{P_1}}{c_{V_1}} = \frac{f_E(\theta)}{f_E(\theta) - \frac{2}{5}\theta\, f_E'(\theta)}. \tag{4.24}$$

We also have

$$c_T^2 = \frac{\omega_T^2}{q^2} = \frac{v_F^2}{3}\left[f_E(\theta) - \frac{2}{5}\,\theta\, f_E'(\theta)\right]. \tag{4.25}$$

where $f_E(\theta)$ is measured precisely by Ku et al. [2012]. From Eqs. 4.24 and 4.25, we can solve for $c_{P_1}/c_{V_1}$ with given $q$, $v_F$ as constants, and thus obtain $\omega_S$. In practice, we fit $c_P(\theta)/c_V(\theta)$ and $\theta(c_T/v_F)$ with polynomial to speed up fit process (see Sec. 2.1.2).

Finally, by providing an initial guess of the free fit parameters, we use the MATLAB "fminsearch" function to find the global minimum of the constructed $\chi^2$, yielding the best fit parameters.

Examples of our fit for different temperatures are shown below, Fig. 4.9 $\sim$ Fig. 4.14. In these figures, blue dots are measured data with errorbars. Red curves are best fits from this "exact analytic fit function" method. For the evolution, note that the decay rate $\Gamma \propto q^2 \propto \lambda^{-2}$. In order to give the reader a better view of the different decay rates versus the reduced temperatures $T/T_F$, we keep the same wavelength $\lambda$ for all these 6 figures here.

We also compare the data measured at different wavelengths (see Figs. 4.15 and 4.16) to check whether we get consistent results. We do not see significant change in the extracted transport coefficients for neither longer nor shorter wavelengths. A more detailed discussion will be covered in Chapter 5.

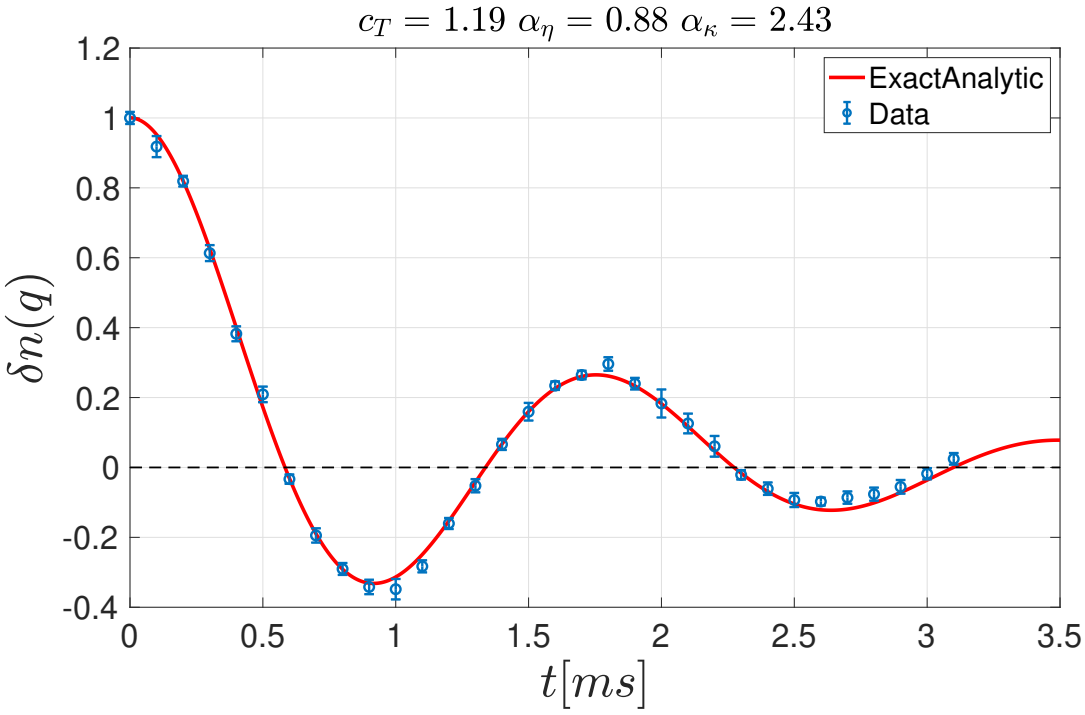


Figure 4.9: $T/T_F = 0.28$, $\lambda = 23.5\mu m$.

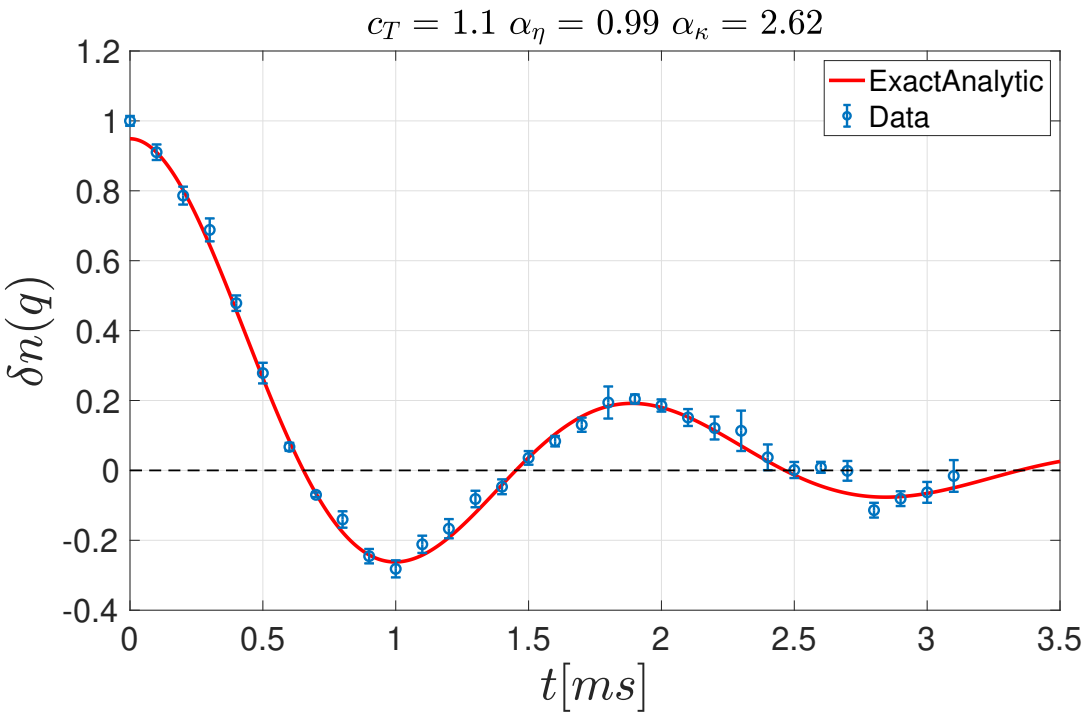


Figure 4.10: $T/T_F = 0.34$, $\lambda = 23.5\mu m$.

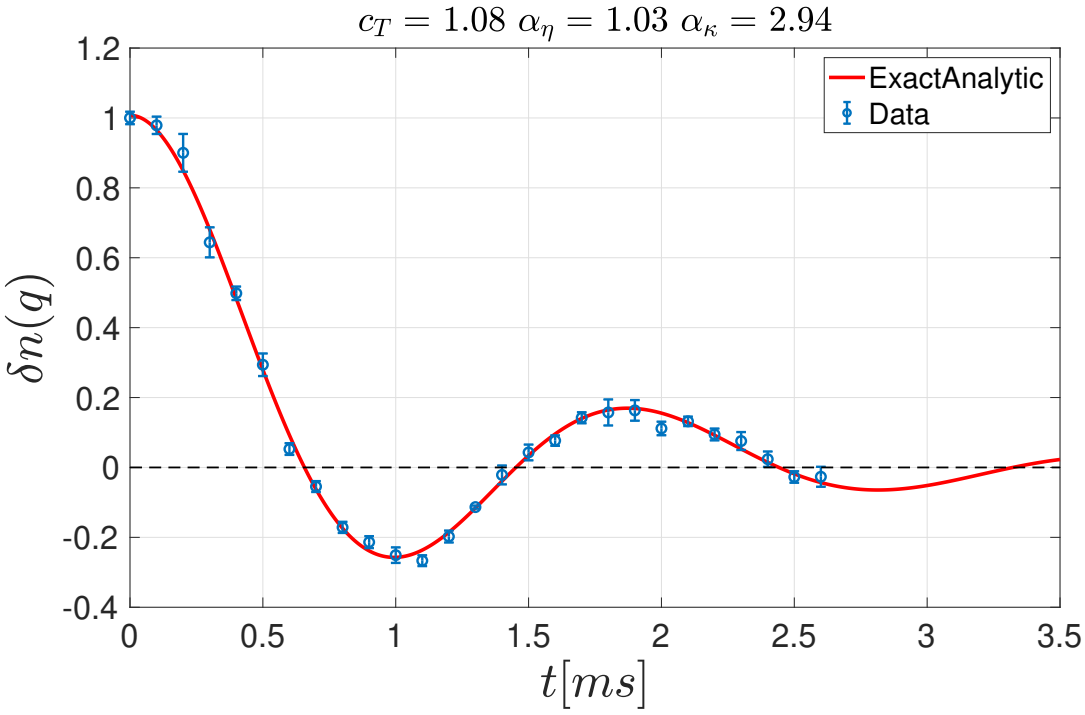


Figure 4.11: $T/T_F = 0.40$, $\lambda = 23.0\mu m$.

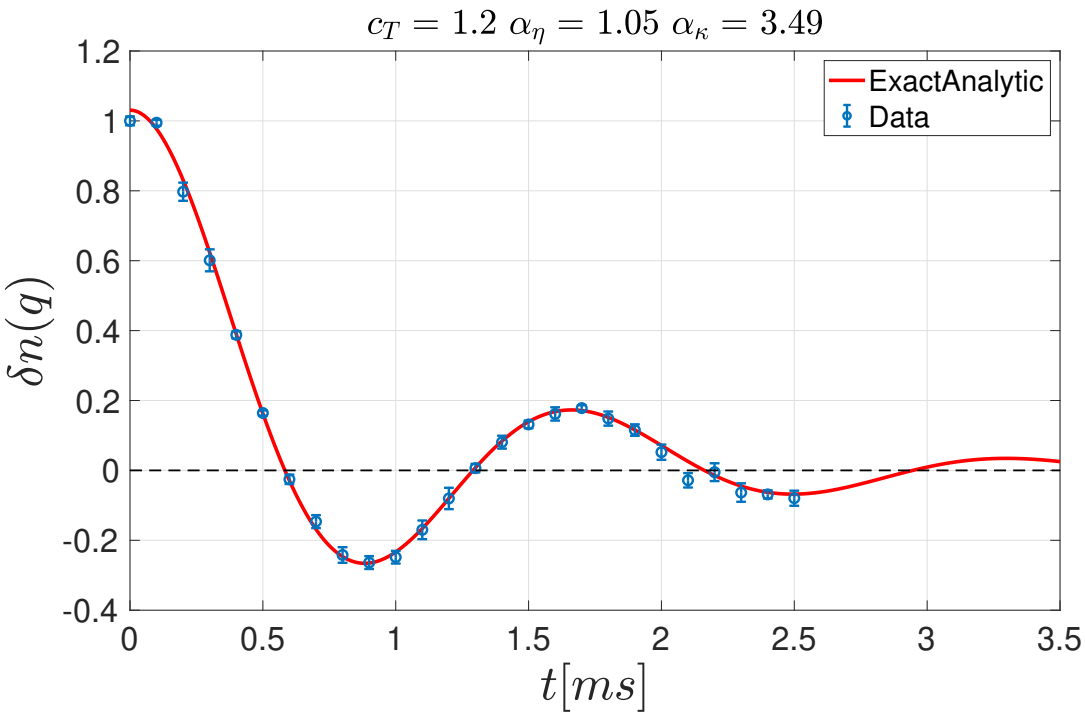


Figure 4.12: $T/T_F = 0.46$, $\lambda = 22.7\mu m$.

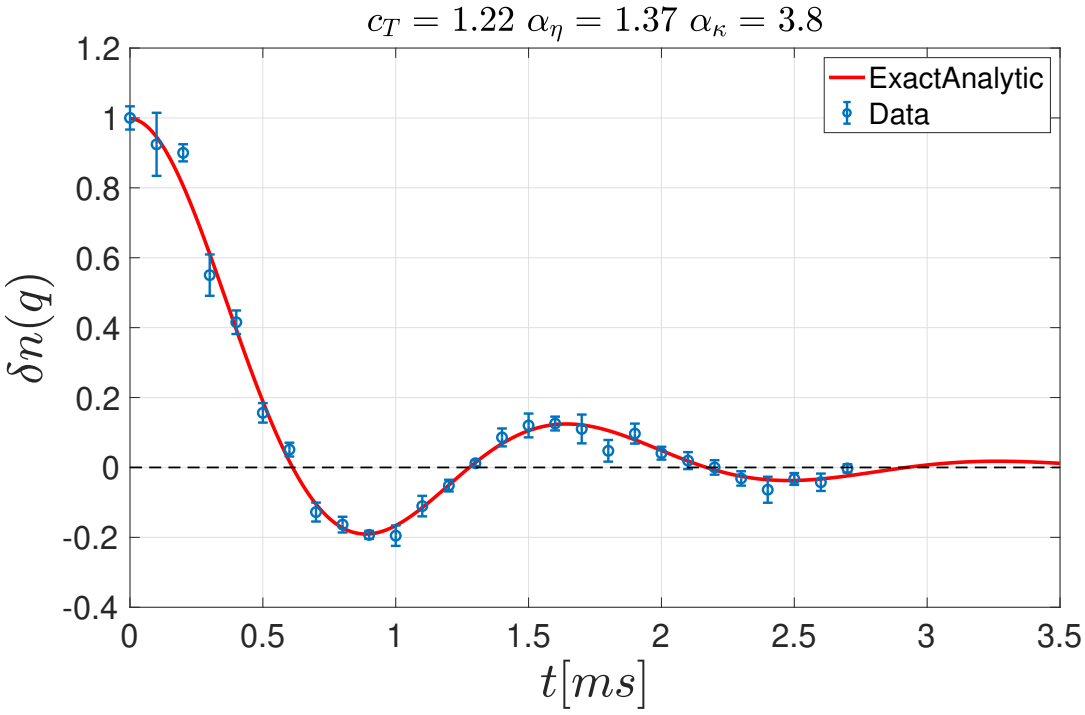


Figure 4.13: $T/T_F = 0.52$, $\lambda = 23.0\mu m$.

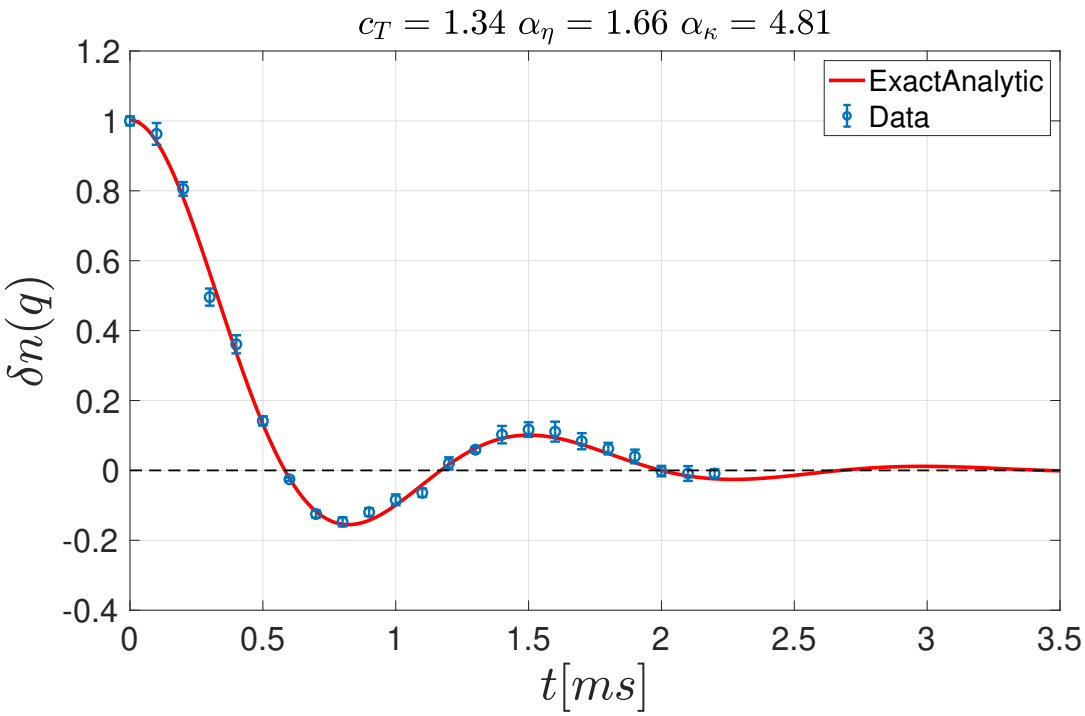


Figure 4.14: $T/T_F = 0.63$, $\lambda = 23.3\mu m$.

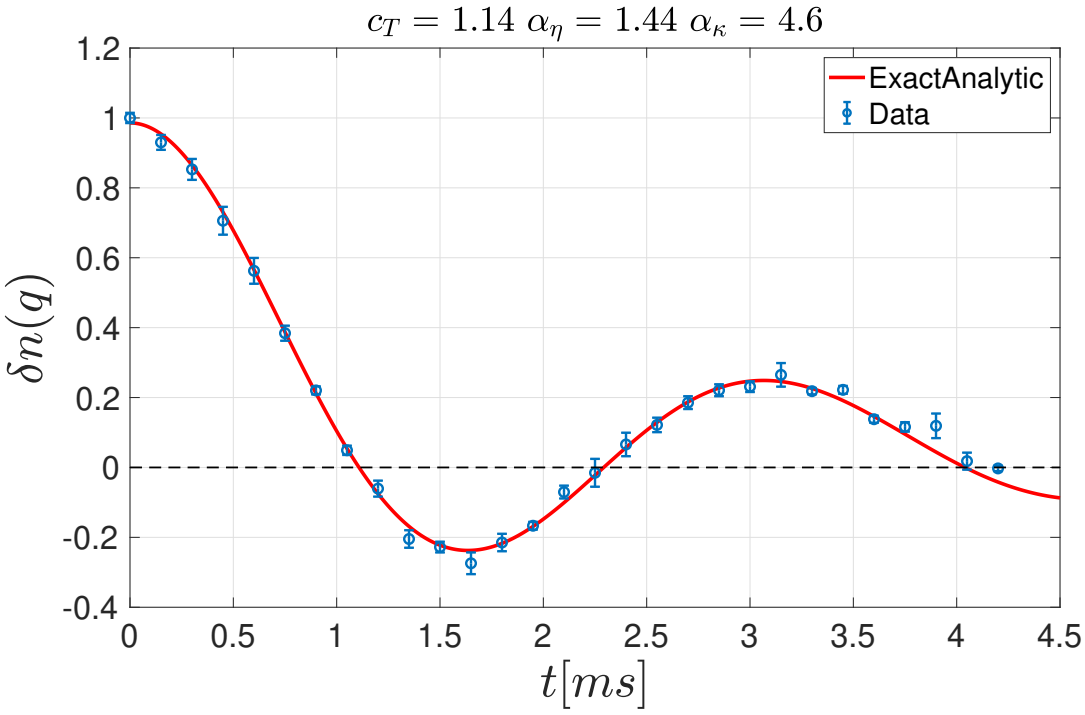


Figure 4.15: $T/T_F = 0.56$, with longer wavelength $\lambda = 41.7\mu m$.

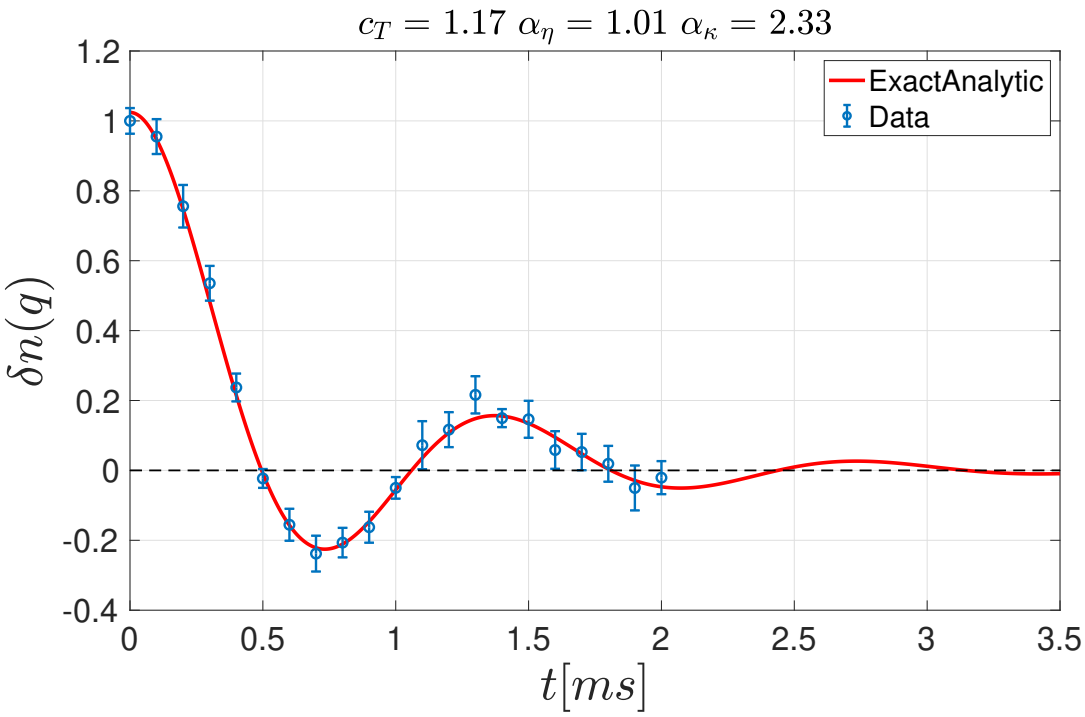


Figure 4.16: $T/T_F = 0.37$, with shorter wavelength $\lambda = 18.2\mu m$.

## 4.3 Data Analysis Details

In this section, we discuss some data analysis details, including the calculation of statistical errors, the determination of the central density, and the estimation of the systematic shifts in our experiments.

### 4.3.1 Statistical Uncertainty

Our statistical uncertainty in the experiment comes from the shot-to-shot variation of the density profile. At the beginning of each measurement cycle, the number of atoms loaded into the box varies. Also, even assuming that the atom number is the same for all runs, the spatial distribution can vary as well.

All the properties we measure depend on the density of the atomic gas. In a single experiment, we usually take about 150-200 shots and assume they all represent the same system, i.e., same density and temperature etc. So we need to ensure that the atom number fluctuation is not too big for the data we study. Actually, the first step of our data analysis is to calculate the standard deviation $\sigma_s$ in atom number of our entire data set, and to exclude those data $2\sigma_s$ away from the mean. This step helps us select the data for the same condition statistically.

We use a standard statistical measure $\sigma_m = \frac{1}{\sqrt{N}}\sigma_s$, i.e., the standard error of the mean (SEM), to estimate the variations. Here, $\sigma_s$ is the corrected sample standard deviation[7], given by

$$\sigma_s = \sqrt{\frac{1}{N-1}\sum_{i=1}^{N}(x_i-\mu)^2}, \tag{4.26}$$

where $\mu = \frac{1}{N}\sum_{i=1}^{N} x_i$, and $x_i$ are measurements of the sample. We omit the notation $_m$ and use the usual symbol for standard deviation $\sigma$ to denote SEM in the rest of this thesis for convenience. Since we are mainly interested in the density perturbation in the Fourier domain, SEM here is expressed by $\sigma_{\delta n(q,t)}$.

In our plots for $\delta n(q,t)$, the statistical variation is shown as error bars, each denoting for $\pm 1\sigma$. As we mentioned in Sec. 4.1, since we take a large number of backgrounds, $\sigma_{n_0(z,t)}$ can be neglected and $\sigma_{\delta n(z,t)} \simeq \sigma_{n(z,t)}$.

The hydrodynamic transport coefficients extracted by the fit parameters are examined by an error matrix for goodness of fit [Taylor 1997]. Suppose $\chi^2$ depends on two independent

[7]Note that the corrected sample standard deviation is still biased downward for small sample size, but it performs better than the uncorrected one; Either method is good enough for our application.

parameters $(u, v)$, and we find the minimum at $(u_0, v_0)$. To evaluate the uncertainty for the minimum, we expand $\chi^2$ by a Taylor expansion up to second order:

$$\chi^2(u,v) \simeq \chi^2(u_0,v_0) + \sum_{i=u,v} D_i \epsilon_i + \frac{1}{2} \sum_{i,j=u,v} H_{ij} \epsilon_i \epsilon_j, \tag{4.27}$$

where $\epsilon$ is a small step walking away from $(u_0, v_0)$ to $(u, v)$, i.e., $u = u_0 + \epsilon_u$ and $v = v_0 + \epsilon_v$. $D_i$ is the partial derivative with respect to each parameter, and $H_{ij}$ is the Hessian matrix, defining as follows,

$$\begin{aligned} D_u &= \frac{\partial \chi^2}{\partial u} \\ D_v &= \frac{\partial \chi^2}{\partial v} \\ H_{uu} &= \frac{\partial^2 \chi^2}{\partial u^2} \\ H_{vv} &= \frac{\partial^2 \chi^2}{\partial v^2} \\ H_{uv} = H_{vu} &= \frac{\partial^2 \chi^2}{\partial u \partial v}. \end{aligned} \tag{4.28}$$

The minimum of $\chi^2$ requires $D_i = 0$. The uncertainty in the coefficients $(u, v)$ is evaluated by a change of 1 of the $\chi^2$ with respect to a change of the coefficients. Taking the correlation between $u$ and $v$ into account, the corresponding uncertainty is given by the square root of the error matrix, where a factor of $\sqrt{2}$ comes from the Taylor expansion in Eq. 4.27. So, we have

$$\begin{aligned} \sigma_u &= \sqrt{\frac{2 H_{vv}}{H_{uu} H_{vv} - {H_{uv}}^2}} \\ \sigma_v &= \sqrt{\frac{2 H_{uu}}{H_{uu} H_{vv} - {H_{uv}}^2}}. \end{aligned} \tag{4.29}$$

Use this method, we calculate our uncertainties in the extracted hydrodynamic transport coefficients. For the shear viscosity coefficient $\alpha_\eta$ and the thermal conductivity coefficient $\alpha_\kappa$, we evaluate $\chi^2(\alpha_\eta, \alpha_\kappa)$ holding $\omega_T$ and $A$ as constants for the "exact analytic fit function" method (4.2.4), and find $\sigma_{\alpha_\eta}$ and $\sigma_{\alpha_\kappa}$ from Eqs. 4.28 and 4.29, by letting $u \equiv \alpha_\eta$ and $v \equiv \alpha_\kappa$.

For the sound diffusitivity $2a/q^2$, we evaluate $\chi^2(a, b)$ holding $\Gamma$ and $A$ as constants for the analytic fit function method (4.2.3), and find $\sigma_a$ from Eqs. 4.28 and 4.29, by letting $u \equiv a$ and $v \equiv b$. Then we calculate $\sigma_{D_1} = 2\sigma_a/q^2$.

### 4.3.2 Determination of the Central Density

The central 3D-density $n_0$ is used to find the central Fermi energy, corresponding Fermi temperature $T_F$, and Fermi speed $v_F$, which determines the reduced temperature $T/T_F$ from the measured sound speed $c_T$ using the known equation of state [Ku et al. 2012]. The reduced temperature then determines the thermodynamic properties of the sample.

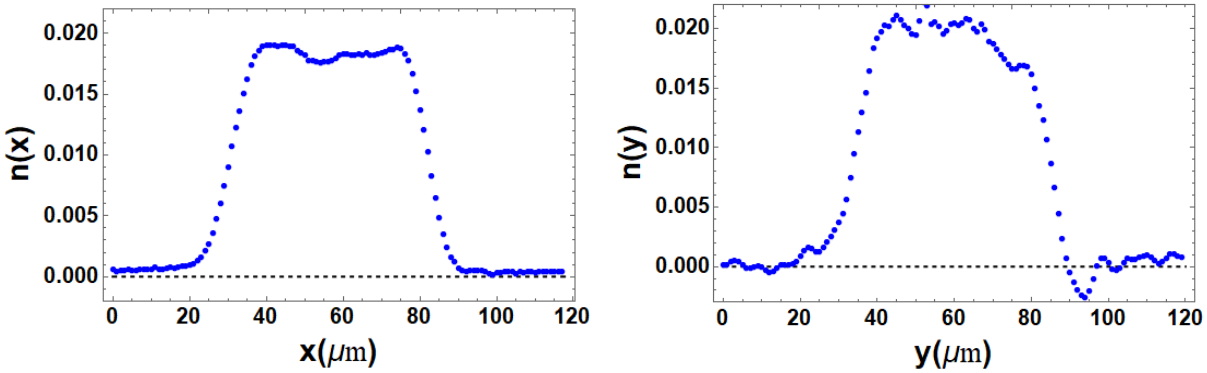


(a) $x$ profile from the horizontal camera.

(b) $y$ profile from the vertical camera.

Figure 4.17: Density profiles along the $x$ and $y$ directions of the box potential. The horizontal imaging path is cleaner than the vertical imaging path, where an artificial distortion can be seen.

To find $n_0$, we observe the trapped cloud along the $x$ and $y$ axes with two cameras (see Fig. 4.17). In this way, we measure the two-dimensional column densities $\tilde{n}(z,x) = \int_{-\infty}^{\infty} dy\, n(x,y,z)$ and $\tilde{n}(z,y) = \int_{-\infty}^{\infty} dx\, n(x,y,z)$, for each spin state, where $z$ denotes the long axis of the box potential and $x$ denotes the direction of the bias magnetic field. For our experiments, the typical box dimensions are $\Delta x = 52\,\mu$m, $\Delta y = 50\,\mu$m and $\Delta z = 150\,\mu$m.

The curvature of the bias magnetic field produces a harmonic confining potential $\propto z^2$, which causes a noticeable variation of the density over $150\,\mu$m. In contrast, the confining potential $\propto y^2$ produces a much smaller variation of the density over $50\,\mu$m along the $y$ axis. Further, the number of atoms trapped outside the box along $x$ and $y$ is negligible (see Sec. 3.3.4). We note that the measured $n(y)$ is distorted in Fig. 4.17 (b). This is an artifact of the imaging path for the vertical camera, which is collinear with the vertically projected beams that form the sides of the box potential. We assume that the true shapes are nearly identical.

The one-dimensional density that we analyze in the experiments as a function of time, is obtained by integrating the measured 2D-column density over a limited central region along $x$ (about 43.5 microns long), where the density is slowly varying,

$$n(z) = \int_{x_1}^{x_2} d\,x\,\tilde{n}(z,x). \tag{4.30}$$

The $n(z)$ contains most of the atoms (usually more than 80%) along $x$, while the edges are avoided.

To estimate the 3D density, we assume that $n(x,y,z)$ approximately factors, as it would in a true 3D box potential,

$$n(x,y,z) \simeq \tilde{n}(x,z)\,n(y). \tag{4.31}$$

We normalize $\int_{-\infty}^{\infty} d\,y\,n(y) = 1$, so that $\int_{-\infty}^{\infty} d\,y\,n(x,y,z) = \tilde{n}(x,z)$ as it should. The normalized 1D density $n(y)$, averaged over the "top-hat" region near the center of the box $y = y_c$, is essentially the inverse of the box length $L_y$ along $y$, i.e., $n(y) = 1/L_y$, as it would for a true box potential. We measure

$$n(y) = \frac{\int_{z_1}^{z_2} d\,z\,\tilde{n}(z,y)}{\int_{-\infty}^{\infty} d\,y \int_{z_1}^{z_2} d\,z\,\tilde{n}(z,y)}, \tag{4.32}$$

where $\tilde{n}(z,y)$ is the column density measured by the camera oriented along the $x$-axis. $n(y)$ satisfies $\int_{-\infty}^{\infty} d\,y\,n(y) = 1$ for any choice of $z_1$ and $z_2$. We take $z_1$ and $z_2$ in the central region of the cloud (about 35 micron long), where the density is nearly uniform, to measure the Fourier transform $\delta n(q,t)$.

Averaging the column density near the center, $x_c, z_c$, where the 2D density is nearly uniform, we obtain the total central density $n_0 = 2\,\tilde{n}(x_c,z_c)\,n(y_c)$. For a single spin state, typical values are $n(y_c) = 0.0204/\mu\text{m} = 204/\text{cm}$, i.e., $L_y = 49.0\,\mu\text{m}$, and $\tilde{n}(x_c,z_c) = 1.10 \times 10^9/\text{cm}^2$, which yields $n_0/2 = 2.24 \times 10^{11}/\text{cm}^3$. From $n_0$ we find the Fermi speed $v_F$. This in turn determines the reduced temperature $\theta(c_T/v_F)$, where $c_T = \omega_T/q$ is determined from the fit to $\delta n(q,t)$.

Note that there is a systematic effect that could make our measured density slightly lower than the actual density. For any absorption imaging technique, true atom number is measured when the imaging beam is right on the atomic resonance frequency. But every laser beam has a finite bandwidth and the imaging frequency drifts around the resonance in real life, which results in a overall downward shift of the measured average atom number.

A detailed discussion can be find in the thesis of our former group member [Joseph 2010].

However, we don't expect a significant downward shift of the measured density we obtain compared to an estimate of ∼12% from Joseph [2010]. First, our high field magnet power supply has been upgraded to a very stable one, eliminating the variation in B-field and hence imaging resonance frequency, which plays a significant role in Joseph's model. More importantly, as mentioned in the previous subsection, we exclude data $2\sigma_s$ away from the mean atom number. So, our shifts should be significantly smaller than what has been estimated by Joseph [2010].

CHAPTER

# 5

# RESULTS

In this chapter, I will show the main experimental results, i.e., our measured shear viscosity $\eta$, thermal conductivity $\kappa_T$, and sound diffusivity $D_1$. I will also discuss some details of the results to check consistency and generality in our model, and to provide corrections to the measurements based on our best understanding. I also compare our sound diffusivity results with a recent measurement by the MIT group [Patel et al. 2020]. Further, I extend our analysis beyond the current model to the region where hydrodynamics breaks down, to motivate future studies.

## 5.1 Experimental Results

In the previous chapter, I described four data analysis methods. They give identical results for the extracted transport coefficients within errorbars[1]. Here, I show the measurements of the shear viscosity $\eta$, the thermal conductivity $\kappa_T$, and the sound diffusivity $D_1$ from the

[1]The method of numerical integration of $\delta n(z,t)$ (Sec.4.2.1) gives slightly different (a few percent) results compared to the other three methods, which are based on Fourier component $\delta n(q,t)$. This is simply because the density profile is slowly varying in the region we measure, even though we have already chosen the most uniform region. A perfectly uniform potential is expected to make results from all methods identical.

"exact analytic fit function" method (see Sec. 4.2.4).

I briefly summarize this method here to show how we get the shear viscosity $\eta$, the thermal conductivity $\kappa_T$ and the sound diffusivity $D_1$, while readers are encouraged to read chapter 4 for details.

In chapter 1, we have pointed out that the transport coefficients in unitary Fermi gases are universal functions of density and pressure. Here, we define

$$\eta \equiv \alpha_\eta \hbar\, n_0 \tag{5.1}$$

$$\kappa_T \equiv \alpha_\kappa \hbar\, n_0 \frac{k_B}{m}. \tag{5.2}$$

We fit the analytic solution for a density perturbation in Fourier space to the data,

$$\delta n(q,t) = A_0\, e^{-\Gamma t} + e^{-a\,t}\,[A_1 \cos(b\,t) + A_2 \sin(b\,t)], \tag{5.3}$$

using the amplitude $A$ and three frequencies $\omega_T \equiv q\, c_T, \gamma_\kappa, \gamma_\eta$ as free parameters. These three frequencies are connected to the above equation by

$$\Gamma + 2\,a = \gamma_\kappa + \gamma_\eta \tag{5.4}$$

$$a^2 + b^2 + 2\,a\,\Gamma = \omega_S^2 + \gamma_\eta\,\gamma_\kappa \tag{5.5}$$

$$\Gamma(a^2 + b^2) = \omega_T^2\,\gamma_\kappa, \tag{5.6}$$

where $\omega_S^2 = c_{P_1}/c_{V_1}\,\omega_T^2$, $\gamma_\eta = (4\hbar q^2/3m)\alpha_\eta$, $\gamma_\kappa = (k_B\hbar q^2/c_{V_1} m)\alpha_\kappa$. The initial conditions require $A_0 = (a^2 + b^2 - \omega_T^2/(\Gamma - a)^2 + b^2)A$, $A_1 = A - A_0$, $A_2 = [(\Gamma - a)A_0 + a\,A]/b$.

The decay rate $\Gamma$ is obtained by finding the real solution to the cubic polynomial

$$s^3 - s^2(\gamma_\kappa + \gamma_\eta) + s\,(\omega_S^2 + \gamma_\kappa\gamma_\eta) - \omega_T^2\gamma_\kappa = 0. \tag{5.7}$$

Here, the heat capacities per particle at constant volume $c_{V_1}$ and at constant pressure $c_{P_1}$ can be determined from the measured equation of state as function of the reduced temperature $T/T_F = \theta(c_T/v_F)$, which is self-consistently determined from $c_T \equiv \omega_T/q$ by the equation of state, with $v_F$ given for the average central density $n_0$ (see Sec.2.1.2). The fits determine the frequency $\omega_T$ within 2%, enabling in-situ thermometry.

A typical fit to our data is shown in Fig. 5.1. We can see our model describes the evolution of $\delta n(q,t)$ very well. The inset shows two independent modes, an exponentially decaying thermal diffusion mode (orange) and a decaying oscillatory first sound mode (blue).

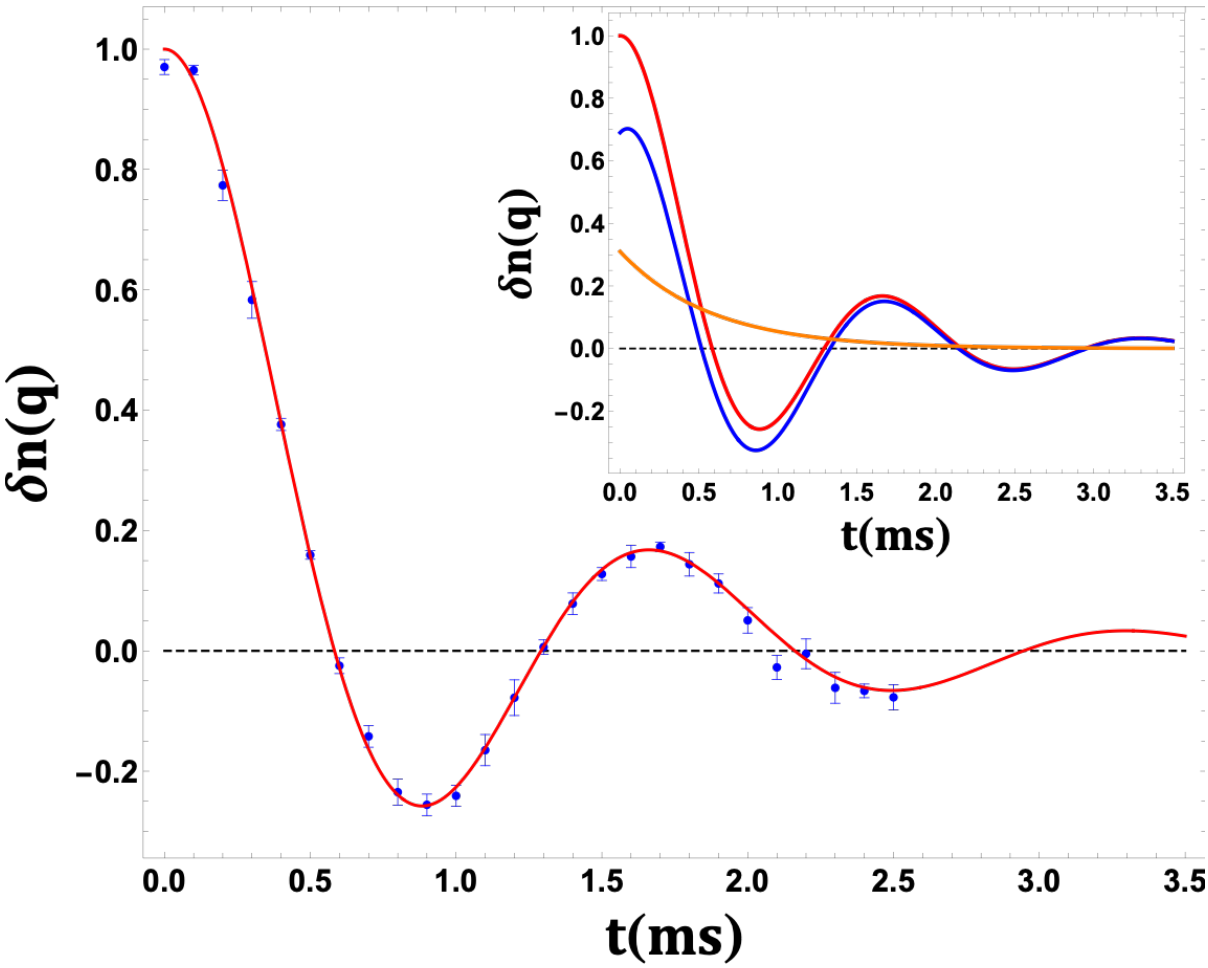


Figure 5.1: Real part of the Fourier transform of the density perturbation $\delta n(q,t)$ for $q = 2\pi/\lambda$ with $\lambda = 22.7\,\mu$m. The reduced temperature $T/T_F = 0.46$. Blue dots (data); Red curve: Analytic fit of our hydrodynamics model. Inset shows contributions of thermal diffusion (orange exponential) and first sound (blue). The error bars are the standard deviation of the mean of $\delta n(q,t)$ (see Sec. 4.3.1).

We find that fitting the data with $A_0 = 0$ increases the $\chi^2$ per degree of freedom from $\simeq 1$ to $\simeq 20$, demonstrating the importance of the thermal diffusion mode, which determines the thermal conductivity in our measurements. In fact, for the isothermal static initial conditions employed in our experiments, the thermally diffusive mode comprises $\simeq 32\%$ of the initial total amplitude of the dominant Fourier component $\delta n(q,0)$, which is readily apparent in the free hydrodynamic relaxation.

Also, from the inset in Fig. 5.1, we can see that these two modes (orange and blue) evolve very differently as functions of time, enabling well-distinguished determination of

$\eta$ and $\kappa$. To be more specific, $\kappa_T$ is, to a very good approximation (see Sec. 2.2.3), found from the decay rate $\Gamma$ of the thermal diffusion mode. Meanwhile, the first sound diffusivity $D_1 = 2a/q^2 = D_\eta + D_\kappa$ contains contributions from $\eta$ and $\kappa_T$. Hereby, subtracting $D_\kappa$ from $D_1$ immediately yields $D_\eta$, which gives $\eta$ (see Eq. 2.66).

Our measured shear viscosity, Fig. 5.2, can be compared to the high temperature diluteness expansion of Bluhm et al. [2017], $\eta_{\rm exp}(\theta) = (\alpha_0\,\theta^{3/2} + \alpha_2)\,\hbar n$, where $\alpha_0 = 2.77(21)$ and $\alpha_2 = 0.25(08)$ are measured by using a second order hydrodynamics model to fit aspect ratio data for freely expanding clouds of Joseph et al. [2015]. Here, the first term is the high temperature limit, where $\theta^{3/2} n \propto T^{3/2}$ depends only on the temperature. The extracted $\alpha_0$ is in excellent agreement with a variational calculation based on the two-body Boltzmann equation for a unitary gas [Bruun and Smith 2007; Bluhm et al. 2017]. The leading correction from $\alpha_2$ depends only on the density. The red curve in Fig. 5.2 shows that $\eta_{\rm exp}(T/T_F)$ is in agreement with the measurements in the box potential for $T/T_F \geq 0.45$. At lower temperatures, $T/T_F < 0.4$, the shear viscosity measured in the box is consistently larger than that of the expanding cloud.

For comparison, the red-dashed curve shows the high temperature limit, where $\alpha_2 = 0$. Comparing the red curve and the red-dashed curve, we find that there is a significant density-dependent contribution to the shear viscosity. The top purple-dashed curve is a theory prediction of Enss et al. [2011], by evaluation of the Kubo formula within the T-matrix approximation. This prediction is in reasonable agreement with our data.

Our measured thermal conductivity, Fig. 5.3, can be compared with variational calculations for a unitary Fermi gas in the high temperature, two-body Boltzmann equation limit [Braby et al. 2010], where $\kappa_T(\theta) = 15/4\,\alpha_0\,\theta^{3/2}\,\hbar n\,k_B/m$, with $k_B$ the Boltzmann constant. The red-dashed line in Fig. 5.3 shows that the high temperature prediction is in reasonable agreement with measurements in the box potential for $T/T_F \geq 0.45$, without a temperature-independent correction. Note that, in contrast to the shear viscosity, the pure density dependent contribution to the high temperature thermal conductivity appears to be quite small. Meanwhile, our measured thermal conductivity is significantly smaller than some recent predictions (a Luttinger-Ward approach by Frank et al. [2020]; a Kubo-based microscopic calculation by Zhou and Ma [2021][2]).

For lower temperatures, $T/T_F < 0.4$, the thermal conductivity measured in the box

[2]As mentioned by the author, in their paper, the theory yields different Tc to experiments in the crossover regions, so a direct comparison between their plots with experiments may not be appropriate. However, we can estimate that our measurement is lower than their calculation, but in closer agreement compared to the prediction of Frank et al. [2020]

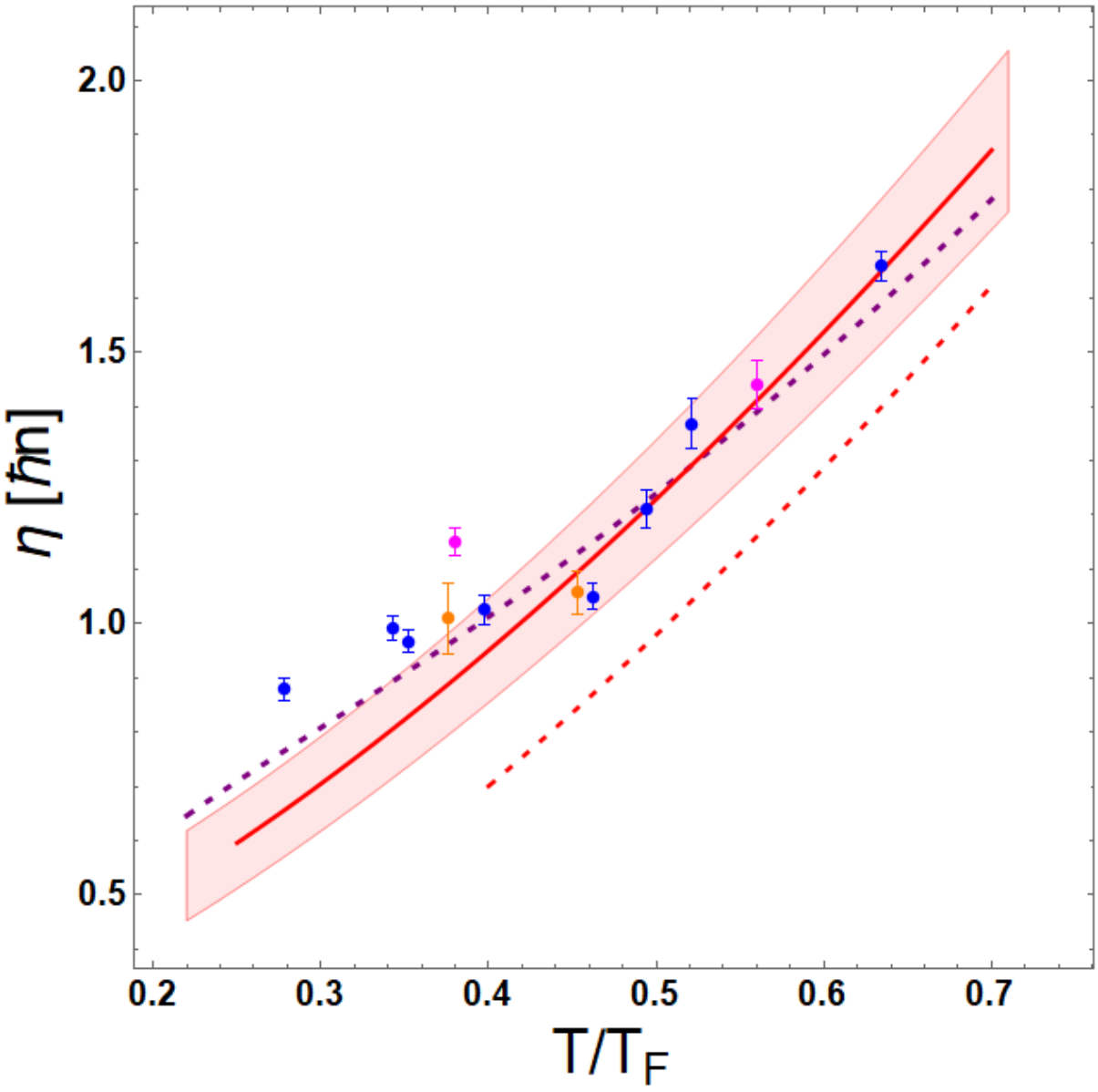


Figure 5.2: Shear viscosity $\eta$ in units of $\hbar n$ versus reduced temperature $T/T_F$. Blue dots: $\lambda \simeq 23\,\mu$m. Orange dots: Left (right) $\lambda = 18.2(18.9)\,\mu$m. Pink dots: Left (right) $\lambda = 32.3(41.7)\,\mu$m. Red solid curve: Fit to cloud expansion data, $\alpha_0\,\theta^{3/2} + \alpha_2$, where $\alpha_0 = 2.77, \alpha_2 = 0.25$ [Bluhm et al. 2017]. Shaded region denotes the standard deviation of the fit. Upper purple-dashed curve: Prediction of Enss et al. [2011]. Lower red-dashed curve: High temperature limit, $\alpha_0\,\theta^{3/2}$. Data error bars are statistical (see Sec. 4.3.1).

seems to be larger than the high temperature prediction, but is significantly smaller than the predictions by Frank et al. [2020]; Zhou and Ma [2021].

The sound diffusivity $D_1 = 2\,a/q^2$, in units of $\hbar/m$, Fig. 5.4, is determined by Eqs. 4.15 from the fit parameters $c_T q$, $\gamma_\eta$, and $\gamma_\kappa$. We obtain the same results within our error bars, by directly fitting $\Gamma$, $a$ and $b$ in Eq. 4.13, constraining $A_0/A$ using the long wavelength (LW) limit (see Sec. 5.2.3), where $b \simeq c_S q$ determines $T/T_F$. The red-dashed curve shows the predicted LW $D_1$, using the high temperature limits for both the shear viscosity and the thermal conductivity, with $c_{P_1} = 5/2\,k_B$ and $c_{V_1} = 3/2\,k_B$, i.e., $1/c_{V_1} - 1/c_{P_1} = 4/15$. For the red solid curve, the high temperature shear viscosity term in $D_1$ is replaced with the measured viscosity for the expanding gas, $\eta_{exp}(\theta)$ and the thermal conductivity term remains the same, i.e., $D_1 = 4/3(\alpha_0\,\theta^{3/2} + \alpha_2) + \alpha_0\,\theta^{3/2}$, yielding a good fit to the data for $T/T_F \geq 0.45$, consistent with our measured $\eta$ and $\kappa_T$. Our diffusivity data can be compared to that of Patel et al. [2020], which is shifted upward relative to that of Fig. 5.4, but exhibits nearly identical scaling with $T/T_F$. More details of sound diffusivity, including the comparison with Ref. Patel et al. [2020], will be discussed shortly in Sec. 5.1.1.

As can be seen in Figs. 5.2 $\sim$ 5.4, we use several perturbation wavelengths in the experiment, from 18 $\mu$m to 42 $\mu$m to check the $q$-dependence of our measured results. We compare data for $\lambda \simeq 23\,\mu$m to data points with $\lambda = 18.2\,\mu$m (4-spatial periods[3]), $18.9\,\mu$m (4-spatial periods), $32.3\,\mu$m (3-spatial periods) and $41.7\,\mu$m (2-spatial periods). These measurements show that there are no large systematic shifts with wavelength.

Meanwhile, we find that a perturbation wavelength $\lambda \simeq 23\,\mu$m yields good dynamic range for decay measurements over time scales that avoid perturbing $\delta n(z,t)$ in the measured central region by reflections from the walls of box potential, which then can be neglected (see Sec. 4.2). This explains why most of our experiments are using a perturbation wavelength of $23\,\mu$m.

[3]Number of spatial periods here indicates the range of the 1-D profile we use to perform the FFT, see Sec.4.2

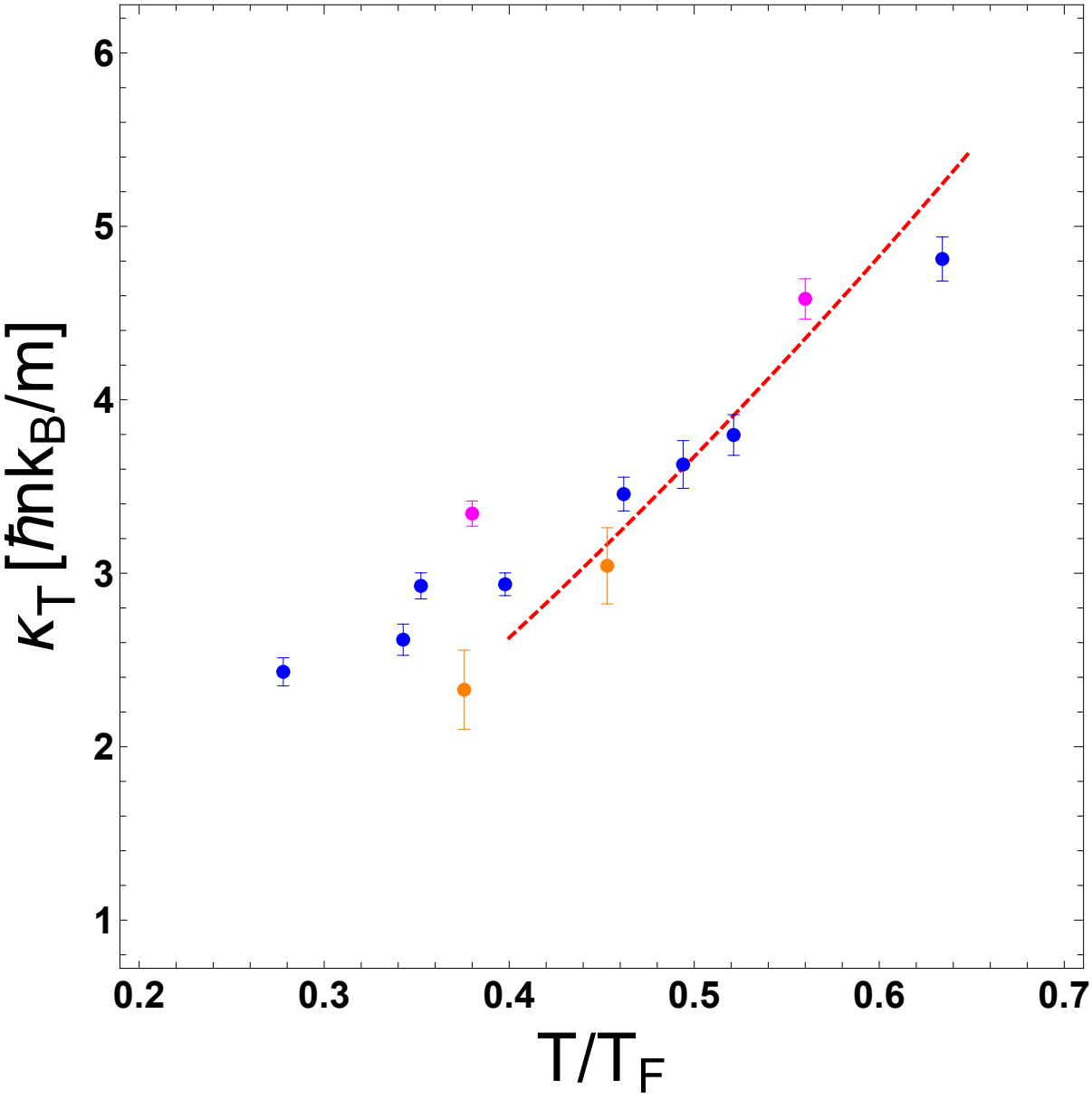


Figure 5.3: Thermal conductivity $\kappa_T$ in units of $\hbar n\, k_B/m$ versus reduced temperature $T/T_F$. Blue dots: $\lambda \simeq 23\,\mu$m. Orange dots: Left (right) $\lambda = 18.2\,(18.9)\,\mu$m. Pink dots: Left (right) $\lambda = 32.3\,(41.7)\,\mu$m. Red-dashed curve: High temperature limit, $15/4\,\alpha_0\,\theta^{3/2}$, where $\alpha_0 = 2.77$. Error bars are statistical (see Sec. 4.3.1).

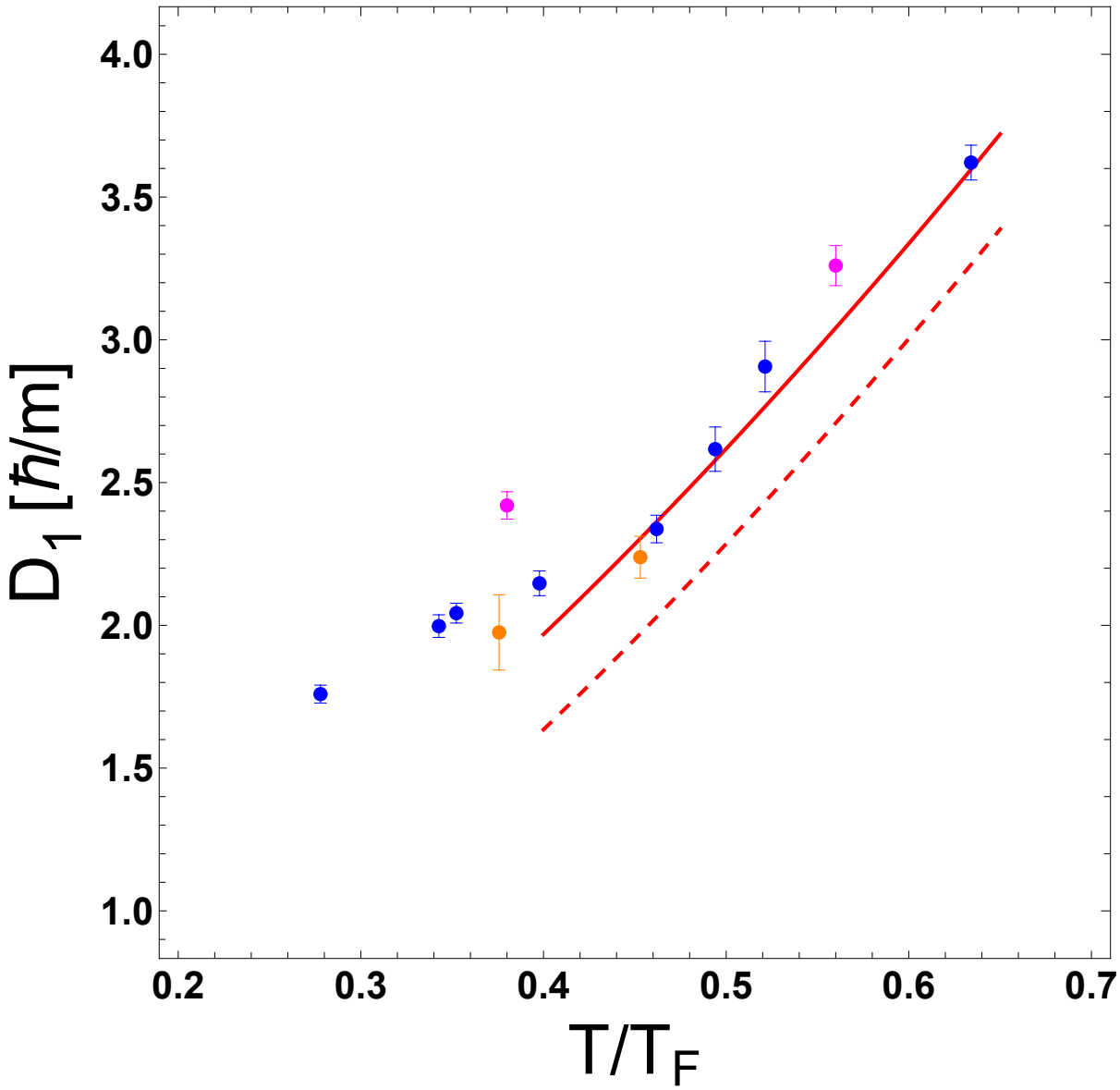


Figure 5.4: Sound diffusivity $D_1 = 2a/q^2$, in units of $\hbar/m$ versus reduced temperature $T/T_F$. Blue dots: $\lambda \simeq 23\,\mu$m. Orange dots: Left (right) $\lambda = 18.2(18.9)\,\mu$m. Pink dots: Left (right) $\lambda = 32.3(41.7)\,\mu$m. Red-dashed curve: Long wavelength, high temperature limit, $D_1 = 7/3\,\alpha_0\,\theta^{3/2}$. Red solid curve: $D_1 = 4/3\,(\alpha_0\,\theta^{3/2} + \alpha_2) + \alpha_0\,\theta^{3/2}$, where $\alpha_0 = 2.77, \alpha_2 = 0.25$. Error bars are statistical (see Sec. 4.3.1).

Since the measured hydrodynamic transport coefficients are particularly important for theoretical studies, here, we provide a complete table for our measurement of the coefficients, including the total central density[4] $n_0$ and perturbing wavelength $\lambda$.

Table 5.1: Measured Transport Coefficients

| $T/T_F$ | $\alpha_\eta$ | $\sigma_{\alpha_\eta}$ | $\alpha_\kappa$ | $\sigma_{\alpha_\kappa}$ | $D_1$ | $\sigma_{D_1}$ | $c_T[cm/s]$ | $\lambda[\mu m]$ | $n_0[cm^{-3}]$ |
|---|---|---|---|---|---|---|---|---|---|
| 0.278 | 0.879 | 0.021 | 2.432 | 0.081 | 1.759 | 0.032 | 1.185 | 23.53 | 6.20E+11 |
| 0.343 | 0.991 | 0.023 | 2.618 | 0.090 | 1.997 | 0.046 | 1.097 | 23.53 | 4.13E+11 |
| 0.352 | 0.967 | 0.021 | 2.928 | 0.075 | 2.043 | 0.038 | 1.197 | 24.10 | 5.24E+11 |
| 0.376 | 1.010 | 0.065 | 2.329 | 0.229 | 1.975 | 0.115 | 1.167 | 18.18 | 4.59E+11 |
| 0.381 | 1.149 | 0.026 | 3.348 | 0.072 | 2.423 | 0.048 | 1.078 | 32.26 | 3.58E+11 |
| 0.398 | 1.025 | 0.027 | 2.937 | 0.065 | 2.147 | 0.054 | 1.083 | 22.99 | 3.49E+11 |
| 0.453 | 1.057 | 0.041 | 3.044 | 0.220 | 2.240 | 0.076 | 1.201 | 18.87 | 4.22E+11 |
| 0.462 | 1.050 | 0.025 | 3.458 | 0.097 | 2.337 | 0.041 | 1.198 | 22.73 | 4.11E+11 |
| 0.494 | 1.211 | 0.035 | 3.628 | 0.138 | 2.617 | 0.079 | 1.118 | 22.99 | 3.13E+11 |
| 0.521 | 1.368 | 0.046 | 3.798 | 0.117 | 2.906 | 0.103 | 1.221 | 22.99 | 3.86E+11 |
| 0.557 | 1.440 | 0.044 | 4.596 | 0.118 | 3.256 | 0.071 | 1.139 | 41.67 | 2.94E+11 |
| 0.634 | 1.659 | 0.027 | 4.813 | 0.127 | 3.621 | 0.098 | 1.343 | 23.26 | 4.20E+11 |

Here, $\eta \equiv \alpha_\eta \hbar\, n_0$, $\kappa_T \equiv \alpha_\kappa \hbar\, n_0 (k_B/m)$, $D_1 = 2a/q^2$ is in units of $\hbar/m$, $c_T$ is the isothermal sound speed, $\lambda \equiv 2\pi/q$ is the perturbing wavelength and $n_0$ is the total central density for *both* spin states; $\sigma$ is the uncertainty (see Sec. 4.3.1).

### 5.1.1 Sound Diffusivity

In Chapter 2, from the model of a damped oscillator, we have shown that the measured $2\,a/q^2$ is, to a very good approximation, the usual first sound diffusivity [Landau and Lifshitz 1959],

$$\frac{2\,a}{q^2} = \frac{4}{3}\frac{\eta}{n_0 m} + \left(\frac{1}{c_{V_1}} - \frac{1}{c_{P_1}}\right)\frac{\kappa_T}{n_0} = D_1\,. \tag{5.8}$$

The same result follows immediately from the long wavelength (LW) limit (which we will discuss shortly in Sec. 5.2.3), where $c_S\, q >> \gamma_\kappa, \gamma_\eta$, although we do not require this approximation for the initial analysis of our data.

The analytic fits of Eq. 5.3 to the data, determine the measured sound diffusivity $2\,a/q^2$

[4]Note that what we actually measure is the density for one spin state, the total density $n_0$ is obtained simply by doubling the measured one-spin-density, since we use a 50-50 mixture.

shown in Fig. 5.4 and later in Fig. 5.5. The measured $2\,a/q^2$ can be compared to Eq. 5.8. For the unitary Fermi gas, where

$$\frac{1}{c_{V_1}} - \frac{1}{c_{P_1}} = \frac{1}{k_B}\frac{2}{3}\frac{\theta}{f_E(\theta)}, \tag{5.9}$$

Eq. 5.8 and Eq. 5.9, with Eqs. 5.1, and 5.2 yield

$$D_1(\theta) = \left[\frac{4}{3}\alpha_\eta(\theta) + \frac{2}{3}\frac{\theta}{f_E(\theta)}\,\alpha_\kappa(\theta)\right]\frac{\hbar}{m}. \tag{5.10}$$

Here, $f_E(\theta)$ is the measured universal function [Ku et al. 2012] that determines the energy density, Eq. 2.14. This universal function determines the heat capacities and the sound speeds employed in our data analysis, as described in Sec.2.1.2.

We evaluate the viscosity term in Eq. 5.10 using a diluteness expansion,

$$\alpha_\eta(\theta) = \alpha_0\,\theta^{3/2} + \alpha_2, \tag{5.11}$$

where $\alpha_0 = 45\pi^{3/2}/(64\sqrt{2}) \simeq 2.77$ [Bruun and Smith 2007; Bluhm et al. 2017]. Here, we include an $\alpha_2$ term, which arises from the purely density-dependent part of the viscosity. $\alpha_0 = 2.77(21)$ and $\alpha_2 = 0.25(08)$ are obtained from the fits to cloud expansion data [Bluhm and Schäfer 2016; Bluhm et al. 2017].

For the thermal conductivity term, we use the high temperature two-body Boltzmann equation limit [Braby et al. 2010],

$$\kappa_T = \frac{15}{4}\frac{k_B}{m}\,\eta. \tag{5.12}$$

This result follows from kinetic theory, where $\eta = \tau_\eta\, p$ and $\kappa_T = 5/2\, k_B/m\, \tau_\kappa\, p$, with $p$ the pressure. Using $\tau_\kappa = (3/2)\,\tau_\eta$, which can be shown to hold for any isotropic collision cross section, one obtains Eq. 5.12. This result is consistent with the thermal conductivities obtained in ref. [Braby et al. 2010] for a unitary Fermi gas and for a Fermi gas with a constant collision cross section. While Eq. 5.12 is rigorously derived only for the leading $\alpha_0$ term in $\eta$, we take

$$\alpha_\kappa(\theta) = \frac{15}{4}(\alpha_0\,\theta^{3/2} + \alpha_2'), \tag{5.13}$$

to include a pure density-dependent correction.

Using Eqs. 5.11 and 5.13, the sound diffusivity for a unitary Fermi gas, Eq. 5.10, takes the form

$$D_1(\theta) = \left[\frac{4}{3}(\alpha_0\,\theta^{3/2} + \alpha_2) + \frac{5}{2}\frac{\theta}{f_E(\theta)}\,(\alpha_0\,\theta^{3/2} + \alpha_2')\right]\frac{\hbar}{m}, \tag{5.14}$$

where $5/2\,\theta/f_E(\theta) = n\,k_B\,T/p$, as we have proven in chapter 2.

The red-dashed curve in Fig. 5.4 shows the high temperature classical limit of eq. 5.14 where $p = n\,k_B\,T$ and $5/2\,\theta/f_E(\theta) \to 1$. Here, we take $\alpha_2 = \alpha_2' = 0$, so that $D_1 = 7/3\,\alpha_0\,\theta^{3/2}$ with $\alpha_0 = 2.77$. The red-solid curve in Fig. 5.4 shows Eq. 5.14 with $\alpha_2 = 0.25$, consistent with our shear viscosity data, and $\alpha_2' = 0.0$, consistent with our thermal conductivity data. For simplicity, we again take the classical limit with $5/2\,\theta/f_E(\theta) \to 1$. The good fit to our sound diffusivity data demonstrates the consistency with our extracted transport properties, $\eta$ and $\kappa_T$.

Similar results are obtained using the $f_E(\theta)$ from the measured equation of state [Ku et al. 2012] in Eq. 5.13 with $5/2\,\theta/f_E(\theta) = n\,k_B\,T/p$. This is shown in Fig. 5.5.

In Fig. 5.5, we also compare our data with those of Patel et al. [2020] (red dots). In both data sets, the error bars are statistical, and denote $1\,\sigma$. For our data, we show the statistical error from the $\chi^2$ fits. We estimate a systematic *downward* shift of $\leq 5\%$, arising from the density variation, as discussed in Sec.5.2.1. For Patel et al. [2020], the estimated systematic error is 13%, arising from the width of the end caps. We observe an upward shift of the diffusivity data of Patel et al. [2020], compared to that of the present work, but the scaling of the normal fluid diffusivity with reduced temperature $T/T_F$ is in good agreement.

It is also interesting to compare our data with those of Patel et al. [2020] by fitting both with $D_1 = 4/3\,(\alpha_0\,\theta^{3/2} + \alpha_2) + \alpha_0\,\theta^{3/2}$ with $\alpha_0 = 2.77$, and chosing different value for $\alpha_2$. Fig. 5.6 shows the same trend of the two measurements, while the optimal $\alpha_2$ appear to be differ by 0.7. This is interesting for future theoretical studies.

## 5.2 Systematic Shifts of the Results

In this section, we discuss some important details of our theoretical model and measured results to evaluate possible shifts, including an estimation for the effect of density variation on the measured results, a consistency check by calculating the stored energy in the initial perturbation, and a discussion of the long wavelength (LW) approximation.

### 5.2.1 Effect of Density Variation on the Measured Transport Coefficients

Figs. 5.2 - 5.4 and Table. 5.1 show the measured transport coefficients, where the error bars denote the statistical errors from the $\chi^2$ fits, which we find from the error matrix (see Sec. 4.3.1). The transport coefficients $\alpha_\eta$ and $\alpha_\kappa$, and $2\,a/q^2$, are determined by Eqs. 5.4-5.6, which do not explicitly depend on the density.

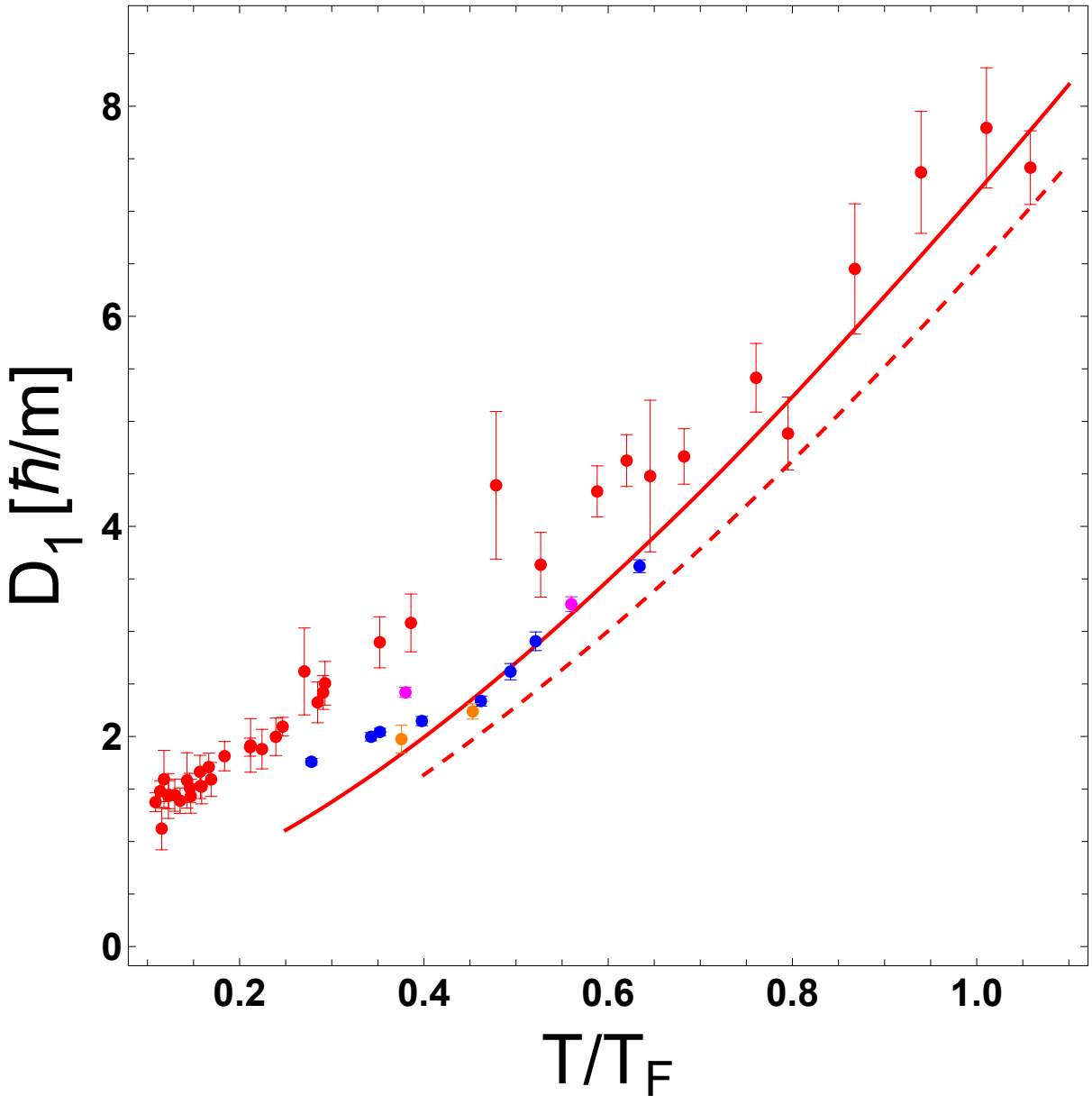


Figure 5.5: Sound diffusivity, $D_1 = 2\,a/q^2$, in units of $\hbar/m$ versus reduced temperature $\theta = T/T_F$. Blue, Orange and Pink dots: Current work. Red dots: Patel et al. [2020]. Red-dashed curve: Long wavelength, high temperature limit, $D_1 = 7/3(\alpha_0\,\theta^{3/2})$, where $\alpha_0 = 2.77$. Red solid curve: $D_1 = 4/3(\alpha_0\,\theta^{3/2} + \alpha_2) + (n\,k_B\,T/p)\,\alpha_0\,\theta^{3/2}$.

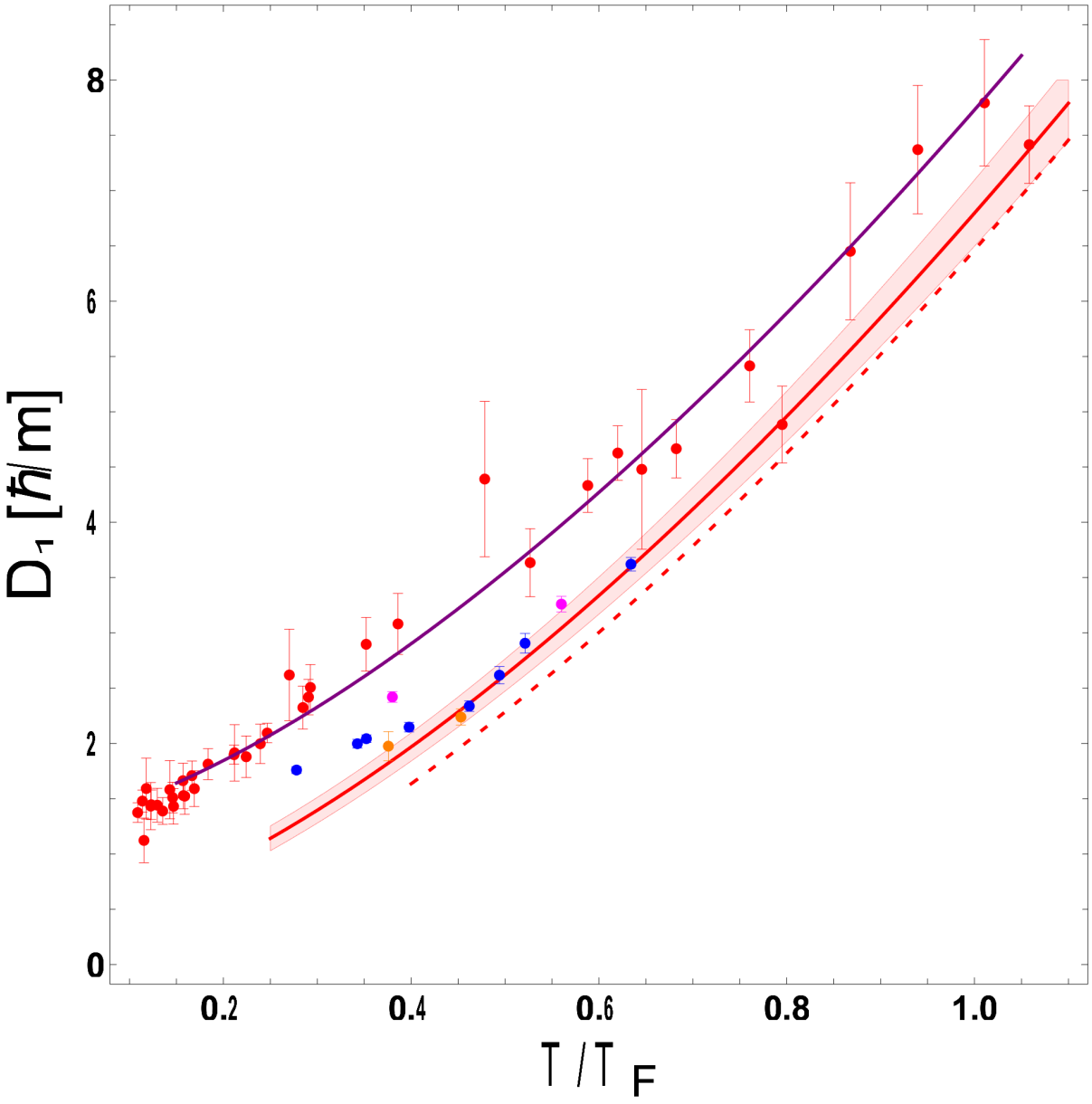


Figure 5.6: Another comparison of sound diffusivity, $D_1 = 2\,a/q^2$, in units of $\hbar/m$ versus reduced temperature $\theta = T/T_F$. Blue, Orange and Pink dots: Current work. Red dots: Patel et al. [2020]. Red-dashed curve: Long wavelength, high temperature limit, $D_1 = 7/3(\alpha_0\,\theta^{3/2})$, where $\alpha_0 = 2.77$. Red solid curve: $D_1 = 4/3(\alpha_0\,\theta^{3/2} + \alpha_2) + \alpha_0\,\theta^{3/2}$, with $\alpha_2 = 0.25$. Shaded region denotes the standard deviation of the fit to first term on the right-hand side [Bluhm et al. 2017]. Purple solid curve: $D_1 = 4/3(\alpha_0\,\theta^{3/2} + \alpha_2) + \alpha_0\,\theta^{3/2}$, with $\alpha_2 = 0.95$.

However, the measured decay rates are inherently averages over the sample. To estimate the effect of the density variation, we consider the high temperature limit, where $c_T \propto \sqrt{T}$ is independent of density, as are the transport properties, $\eta$ and $\kappa_T$, which are $\propto T^{3/2}$. The decay rates then scale inversely with density, $\gamma_\eta \equiv \gamma_\eta(0)\, n_0/n$, and $\gamma_\kappa \equiv \gamma_\kappa(0)\, n_0/n$, so that the decay rates are larger in the low density regions compared to the center, where $n(0) = n_0$.

In a simple model, we can average the exponential decay factors with a normalized density profile for the region measured in our 160 $\mu$m boxes, where the density variation over the central 100 microns is $\simeq 10\%$. We use the central values $\gamma_\eta(0)$ and $\gamma_\kappa(0)$ as fit parameters, since these correspond to the density $n_0$ that determines $T/T_F$ in the figures. These fit parameters are adjusted so that the average decay factors agree with the measurements. We find that $\gamma_\eta(0)$ and $\gamma_\kappa(0)$ are shifted *downward* by 5% compared to the measured values. These results are confirmed by numerical modeling of $\delta n(z,t)$ with Eqs. 4.1 and 4.2, where we find a downward shift of 3-9% for $\gamma_\eta(0)$ and 1-4% for $\gamma_\kappa(0)$ (see Sec. 4.2.2).

We also compute the corresponding average for the density profile $n(y)$ along the line-of-sight direction, where we cannot choose the central region. We divide the density $n(y)$ into 30 segments, find $\delta n(q,t)$ for each segment, and sum the density weighted decay curves, yielding comparable down shifts.

From these estimates, we see that the corrected transport parameters, corresponding to the central density $n_0$ and the given $T/T_F$, are systematically shifted *downward*, compared to the given measured values, by at most 5% for an average, and no more than 10% for any individual measurement shown in Figs. 5.2 - 5.4 and Table. 5.1.

### 5.2.2 Stored Energy

We also estimate the change in the energy per particle $W_1$ that arises from the energy stored in the initial spatially periodic density profile. This is important since we assume the average energy per particle does not change during the entire evolution.

The initial density perturbation stores energy, which is converted into kinetic energy after the perturbation is extinguished and finally into heat. To show that the change in the average energy per particle is negligible, we determined the stored energy $W$ for the ideal case of an adiabatic change of the density, $\delta n$, starting from a uniform density $n_0$. As the total number of atoms does not change during the compression, we must have

$$\int d^3\mathbf{r}\, \delta n(\mathbf{r}) = 0. \tag{5.15}$$

Now consider a small volume $\Delta V$ of the cloud, containing a small number of atoms $\Delta N = n\,\Delta V$. Changing the volume for fixed $\Delta N$, we have $d\,\Delta N = d\,n\,\Delta V + n\,d\,\Delta V = 0$. Taking $n \simeq n_0$, the density before perturbation is applied, we have

$$d\,\Delta V = -\Delta V\,\frac{d\,n}{n_0}. \tag{5.16}$$

The work to change $\Delta V$ by $d\,\Delta V$ is just

$$d\,\Delta W = -p\,d\,\Delta V = (p_0 + \delta p)\Delta V\,\frac{d\,n}{n_0}. \tag{5.17}$$

Then the net work to change the local density from $n_0$ to $n$ is

$$\Delta W = \Delta V \int_{n_0}^{n} \frac{d\,n}{n_0}(p_0 + \delta p). \tag{5.18}$$

Using as the integration variable the local change in density $\delta\,n \equiv n - n_0$, $d\,n = d\,\delta\,n$. Assuming an adiabatic change in pressure, $p - p_0 \equiv \delta p = m\,c_S^2\,\delta\,n$, with $c_S$ the adiabatic sound speed and $p_0$ the uniform background pressure, we have

$$\Delta W = \Delta V \int_0^{\delta n} \frac{d\,\delta\,n'}{n_0}(p_0 + m\,c_S^2\,\delta\,n') = \Delta V \left(\delta\,n\,\frac{p_0}{n_0} + m\,c_S^2\,\frac{(\delta\,n)^2}{2\,n_0}\right). \tag{5.19}$$

Replacing the local volume $\Delta V$ by $d^3\mathbf{r}$, we have for the total stored energy

$$W = \int d^3\mathbf{r}\left(\delta\,n\,\frac{p_0}{n_0} + m\,c_S^2\,\frac{(\delta\,n)^2}{2\,n_0}\right) \simeq \frac{m\,c_S^2}{2}\int d^3\mathbf{r}\,n_0\left[\frac{\delta\,n(\mathbf{r})}{n_0}\right]^2. \tag{5.20}$$

In Eq. 5.20, since the background pressure $p_0$ and density $n_0$ are spatially uniform, Eq. 5.15 requires that the term linear in $\delta\,n$ vanish. For simplicity, we ignore the spatial variation of the sound speed $c_S$ and background density $n_0$ in the region of the perturbation. Defining the energy per particle $W_1 = W/N$ in terms of the mean square fractional density perturbation, we have finally

$$W_1 = \frac{m\,c_S^2}{2}\left\langle\left[\frac{\delta\,n(\mathbf{r})}{n_0}\right]^2\right\rangle. \tag{5.21}$$

The same result can be obtained by finding the rate of change of the total kinetic energy $K$

from the dissipationless equation of motion $n_0 m \partial_t \mathbf{v} = -\nabla \delta p$. Starting from

$$n_0 m \partial_t \mathbf{v}^2 = -\mathbf{v} \cdot \nabla \delta p. \tag{5.22}$$

and defining the total kinetic energy integrating over volume, we have

$$K \equiv \int d^3\mathbf{r} \frac{m\mathbf{v}^2}{2}, \tag{5.23}$$

$$\partial_t K = -\int d^3\mathbf{r}\, \mathbf{v} \cdot \nabla \delta p = \int d^3\mathbf{r}\, \nabla \cdot \mathbf{v} \delta p. \tag{5.24}$$

From the continuity equation $\delta \dot{n} + n_0 \nabla \cdot \mathbf{v} = 0$, and using $\delta p = m c_S^2 \delta n$, we have

$$\begin{aligned} \partial_t K &= -\int d^3\mathbf{r} \frac{\delta \dot{n}}{n_0} \delta p = -m c_S^2 \int d^3\mathbf{r} \frac{\delta \dot{n}}{n_0} \delta n \\ &= -\frac{m c_S^2}{2} \partial_t \int d^3\mathbf{r}\, n_0 \left(\frac{\delta n}{n_0}\right)^2 \end{aligned} \tag{5.25}$$

Finally from $\partial_t (K + W) = 0$, we see that $W$ is the effective potential energy. Dividing $W$ by the atom number $N$, we obtain the same result for $W_1$, i.e., Eq. 5.21.

Note that for a unitary Fermi gas, $m c_S^2 = 10\, E_1/9$ from Eq. 2.18. For a sinusoidal perturbation with a 20% amplitude, $\delta n / n_0 \simeq 0.2 \cos(qz)$, we have $W_1 \simeq 0.01\, m c_S^2$. As $m c_S^2 = 10/9\, E_1$, with $E_1$ the energy per particle [Patel et al. 2020], the change in $E_1$, and hence in $\theta = T/T_F$, is negligible.

### 5.2.3 Long Wavelength Limit

Our hydrodynamic linear response model is based on an application of the fluid dynamics in many-body quantum system, which requires some validity considerations.

Despite its classical history, fluid dynamics can be used as an effective theory for the long-distance, long-time properties of any material. The only requirement for the applicability of fluid dynamics is that the system relaxes to approximate local thermodynamic equilibrium on the time scale of the observation [Schäfer 2014].

According to Schäfer's description, there are two basic time scales associated with the behavior of a many body system. The first is a microscopic time scale $\tau_{fluid}$ that characterizes the rate at which a generic disturbance relaxes. The second time scale $\tau_{diff}$ is associated with the relaxation of conserved charges, decaying by diffusion or collective

motion. In a normal non-relativistic fluid, the conserved charges are the mass density, the momentum density, and the energy density. The gradient expansions of these conserved charges give us transport coefficients, the shear viscosity $\eta$, the bulk viscosity $\zeta$ and the thermal conductivity $\kappa_T$ [Schäfer 2014].

Fluid dynamics is based on the separation of scales $\tau_{fluid} \ll \tau_{diff}$, where the time $\tau_{diff}$ increases with the length scale $\lambda$ of the disturbance, i.e. $\tau_{diff} \propto \lambda^2$. This condition $\tau_{fluid} \ll \tau_{diff}$ can be referred as the long wavelength (LW) limit.

In our case, the fastest time scale for the changes in density and temperature is set nominally by the adiabatic sound frequency $\omega_S$ of the first sound mode, i.e., $\tau_{diff} = \omega_S^{-1}$. So the LW limit requires $\omega_S \tau_{fluid} \ll 1$. Wit $\omega_S = c_S q$, the LW limit effectively requires that $q$ is small.

Starting from our analytic solutions, there are two ways to check whether long wavelength approximation is valid. First, rewriting Eqs. 5.4 and 5.5,

$$b^2 - c_S^2 q^2 = \gamma_\eta \gamma_\kappa - 2a\Gamma - a^2 \tag{5.26}$$

$$a = \frac{1}{2}(\gamma_\eta + \gamma_\kappa - \Gamma). \tag{5.27}$$

Note that $\gamma_\eta, \gamma_\kappa, \Gamma \propto q^2$, and from Eq. 5.27, $a$ is easily found as $\propto q^2$. $b \simeq \sqrt{\omega_S^2 - a^2}$ – the damped oscillation frequency of the first sound, $\ddot{x} + 2a\dot{x} + \omega_S^2 x = 0$ (see Sec. 2.2.3), should also be a function of $q$. In the long wavelength limit, $q$ is small. The right-hand side of Eq. 5.26, $\propto q^4$, while on the left-hand side $c_S^2 q^2$ is of course $\propto q^2$. This means the right-hand side is close to 0 for small q, and thus $b \simeq c_S q \equiv \omega_S$. In our experiments, where the typical $\lambda \simeq 23\,\mu$m, we find that $b$ is smaller than $\omega_S$ by 2.2 %, 4.3 % and 5.7 % for $T/T_F = 0.28, 0.46$, and 0.63, respectively, close to the LW limit. A data-by-data comparison is provided in Table. 5.2.

Second, we can rewrite Eq. 4.16 as

$$\frac{A_0}{A} = \frac{a^2 + b^2 - \omega_T^2}{(\Gamma - a)^2 + b^2}. \tag{5.28}$$

For $b^2 \gg a^2, (\Gamma - a)^2$ in the LW limit, we have

$$\frac{A_0}{A} \simeq \frac{b^2 - \omega_T^2}{b^2}. \tag{5.29}$$

Since $b \simeq \omega_S$, from Eq.5.29 and $\omega_S^2/\omega_T^2 = c_{P_1}/c_{V_1}$, we obtain

$$\frac{A_0}{A} = 1 - \frac{\omega_T^2}{\omega_S^2} = 1 - \frac{c_{V_1}}{c_{P_1}}. \tag{5.30}$$

Here, LW limit requires $A_0/A = 1 - c_{V_1}/c_{P_1}$, which is $\simeq 0.3$ for our $T/T_F$ range. As a cross check, we compare the $A_0/A$, where $A$ is from the fit and $A_0 = (a^2 + b^2 - \omega_T^2/(\Gamma - a)^2 + b^2)A$, with the calculated $1 - c_{V_1}/c_{P_1}$ from the equation of state. We find the difference is within 5.3%, as showed in Table. 5.2.

From these cross checks, we can see that all our data is close to the long wavelength limit, which suggests our hydrodynamic method is appropriate.

Table 5.2: Validity of the Long Wavelength Limit

| $T/T_F$ | $\omega_S$ | $b$ | $\frac{\omega_S - b}{\omega_S}$ | $\frac{\omega_S - \sqrt{a^2+b^2}}{\omega_S}$ | $A_0/A$ | $1 - c_{V_1}/c_{P_1}$ |
|---|---|---|---|---|---|---|
| 0.278 | 3707.5 | 3625.9 | 2.20% | 0.58% | 0.265 | 0.271 |
| 0.343 | 3479.3 | 3374.6 | 3.01% | 0.63% | 0.289 | 0.292 |
| 0.352 | 3716.1 | 3609.3 | 2.87% | 0.89% | 0.284 | 0.294 |
| 0.376 | 4825.3 | 4646.6 | 3.70% | 0.30% | 0.312 | 0.301 |
| 0.381 | 2514.9 | 2449.7 | 2.59% | 0.70% | 0.297 | 0.303 |
| 0.398 | 3556.7 | 3418.4 | 3.89% | 0.98% | 0.301 | 0.307 |
| 0.453 | 4857.6 | 4619.2 | 4.91% | 1.15% | 0.319 | 0.322 |
| 0.462 | 4034.5 | 3862.0 | 4.28% | 1.45% | 0.310 | 0.324 |
| 0.494 | 3737.0 | 3541.3 | 5.24% | 1.29% | 0.328 | 0.332 |
| 0.521 | 4101.1 | 3902.9 | 4.83% | 0.81% | 0.347 | 0.338 |
| 0.557 | 2123.5 | 2074.3 | 2.32% | 0.60% | 0.345 | 0.346 |
| 0.634 | 4538.1 | 4279.6 | 5.70% | 0.81% | 0.380 | 0.361 |

Here, $a, b, A, A_0$ are fit parameters to Eq. 5.3, $\omega_S$ is the calculated adiabatic sound frequency. $c_{V_1}$, $c_{P_1}$ are heat capacity per particle at constant volume and pressure, respectively, calculated by the equation of state with fitted reduced temperature $\theta$.

## 5.3 Breakdown of Hydrodynamics

In our hydrodynamic linear response model, we apply a long wavelength (LW) approximation which assumes instantaneous relaxation to local equilibration, or in other words,

a zero relaxation time $\tau \simeq 0$. However, the relaxation rate $\tau^{-1}$ is not infinity even in our strongly interacting system.

For a finite relaxation time, it is interesting to take a glance at microscopic theories that provides second order corrections to the transport coefficients.

The simplest microscopic description of a fluid is kinetic theory, which describes the long distance behavior of an underlying classical or quantum many-body system [Schäfer 2014]. Kinetic theory can be used to relate properties of long-lived quasi-particles, such as masses and scattering cross sections, to the equation of state and the transport coefficients.

The basic concept of kinetic theory applies to solve the Boltzmann equation of the quasi-particle distribution function $f(\boldsymbol{r}, \boldsymbol{p}, t)$, i.e.,

$$\left(\frac{\partial}{\partial t} + \boldsymbol{v}\frac{\partial}{\partial \boldsymbol{r}} - \frac{\partial V}{\partial \boldsymbol{r}}\frac{\partial}{\partial \boldsymbol{p}}\right) f = -I[f], \tag{5.31}$$

where $V$ is the trapping potential and $I[f]$ is the collision term. In the relaxation-time approximation [Bhatnagar et al. 1954], the collision integral of the Boltzmann equation becomes $I[f] = \delta f/\tau$, where $\delta f = f - f_0$ is the deviation of the distribution function from local equilibrium and $\tau$ is the relaxation time. Solving the Boltzmann equation gives us connections between the static transport coefficients with the finite relaxation time.

In kinetic theory, the static shear viscosity takes the form $\eta = \tau_\eta p$ [Chapman et al. 1990], where $p$ is the pressure and $\tau_\eta$ is a collisional relaxation time. Similarly, the static thermal conductivity is $\kappa_T = (5/2)(k_B/m)\tau_\kappa p$. For a unitary Fermi gas, the pressure is $p = \frac{2}{5} n \epsilon_F(n) f_E(\theta$, so for the shear viscosity we have

$$\tau_\eta = \frac{5}{2}\frac{\hbar}{\epsilon_F(n)}\frac{\alpha_\eta(\theta)}{f_E(\theta)}. \tag{5.32}$$

Similarly, for the thermal conductivity, we have

$$\tau_\kappa = \frac{\hbar}{\epsilon_F(n)}\frac{\alpha_\kappa(\theta)}{f_E(\theta)}. \tag{5.33}$$

From above, we can see the relaxation times are characterized by the transport scattering times, which are functions of density and temperature. In our experiments, the relaxation times are $\sim 100\mu$s, which are listed in Table.5.3.

In the long wave length (LW) limit, these relaxation times need to be small compared to the time scale for density and temperature changes, set nominally by the adiabatic sound frequency $\omega_S$ of the first sound mode. So, for a given $\omega_S$, the LW limit generally requires a

sufficiently high density and a low temperature of the gas. Hence, we would expect that a relaxation time correction is significant for the data taken at the lowest densities and the highest temperatures in our experiments, where the shallow box potential prevents measurements at both high temperature and high density.

We can relate the desired static transport properties to those measured at finite frequency by using a simple Drude model. Before we use this model, it is important to point out this is not a rigorous way to correct our measurements. First, the Drude model is only a crude estimate for the second order hydrodynamic effects, and it has not been proven to be true in the strongly interacting normal fluid regime where we working. Second, as mentioned before, we actually measure the thermal conductivity $\kappa_T$ from the thermal diffusion mode, and obtain the shear viscosity $\eta$ from $D_\eta$, which is by subtracting the contribution of $D_\kappa$ from the first sound diffusivity $D_1 = D_\eta + D_\kappa$. So a direct correction by Drude model to $\eta$ and $\kappa_T$ may not be appropriate.

However, the purpose of giving an example of Drude model here is to demonstrate how breakdown of first order hydrodynamics could effect our measured results, and also to estimate the extreme cases of possible corrections to our measurement. More rigorous studies are expected in the future.

In the Drude approximation Braby et al. [2011]; Enss [2012], the viscosity measured at finite frequency $\eta(\omega)$ is related to the static viscosity $\eta(0)$ by

$$\eta(\omega) = \frac{\eta(0)}{1+(\omega\tau_\eta)^2} \tag{5.34}$$

and similarly for $\kappa_T(\omega)$.

We take $\omega \simeq \omega_S$, the adiabatic frequency for data taken with a spatial period $\lambda$, is just $\omega_S = (2\pi/\lambda)\, c_S(\theta)$. Here, the adiabatic sound speed $c_S(\theta) = v_F\sqrt{f_E(\theta)/3}$ from Eq. 2.18, where $f_E(\theta)$ is determined by the measured equation of state Ku et al. [2012], and $v_F = \sqrt{2\,\epsilon_F(n)/m}$ is the Fermi speed, with $n$ the total density. Using these results, we find

$$\omega_S\tau_\eta \simeq 5\pi\sqrt{\frac{2\,\hbar^2}{3\,m\lambda^2\,\epsilon_F(n)}}\,\frac{\alpha_\eta(0)}{\sqrt{f_E(\theta)}} \tag{5.35}$$

and

$$\omega_S\tau_\kappa \simeq 2\pi\sqrt{\frac{2\,\hbar^2}{3\,m\lambda^2\,\epsilon_F(n)}}\,\frac{\alpha_\kappa(0)}{\sqrt{f_E(\theta)}}, \tag{5.36}$$

where the static viscosity coefficient $\alpha_\eta(0)$ and the static thermal conductivity coefficient

$\alpha_\kappa(0)$ are defined by Eqs. 2.43 and 2.44.

Letting $\alpha_\eta(\omega_S)$ be the measured shear viscosity coefficient, we estimate the static viscosity coefficient,

$$\alpha_\eta(0) = [1 + (\omega_S \tau_\eta)^2)]\,\alpha_\eta(\omega_S), \tag{5.37}$$

where we can approximate $\alpha_\eta(0)$ on the right hand side of eq. 5.35 by the measured value $\alpha_\eta(\omega_S)$ for simplicity, when the correction is not too large. Similarly, we estimate the static thermal conductivity coefficient from the measured value,

$$\alpha_\kappa(0) = [1 + (\omega_S \tau_\kappa)^2)]\,\alpha_\kappa(\omega_S), \tag{5.38}$$

replacing $\alpha_\kappa(0)$ on the right hand side of eq. 5.36 by the measured value $\alpha_\kappa(\omega_S)$.

Eqs. 5.37 and 5.38 give us a crude estimation on what corrections could be made for the measured transport coefficients. In this Drude model, our measured shear viscosity and measured thermal conductivity is shifted upward, depending on the different relaxation rates, densities and perturbing wavelengths, as listed in Table.5.3. For data taken with high density or long perturbing wavelength, the Drude shift is small. The shift is more significant for data taken with both a low density and a short wavelength. We also list the decay rates $\gamma_\eta$, $\gamma_\kappa$ and the adiabatic sound frequency $\omega_S$ in Table.5.3, giving a direct comparison of all the time scales in our experiments for readers of interests.

Although these results suggest that the static transport coefficients need to be shifted up compared to what we measured, we do not expect large changes to our conclusion since most of our data is taken at relatively low temperature and higher density, as shown in Table. 5.3. Again, the Drude model is a crude way to evaluate second order behavior. In the strongly interacting normal fluid region, the gas is not simply Bolzmann quasi-particles. The appropriate relaxation times and the characteristic time scale of disturbance also need to be more carefully defined. In the analysis provided above, we chose the fastest time scale $\omega_S$ to estimate the extreme cases, while the exponential decay rate $\Gamma$ can also be considered as the characteristic time scale. Using this slower frequency would result in less upward shifts compared to those in Table.5.3.

Based on the above discussion, a more rigorous second order hydrodynamic description is expected to shed additional light on our measured results. Meanwhile, it illustrates the ideal condition for future studies for the first order hydrodynamics, i.e., a perturbation of very long wavelength in a gas of very high density[5]. Also, it is instructive to design

[5]The high density setup is already accomplished based on current method, e.g., the USTC group of Ref. Li et al. [2022] achieved a density of $n \simeq 1.6 \times 10^{13}\, c\, m^{-3}$.

Table 5.3: Comparison of Time Scales and Drude Corrections

| $T/T_F$ | $\gamma_\eta$ | $\gamma_\kappa$ | $\omega_S$ | $\tau_\eta$ | $\tau_\kappa$ | $\Delta\eta$ | $\Delta\kappa_T$ | $\lambda[\mu m]$ | $n_0[cm^{-3}]$ |
|---|---|---|---|---|---|---|---|---|---|
| 0.278 | 881.96 | 1831.17 | 3707.5 | 80.54 | 88.96 | 8% | 10% | 23.53 | 6.20E+11 |
| 0.343 | 994.29 | 1970.86 | 3479.3 | 102.7 | 108.6 | 12% | 14% | 23.53 | 4.13E+11 |
| 0.352 | 925.65 | 2101.79 | 3716.1 | 83.72 | 101.4 | 9% | 14% | 24.10 | 5.24E+11 |
| 0.376 | 1697.62 | 2936.47 | 4825.3 | 90.88 | 83.84 | 19% | 16% | 18.18 | 4.59E+11 |
| 0.381 | 613.71 | 1341.10 | 2514.9 | 121.3 | 141.3 | 9% | 12% | 32.26 | 3.58E+11 |
| 0.398 | 1078.02 | 2316.61 | 3556.7 | 106.39 | 121.9 | 14% | 18% | 22.99 | 3.49E+11 |
| 0.453 | 1650.24 | 3563.71 | 4857.6 | 87.39 | 100.7 | 18% | 23% | 18.87 | 4.22E+11 |
| 0.462 | 1129.95 | 2790.10 | 4034.5 | 87.18 | 114.8 | 12% | 21% | 22.73 | 4.11E+11 |
| 0.494 | 1272.99 | 2861.71 | 3737.0 | 114.2 | 137 | 18% | 26% | 22.99 | 3.13E+11 |
| 0.521 | 1438.09 | 2995.67 | 4101.1 | 107.1 | 119 | 19% | 23% | 22.99 | 3.86E+11 |
| 0.557 | 460.87 | 1103.35 | 2123.5 | 128 | 163.5 | 7% | 12% | 41.67 | 2.94E+11 |
| 0.634 | 1704.56 | 3709.63 | 4538.1 | 103.6 | 120.2 | 22% | 29% | 23.26 | 4.20E+11 |

Here, $\gamma_\eta = (4\hbar q^2/3m)\alpha_\eta$, $\gamma_\kappa = (k_B\hbar q^2/c_{V_1} m)\alpha_\kappa$ are the decay rates as we defined in Sec. 5.1, $\omega_S$ is the adiabatic sound frequency. These three are all in units of inverse second in the table. $\tau_\eta$ and $\tau_\kappa$ are relaxation times for $\eta$ and $\kappa_T$, respectively, in units of microsecond. $\Delta_\eta$ and $\Delta_{\kappa_T}$ are *upward* shift percentage by the Drude model for $\eta$ and $\kappa_T$, respectively. $\lambda$ is the perturbing wavelength and $n_0$ is the total density for *both* spin states.

experiments studying higher order behavior by gradually reducing the wavelength and density, with independent controls.

CHAPTER

# 6

# CONCLUSION

## 6.1 Summary

This dissertation has presented new time-domain, free evolution methods for measuring hydrodynamic transport coefficients in a normal fluid unitary Fermi gas. The thermal conductivity and the shear viscosity in a universal normal fluid have been measured independently for the first time.

I have demonstrated the theoretical basis and experimental setup for measuring the free decay of a sinusoidal density profile in a normal fluid strongly interacting Fermi gas.

In the experiment, the gas was confined in a box potential, creating a near-homogeneous sample before being perturbed. The spatial profile was initially created in thermal equilibrium by a perturbing potential. After the perturbation was abruptly extinguished, the dominant spatial Fourier component exhibited an exponentially decaying (thermally diffusive) mode and a decaying oscillatory (first sound) mode, enabling independent measurement of the thermal conductivity $\kappa_T$ and the shear viscosity $\eta$ directly from the time-dependent evolution.

This dissertation has also shown that the oscillatory decay of a spatially periodic density

perturbation well distinguishes these two modes. For the isothermal static initial conditions employed in the experiments, the thermally diffusive exponentially decaying mode comprises $\simeq 32\%$ of the initial total amplitude of the dominant Fourier component, which is readily apparent in the free hydrodynamic relaxation. This mode enables independent measurement of the thermal conductivity $\kappa_T$. The oscillatory decaying first sound mode determines the sound diffusivity $D_1 = D_\eta + D_\kappa$, yielding independent measurement of the shear viscosity $\eta$.

For our results, we find that the shear viscosity measured by this free hydrodynamic relaxation in the box is consistent with that extracted from data on expanding cloud by Bluhm and Schäfer [2016]; Bluhm et al. [2017], which includes a significant density-dependent contribution, for reduced temperatures $T/T_F > 0.45$. At lower temperatures, $T/T_F < 0.4$, the shear viscosity measured in this relaxation experiment is consistently larger than that extracted from the expanding cloud. The thermal conductivity for $T/T_F > 0.45$ is close to the high temperature limit. In contrast to the shear viscosity, the pure density dependent contribution to the high temperature thermal conductivity appears to be quite small. The measured sound diffusivity can be compared to that of Patel et al. [2020], which is shifted upward relative to ours, but exhibits nearly identical scaling with $T/T_F$ and appears to converge at low temperatures.

These results emphasize the need for rigorous calculations of the leading density-dependent corrections to the two-body high temperature limits.

The method in this dissertation is complementary to frequency domain techniques, where transport properties of quantum fluids have been determined by measuring the hydrodynamic linear susceptibility Hohenberg and Martin [1965]; Hu et al. [2018]; Zhang and Yu [2018]; Mukherjee et al. [2019]. However, this method has several advantages over traditional frequency domain techniques.

First, the freedom of designing proper initial conditions in the time domain allows decoupling of physical properties. In our case, the contribution of the thermal diffusion mode and the first sound mode are in phase for the density perturbation $\delta n(q,0)$, but 180° out of phase for the temperature perturbation $\delta T(q,0)$, allowing separation of the thermal conductivity and the sound diffusivity.

Second, frequency domain techniques usually require driving the system to a steady state, during which additional uncertainties could be added, such as extra energy exchanges or an uncertain driving sufficiency. In contrast, free evolution methods start from the steady state, making measurements simple.

In conclusion, I believe the new time-domain free evolution methods presented in this

dissertation will shed new light on measuring in ultracold quantum gases, or even other few-body or many-body quantum systems.

## 6.2 Outlook

Prior to our work, it was not obvious that simply measuring the hydrodynamic decay of a periodic density perturbation, created in a box potential, would enable a clear separation of the contributions of a zero frequency, thermally diffusive mode and an oscillating first sound mode in a normal fluid unitary Fermi gas. It can be expected that this idea can be applied to many other experiments.

For the next generation experiments in our laboratory, one would expect to explore in the superfluid regime, where the exponentially decaying mode will evolve into an oscillating second sound mode. It is also interesting to change the interaction strength across the BEC-BCS crossover, and from strong to weak interactions, to study the breakdown of fluid dynamics and other novel phenomenon. Also, trapping a spin-imbalanced mixture to study transport properties is another interesting topic.

As discussed in chapter 5, our experiments were not performed in a perfect hydrodynamic regime due to systematic limits. We hope to build a system with higher atom density and longer perturbing wavelength to measure those first order transport properties one level better. In contrast, lowering the density and reducing the wavelength would move the system away from first order hydrodynamic regime, proving a platform to study higher order transport properties. Also, we hope to use the DMD to flatten the potential inside the box, making density uniform in all directions.

Furthermore, since our data emphasize the need for rigorous calculations of the leading purely density-dependent corrections to the two-body high temperature limits of the transport coefficients, related theoretical studies are expected.

We expect that for the general application of arbitrary optical beam modulating techniques, including the DMDs and diffractive beam shapers, great prosperity in future experiments on cold atoms and molecules in all dimensionalites and geometries can be foreseen.

# REFERENCES


DLP7000 DLP 0.7 XGA 2x LVDS Type A DMD datasheet. See https://www.ti.com/product/DLP7000.

A new method for directly measuring temperature waves has been reported recently, accessing second sound and thermal diffusion in a unitary Fermi gas. See Z. Yan, P. B. Patel, B. Mukherjee, R. Fletcher, and M. W. Zwierlein, DAMOP21/Session/U07.2 .

Application notes for the HOLO/OR Top-Hat beam shaper. See https://www.holoor.co.il/application/beam-shaper-top-hat/.

A. Adams, L. D. Carr, T. Schäfer, P. Steinberg, and J. E. Thomas. Strongly correlated quantum fluids: ultracold quantum gases, quantum chromodynamic plasmas and holographic duality. *New J. Phys.*, 14:115009, 2012.

M. H. Anderson, J. R. Ensher, M. R. Matthews, C. E. Wieman, and E. A. Cornell. Observation of bose-einstein condensation in a dilute atomic vapor. *science*, 269(5221):198–201, 1995.

E. Arimondo, M. Inguscio, and P. Violino. Experimental determinations of the hyperfine structure in the alkali atoms. *Rev. Mod. Phys.*, 49:31–75, 1977.

L. Baird, X. Wang, S. Roof, and J. E. Thomas. Measuring the hydrodynamic linear response of a unitary Fermi gas. *Phys. Rev. Lett.*, 123:160402, 2019.

J. Bardeen, L. N. Cooper, and J. R. Schrieffer. Theory of superconductivity. *Phys. Rev.*, 108: 1175–1204, 1957.

R. Bause, A. Schindewolf, R. Tao, M. Duda, X.-Y. Chen, G. Quéméner, T. Karman, A. Christianen, I. Bloch, and X.-Y. Luo. Collisions of ultracold molecules in bright and dark optical dipole traps. *Phys. Rev. Research*, 3:033013, 2021.

P. L. Bhatnagar, E. P. Gross, and M. Krook. A model for collision processes in gases. i. small amplitude processes in charged and neutral one-component systems. *Phys. Rev.*, 94: 511–525, 1954.

I. Bloch, J. Dalibard, and W. Zwerger. Many-body physics with ultracold gases. *Rev. Mod. Phys.*, 80:885–964, 2008.

I. Bloch, J. Dalibard, and S. Nascimbène. Quantum simulations with ultracold quantum gases. *Nature Physics*, 8:267, 2012.

M. Bluhm and T. Schäfer. Model-independent determination of the shear viscosity of a trapped unitary Fermi gas: Application to high-temperature data. *Phys. Rev. Lett.*, 116: 115301, 2016.

M. Bluhm, J. Hou, and T. Schäfer. Determination of the density and temperature dependence of the shear viscosity of a unitary Fermi gas based on hydrodynamic flow. *Phys. Rev. Lett.*, 119:065302, 2017.

M. Bohlen, L. Sobirey, N. Luick, H. Biss, T. Enss, T. Lompe, and H. Moritz. Sound propagation and quantum-limited damping in a two-dimensional fermi gas. *Phys. Rev. Lett.*, 124: 240403, 2020.

T. Bourdel, L. Khaykovich, J. Cubizolles, J. Zhang, F. Chevy, M. Teichmann, L. Tarruell, S. J. J. M. F. Kokkelmans, and C. Salomon. Experimental study of the bec-bcs crossover region in lithium 6. *Phys. Rev. Lett.*, 93:050401, 2004.

M. Braby, J. Chao, and T. Schäfer. Thermal conductivity and sound attenuation in dilute atomic Fermi gases. *Phys. Rev. A*, 82:033619, 2010.

M. Braby, J. Chao, and T. Schäfer. Viscosity spectral functions of the dilute fermi gas in kinetic theory. *New Journal of Physics*, 13(3):035014, 2011.

C. C. Bradley, C. Sackett, J. Tollett, and R. G. Hulet. Evidence of bose-einstein condensation in an atomic gas with attractive interactions. *Physical review letters*, 75(9):1687, 1995.

G. M. Bruun and H. Smith. Shear viscosity and damping for a Fermi gas in the unitary limit. *Phys. Rev. A*, 75:043612, 2007.

C. Cao, E. Elliott, J. Joseph, H. Wu, J. Petricka, T. Schäfer, and J. E. Thomas. Universal quantum viscosity in a unitary Fermi gas. *Science*, 331:58, 2011.

S. Chapman, T. Cowling, D. Burnett, and C. Cercignani. *The Mathematical Theory of Non-uniform Gases: An Account of the Kinetic Theory of Viscosity, Thermal Conduction and Diffusion in Gases*. Cambridge Mathematical Library. Cambridge University Press, 1990.

C. Chin, R. Grimm, P. Julienne, and E. Tiesinga. Feshbach resonances in ultracold gases. *Rev. Mod. Phys.*, 82:1225–1286, 2010.

P. Christodoulou, M. Gałka, N. Dogra, R. Lopes, J. Schmitt, and Z. Hadzibabic. Observation of first and second sound in a bkt superfluid. *Nature*, 594(7862):191–194, 2021.

K. B. Davis, M.-O. Mewes, M. R. Andrews, N. J. van Druten, D. S. Durfee, D. Kurn, and W. Ketterle. Bose-einstein condensation in a gas of sodium atoms. *Physical review letters*, 75(22):3969, 1995.

B. DeMarco and D. S. Jin. Onset of fermi degeneracy in a trapped atomic gas. *Science*, 285 (5434):1703–1706, 1999.

E. Elliott, J. A. Joseph, and J. E. Thomas. Observation of conformal symmetry breaking and scale invariance in expanding Fermi gases. *Phys. Rev. Lett.*, 112:040405, 2014.

T. Enss. Quantum critical transport in the unitary fermi gas. *Phys. Rev. A*, 86:013616, 2012.

T. Enss, R. Haussmann, and W. Zwerger. Viscosity and scale invariance in the unitary Fermi gas. *Annals Phys.*, 326:770–796, 2011.

W. Florkowski, R. Ryblewski, and M. Spaliński. Gradient expansion for anisotropic hydrodynamics. *Phys. Rev. D*, 94:114025, 2016.

B. Frank, W. Zwerger, and T. Enss. Quantum critical thermal transport in the unitary Fermi gas. *Phys. Rev. Research*, 2:023301, 2020.

G. Gauthier, T. A. Bell, A. B. Stilgoe, M. Baker, H. Rubinsztein-Dunlop, and T. W. Neely. Dynamic high-resolution optical trapping of ultracold atoms. In *Advances in Atomic, Molecular, and Optical Physics*, volume 70, pages 1–101. Elsevier, 2021.

M. Gehm. *Preparation of an Optically-Trapped Degenerate Fermi Gas of $^6$Li: Finding the Route to Degeneracy*. PhD thesis, Duke University, 2003.

M. Greiner, C. A. Regal, and D. S. Jin. Emergence of a molecular bose–einstein condensate from a fermi gas. *Nature*, 426(6966):537–540, 2003.

T.-L. Ho. Universal thermodynamics of degenerate quantum gases in the unitarity limit. *Phys. Rev. Lett.*, 92:090402, 2004.

J. Hofmann. High-temperature expansion of the viscosity in interacting quantum gases. *Phys. Rev. A*, 101:013620, 2020.

P. Hohenberg and P. Martin. Microscopic theory of superfluid helium. *Annals Phys.*, 34(2): 291–359, 1965. ISSN 0003-4916.

Y.-H. Hou, L. P. Pitaevskii, and S. Stringari. Scaling solutions of the two-fluid hydrodynamic equations in a harmonically trapped gas at unitarity. *Phys. Rev. A*, 87:033620, 2013.

M. Houbiers, H. T. C. Stoof, W. I. McAlexander, and R. G. Hulet. Elastic and inelastic collisions of $^6$Li atoms in magnetic and optical traps. *Phys. Rev. A*, 57:R1497–R1500, 1998.

H. Hu, P. Zou, and X.-J. Liu. Low-momentum dynamic structure factor of a strongly interacting Fermi gas at finite temperature: A two-fluid hydrodynamic description. *Phys. Rev. A*, 97:023615, 2018.

K. Hueck, N. Luick, L. Sobirey, J. Siegl, T. Lompe, and H. Moritz. Two-dimensional homogeneous fermi gases. *Phys. Rev. Lett.*, 120:060402, Feb 2018. doi: 10.1103/PhysRevLett.120.060402. URL `https://link.aps.org/doi/10.1103/PhysRevLett.120.060402`.

A. Jagannathan. *Optical Control of Magnetic Feshbach Resonances by Closed-Channel Electromagnetically Induced Transparency*. PhD thesis, Duke University, 2016.

S. Jochim, M. Bartenstein, A. Altmeyer, G. Hendl, S. Riedl, C. Chin, J. H. Denschlag, and R. Grimm. Bose-einstein condensation of molecules. *Science*, 302(5653):2101–2103, 2003.

J. Joseph. *Precision Measurement of the Sound Velocity in an Ultracold Fermi Gas through the BEC-BCS Crossover*. PhD thesis, Duke University, 2010.

J. A. Joseph, E. Elliott, and J. E. Thomas. Shear viscosity of a unitary Fermi gas near the superfluid phase transition. *Phys. Rev. Lett.*, 115:020401, 2015.

W. Ketterle and M. W. Zwierlein. Making, probing and understanding ultracold fermi gases. *La Rivista del Nuovo Cimento*, 31(5):247–422, 2008.

J. Kinast. *Thermodynamics and SuperFluidity of a Strongly Interacting Fermi Gas*. PhD thesis, Duke University, 2006.

M. Ku, A. T. Sommer, L. W. Cheuk, and M. W. Zwierlein. Revealing the superfluid lambda transition in the universal thermodynamics of a unitary Fermi gas. *Science*, 335:563, 2012.

C. C. N. Kuhn, S. Hoinka, I. Herrera, P. Dyke, J. J. Kinnunen, G. M. Bruun, and C. J. Vale. High-frequency sound in a unitary fermi gas. *Phys. Rev. Lett.*, 124:150401, 2020.

L. D. Landau and E. M. Lifshitz. *Fluid Dynamics, Course of Theoretical Physics Vol. VI*. Pergamon Press, Oxford, 1959.

X. Li, X. Luo, S. Wang, K. Xie, X.-P. Liu, H. Hu, Y.-A. Chen, X.-C. Yao, and J.-W. Pan. Second sound attenuation near quantum criticality. *Science*, 375(6580):528–533, 2022.

J. Maki and S. Zhang. Role of effective range in the bulk viscosity of resonantly interacting $s$- and $p$-wave fermi gases. *Phys. Rev. Lett.*, 125:240402, 2020.

A. J. Moerdijk, B. J. Verhaar, and A. Axelsson. Resonances in ultracold collisions of $^6$Li, $^7$Li, and $^{23}$Na. *Phys. Rev. A*, 51:4852–4861, 1995.

B. Mukherjee, Z. Yan, P. B. Patel, Z. Hadzibabic, T. Yefsah, J. Struck, and M. W. Zwierlein. Homogeneous atomic fermi gases. *Phys. Rev. Lett.*, 118:123401, 2017.

B. Mukherjee, P. B. Patel, Z. Yan, R. J. Fletcher, J. Struck, and M. W. Zwierlein. Spectral response and contact of the unitary fermi gas. *Phys. Rev. Lett.*, 122:203402, 2019.

N. Navon, R. P. Smith, and Z. Hadzibabic. Quantum gases in optical boxes. *Nature Physics*, pages 1–8, 2021.

Y. Nishida. Viscosity spectral functions of resonating fermions in the quantum virial expansion. *Annals of Physics*, 410:167949, 2019.

K. M. O'Hara. *Optical Trapping and Evaporative Cooling of Fermionic Atoms*. PhD thesis, Duke University, 2000. URL `http://adsabs.harvard.edu/abs/2000PhDT.....190`.

K. M. O'Hara, S. L. Hemmer, M. E. Gehm, S. R. Granade, and J. E. Thomas. Observation of a strongly interacting degenerate Fermi gas of atoms. *Science*, 298:2179, 2002.

K. O'Hara, M. E. Gehm, S. Granade, and J. Thomas. Scaling laws for evaporative cooling in time-dependent optical traps. *Physical Review A*, 64(5):051403, 2001.

P. B. Patel, Z. Yan, B. Mukherjee, R. J. Fletcher, J. Struck, and M. W. Zwierlein. Universal sound diffusion in a strongly interacting Fermi gas. *Science*, 370:1222–1226, 2020.

J. Sakurai and J. Napolitano. *Modern Quantum Mechanics*. Cambridge University Press, 2020.

T. Schäfer. Fluid dynamics and viscosity in strongly correlated fluids. *Annual Review of Nuclear and Particle Science*, 64:125–148, 2014.

D. T. Son. Vanishing bulk viscosities and conformal invariance of the unitary Fermi gas. *Phys. Rev. Lett.*, 98:020604, 2007.

G. C. Strinati, P. Pieri, G. Röpke, P. Schuck, and M. Urban. The BCS-BEC crossover: From ultra-cold Fermi gases to nuclear systems. *Physics Reports*, 738:1–76, 2018.

M. Tajik, B. Rauer, T. Schweigler, F. Cataldini, J. Sabino, F. S. Møller, S.-C. Ji, I. E. Mazets, and J. Schmiedmayer. Designing arbitrary one-dimensional potentials on an atom chip. *Optics express*, 27(23):33474–33487, 2019.

J. R. Taylor. *An introduction to Error Analysis*. University Science Books, 2 edition, 1997.

J. E. Thomas, J. Kinast, and A. Turlapov. Virial theorem and universality in a unitary Fermi gas. *Phys. Rev. Lett.*, 95:120402, 2005.

C. J. Vale and M. Zwierlein. Spectroscopic probes of quantum gases. *Nature Physics*, pages 1–11, 2021.

J. L. Ville, R. Saint-Jalm, E. Le Cerf, M. Aidelsburger, S. Nascimbène, J. Dalibard, and J. Beugnon. Sound propagation in a uniform superfluid two-dimensional bose gas. *Phys. Rev. Lett.*, 121:145301, 2018.

X. Wang, X. Li, I. Arakelyan, and J. E. Thomas. Hydrodynamic relaxation in a strongly interacting fermi gas. *Phys. Rev. Lett.*, 128:090402, Mar 2022. doi: 10.1103/PhysRevLett.128.090402. URL `https://link.aps.org/doi/10.1103/PhysRevLett.128.090402`.

G. Wlazłowski, P. Magierski, and J. E. Drut. Shear viscosity of a unitary fermi gas. *Phys. Rev. Lett.*, 109:020406, 2012.

P. Zhang and Z. Yu. Energy-absorption spectroscopy of unitary Fermi gases in a uniform potential. *Phys. Rev. A*, 97:041601, 2018.

Z. Zhang, L. Chen, K.-X. Yao, and C. Chin. Transition from an atomic to a molecular bose–einstein condensate. *Nature*, 592(7856):708–711, 2021.

H. Zhou and Y. Ma. Thermal conductivity of an ultracold Fermi gas in the BCS-BEC crossover. *Sci. Rep.*, 11:1228, 2021.

G. Zürn, T. Lompe, A. N. Wenz, S. Jochim, P. S. Julienne, and J. M. Hutson. Precise characterization of $^6$Li feshbach resonances using trap-sideband-resolved rf spectroscopy of weakly bound molecules. *Phys. Rev. Lett.*, 110:135301, 2013.

M. W. Zwierlein, C. A. Stan, C. H. Schunck, S. M. F. Raupach, A. J. Kerman, and W. Ketterle. Condensation of pairs of fermionic atoms near a feshbach resonance. *Phys. Rev. Lett.*, 92: 120403, 2004.

# APPENDICES

APPENDIX

# A

# CODE FOR JAVIS HALFTONING

This code is found online by the author below for performing Javis Halftoning.

```
%Program for Image Halftoning by Jarvis Method

%Program Description
% The input gray image will be converted into halftone image
% of same size using Jarvis's Error Diffusion Method.
%
%Parameters
% inImg   -   Input Gray Image
% outImg  -   Output Halftoned Image

%Author : Athi Narayanan S
%Student, M.E, EST,
%K.S.R College of Engineering
%Erode, Tamil Nadu, India.
%s_athi1983@yahoo.co.in
```

```
%http://sites.google.com/site/athisnarayanan/
%
function outImg = jarvisHalftone(inImg)
% inImg = flipud(inImg);
inImg = double(inImg);

[M,N] = size(inImg);

% 255/2
% T = 127.5;
T = .5;
y = inImg;
error = 0;

y= [127.5*ones(M,2) y 127.5*ones(M,2) ; 127.5*ones(2,N+4)];
z = y;

for rows = 1:M
  for cols = 3:N+2

    % round up or down to be binary

    z(rows,cols) =T*2*(y(rows,cols)>=T);

    % error of the rounding calculated

    error = -z(rows,cols) + y(rows,cols);

    %error is distributed among neighboring pixels

    y(rows,cols+2) = 5/48 * error + y(rows,cols+2);
    y(rows,cols+1) = 7/48 * error + y(rows,cols+1);

    y(rows+1,cols+2) = 3/48 * error + y(rows+1,cols+2);
    y(rows+1,cols+1) = 5/48 * error + y(rows+1,cols+1);
```

```
51      y(rows+1,cols+0) = 7/48 * error + y(rows+1,cols+0);
52      y(rows+1,cols-1) = 5/48 * error + y(rows+1,cols-1);
53      y(rows+1,cols-2) = 3/48 * error + y(rows+1,cols-2);
54
55      y(rows+2,cols+2) = 1/48 * error + y(rows+2,cols+2);
56      y(rows+2,cols+1) = 3/48 * error + y(rows+2,cols+1);
57      y(rows+2,cols+0) = 5/48 * error + y(rows+2,cols+0);
58      y(rows+2,cols-1) = 3/48 * error + y(rows+2,cols-1);
59      y(rows+2,cols-2) = 1/48 * error + y(rows+2,cols-2);
60    end
61  end
62
63  outImg = z(1:M,3:N+2);
64  % outImg = im2bw(uint8(outImg));
```

APPENDIX

# B

# CODE FOR NUMERICAL INTEGRATION

Use this code for the numerical integration method in Sec. 4.2.1, based on the hydrodynamic linear response model.

```
function [f,fax1,fax1err,faxN1,dn,ndata,ndataerr,nbgdata,bigax,
    bigaxN] = ...
     XinLinearHydroNI(n0peak2use,axnormbg2use,axihat1,axnorm1,
         axerrnorm1,camera,timestep,t1,t4,lower,upper,cT,SDiff,eta,
         CR,FEtheta,n)

% input 1D density as delta n
% axnorm1 and axerrnorm1 are the points exclude 2 sigma away
tn=t4-t1+1;

sft = 0;
startpoint = 1; endpoint = length(axnormbg2use);
axcrt1 = axnorm1(startpoint:endpoint-sft,:)-axnormbg2use(
    startpoint+sft:endpoint);
```

```
11 axerrcrt1 = axerrnorm1(startpoint:endpoint-sft,:);     % bg error
       is small
12
13 axcrt=zeros(length(axcrt1),tn);
14 axcrt(:,1)=axihat1;
15 axcrt(:,2:tn)=axcrt1(:,6:tn+4);
16
17 axerrcrt=zeros(length(axerrcrt1),tn);
18 axerrcrt(:,1)=mean(axerrcrt1(:,1:5),2)./sqrt(5);
19 axerrcrt(:,2:tn)=axerrcrt1(:,6:tn+4);
20
21
22
23 [nfit,densityOffset] = PolyTanhAnalyticFunction(axnormbg2use(
       startpoint+sft:endpoint));
24
25 % rescale the data from pixels to microns
26 ntwid = abs(nfit-(max(nfit)-1))./max(nfit-(max(nfit)-1));
27 x = linspace(1,length(ntwid),length(ntwid)) .* camera.psize;
28 numzpoints = floor(max(x));
29 z = linspace(1,numzpoints,numzpoints) ;
30 dz = z(2) - z(1);
31 nscale = max(interp1(x,ntwid,z,'spline'),0.0001);
32 nfitz = interp1(x,nfit,z,'spline');
33 ndatainit = interp1(x,axcrt(:,1),z,'spline');
34 ndata = interp1(x,axcrt,z,'spline');
35 ndataerr = interp1(x,axerrcrt,z,'spline');
36 nbgdata = interp1(x,axnormbg2use(startpoint+sft:endpoint),z,'
       spline');
37 % load Martin's fE data and interpolate
38 load('MartinEEOS.mat');
39 dtheta = 0.001;
40 theta0steps = 0:dtheta:1.5;
41 fE = interp1(FEtheta(:,1),FEtheta(:,2),theta0steps,'pchip');
42 fEprime = gradient(fE,dtheta);
```

```
43
44
45 % find theta0 from sound velocity and average density
46 % boxvol = (167e-4)*(43e-4)*(54e-4);      % box size in microns
       for cylindrical gaussian box
47 % boxvol = (160e-4)*(43.5e-4)*(51e-4);     % box size in microns
       for TH box
48 % boxvol = (107e-4)*(43.5e-4)*(51e-4);     % box size for center
       of Smaller TH box
49 % n0 = 2*Nctrbg2use/boxvol;      % use this for data taken after
       spin balance fix
50
51 n0 = 2*n0peak2use;               % use this for max density in the
       center
52 kB = 1.3806504E-16;
53 hbar = 1.0545716E-27;
54 mLi6 = 9.9883414E-24;
55
56 eF0 = hbar^2/(2*mLi6)*(3*pi^2*n0)^(2/3)/kB;     %cgs
57 vF0 = sqrt(2*eF0*kB/mLi6);
58 cTInterp = vF0*sqrt(fE/3-(2/15).*fEprime.*theta0steps);
59
60 theta0 = interp1(cTInterp,theta0steps,cT,'pchip');
61
62 fE0 = interp1(theta0steps,fE,theta0,'pchip');
63 fE0prime = interp1(theta0steps,fEprime,theta0,'pchip');
64
65
66 thetaZ = theta0 ./ (nscale.^(2/3));
67
68 fEthetaZ = interp1(FEtheta(:,1),FEtheta(:,2),thetaZ,'spchip');
69 grad_fEthetaZ = gradient(fEthetaZ,dz);
70
71 % hydro-thermal properties
72 CV1 = (3/5) * fE0prime;
```

```
73 CP1 = CV1 * fE0 / (fE0 -(2/5) * theta0 *fE0prime);
74
75 alfa = (hbar/mLi6) * eta;
76
77
78 C1 = CR - 1;
79 C2 = SDiff * (hbar/mLi6);
80
81 % gradient method
82 dU0dz = (-2/3) .* (fEthetaZ - (2/5) .* thetaZ .*...
83 grad_fEthetaZ) .* (gradient(nfitz,dz) ./ (nscale .^ (1/3)));
84 % figure;plot(dU0dz);
85
86 U0 = zeros(size(dU0dz));
87 for i = 1:length(dU0dz)
88     U0(i) = sum(dU0dz(1:i));
89 end
90
91 dt = 1e-6;
92 tend=timestep*(t4-t1)+1;          % for ending time in simulation
93 t = linspace(0,tend,tend+1) * dt;
94
95 dn = zeros(length(t), length(z));
96 dn(1,:) = ndatainit;
97 dn(2,:) = ndatainit;
98 dndot = zeros(length(t), length(z));
99 dUdz = ones(length(t) - 1, length(z)) .* dU0dz * 1e4;
100 V0force = zeros(length(t) - 1, length(z)) ;
101 dT = zeros(length(t), length(z));
102
103
104
105 for i = 3:(length(t))
106     dndot(i-1,:) = 1/dt .* (dn(i - 1,:)-dn(i - 2,:));
107
```

```
108       dndotdz = gradient(dndot(i - 1,:),dz*1e-4);
109       d2ndotdz2 = gradient(dndotdz,dz*1e-4);
110
111       dndz = gradient(dn(i - 1,:),dz*1e-4);
112       d2ndz2 = gradient(dndz, dz*1e-4);
113
114       dTdz = gradient(dT(i - 1,:),dz*1e-4);
115       d2Tdz2 = gradient(dTdz,dz*1e-4);
116
117
118
119       V0force(i - 1 ,:) = 0.5 .* vF0.^2 .* gradient(dn(i - 1,:) .*
              dUdz(i - 1,:),dz*1e-4);
120
121
122       dn(i,:) = 2 .* dn(i - 1,:) - dn(i - 2,:) + dt.^ 2 .* (cT ^ 2
              .* (d2ndz2 + d2Tdz2)...
123        + (4/3) .* alfa .* d2ndotdz2 + V0force(i - 1,:));
124       supress = dn(i,:);
125       old = dn(i - 1,:);
126       supress( nscale <.0003) = old( nscale <.0003);
127       dn(i,:) = supress;
128
129       dT(i,:) = dT(i - 1,:) + C1.*(dn(i,:)-dn(i-1,:)) + dt .*C2 .*
              d2Tdz2;
130   end
131
132   dn=dn';       % reshape to agree with ndata
133   dn=dn(:,((t1:t4)-t1)*timestep+1);  %reduce num of dn to the same
          as data
134
135
136
137   %% Fourier transform
138
```

```
139
140 % n=2000;
141
142 ax=ndata(lower:upper,:);
143 axerr=ndataerr(lower:upper,:);
144 bigax=zeros(n,size(ax,2));
145 bigaxerr=zeros(n,size(axerr,2));
146 bigax(n/2+1-round(length(ax)/2):n/2+round((length(ax)-1)/2),:)=ax;
147 bigaxerr(n/2+1-round(length(ax)/2):n/2+round((length(ax)-1)/2),:)=
      axerr;
148
149 axN=dn(lower:upper,:);
150 bigaxN=zeros(n,size(axN,2));
151 bigaxN(n/2+1-round(length(ax)/2):n/2+round((length(ax)-1)/2),:)=
      axN;
152 fax=zeros(size(bigax,1),size(bigax,2));
153 faxerr=zeros(size(bigaxerr,1),size(bigaxerr,2));
154
155 Fs=n;            % sampling frequency
156
157
158 for i=1:size(bigax,2)
159
160     fax(:,i)=real(fft(bigax(:,i)));      % method of direct FFT
161     faxerr(:,i)=abs(real(fft(bigaxerr(:,i))));
162
163 end
164
165 fax1=fax(1:n/2+1,:);
166 fax1err=faxerr(1:n/2+1,:);
167 fax1(2:end-1,:)=2*fax1(2:end-1,:);
168 fax1err(2:end-1,:)=2*fax1err(2:end-1,:);
169
170
171
```

```
faxN=zeros(size(bigaxN,1),size(bigaxN,2));
for i=1:size(bigaxN,2)
    faxN(:,i)= real(fft(bigaxN(:,i)));
%     faxN(:,i)= abs(fft(bigaxN(:,i)));

end


faxN1=faxN(1:n/2+1,:);
faxN1(2:end-1,:)=2*faxN1(2:end-1,:);
f = Fs*(0:(n/2))/n;
```

Use this code to get the Fourier transform of $\delta n(z,t)$. The filter applied on the initial condition $\delta n(z,0)$ is only for the purpose of choosing region of interest.

```
function [axihat1,axOrig1,f,mfax1,mfax2,sfax1,sfax2]=...
    XinFourierAndFilter(camera,MyData1,CDIndArray1,NormPoint,
        Nctrbg2use,axnorm1,axnormbg2use,ctr,lower,upper,n,wd)
% Get the FFT of each single shots and calculate the error
[nfiles1,~] = size(MyData1);

ff = ones(nfiles1,1);

PSummary = unique(MyData1.Parameter);
Nparams = length(PSummary);

x = linspace(1,length(axnormbg2use),length(axnormbg2use)) .*
    camera.psize;
numzpoints = floor(max(x));
z = linspace(1,numzpoints,numzpoints) ;

% n=2000;
f = 0:n/2;

mfax1 = zeros(n/2+1,Nparams-4);
```

```
19 mfax2 = zeros(n/2+1,Nparams-4);
20 sfax1 = zeros(n/2+1,Nparams-4);
21 sfax2 = zeros(n/2+1,Nparams-4);
22
23 % For initial condition, which is average of first 5 shots
24 for i=1:5
25 fparam=logical((MyData1.Parameter==PSummary(i+0)).*ff);
26 CDsum=sum(CDIndArray1(:,ctr-wd:ctr+wd,fparam),2);
27 Nctr1=sum(sum(CDIndArray1(:,ctr-wd:ctr+wd,fparam)))*camera.psize
    ^2;
28 axn = CDsum./reshape(Nctr1,1,1,[])*Nctrbg2use/NormPoint -
    axnormbg2use;
29
30 fax2F(:,i) = mean(fft(axn),3);      % for the initial goes to
    filter
31 ax = interp1(x,axn,z,'spline');
32 bigax=zeros(n,1,size(ax,3));
33 bigax(n/2+1-round(length(ax(lower:upper,:,:))/2):n/2+round((length
    (ax(lower:upper,:,:))-1)/2),:)=ax(lower:upper,:,:);
34 fax=fft(bigax);
35 fax1=fax(1:n/2+1,:,:);
36 fax1(2:end-1,:,:)=2*fax1(2:end-1,:,:);
37
38 sfax1(:,i)=std(real(fax1),0,3)/sqrt(sum(fparam));
39
40 end
41
42 fax2Filter=mean(fax2F,2);
43
44 % apply the filter for initial condition here
45 figure(107);plot(abs(fax2Filter(:,1)));
46 dlg_title='Cutoff Input';
47 num_lines=[1 30];
48 defaultans={'0.5'};
49 prompt1='enter the cutoff value:';
```

```
50 answer1=str2double(inputdlg(prompt1,dlg_title,num_lines,defaultans
   ));
51 indices=abs(fax2Filter(:,1))>answer1;     % only apply filter to
   initial condition
52 close figure 107;
53 axhat1=fax2Filter(:,1).*indices;
54 axihat1=ifft(axhat1);
55
56 % FFT of the new initial condition
57
58 ax1 = (interp1(x,axihat1,z,'spline'))';
59 bigax1=zeros(n,1);
60 bigax1(n/2+1-round(length(ax1(lower:upper,1))/2):n/2+round((length
   (ax1(lower:upper,1))-1)/2),1)=ax1(lower:upper,1);
61 fax=fft(bigax1);
62 fax1=fax(1:n/2+1,:);
63 fax1(2:end-1,:)=2*fax1(2:end-1,:);
64
65
66 mfax1(:,1)=real(fax1);
67 % mfax1(:,1)=abs(fax1);
68 sfax1(:,1)=mean(sfax1(:,1:5),2)/sqrt(5);
69
70 % mfax2(:,1)=imag(fax1);
71 mfax2(:,1)=abs(fax1);
72
73
74 % campare with non-filted one
75 axOrig = mean(axnorm1(:,1:5) - axnormbg2use,2);
76 axOrig1 = (interp1(x,axOrig,z,'spline'))';
77 figure(120);plot(axOrig1);hold on;
78 plot(ax1);hold off;
79
80
81 for i=6:Nparams
```

```
82  fparam=logical((MyData1.Parameter==PSummary(i+0)).*ff);
83 CDsum=sum(CDIndArray1(:,ctr-wd:ctr+wd,fparam),2);
84  Nctr1=sum(sum(CDIndArray1(:,ctr-wd:ctr+wd,fparam)))*camera.psize
        ^2;
85  axn = CDsum./reshape(Nctr1,1,1,[])*Nctrbg2use/NormPoint -
        axnormbg2use;
86
87  ax = interp1(x,axn,z,'spline');
88  bigax=zeros(n,1,size(ax,3));
89  bigax(n/2+1-round(length(ax(lower:upper,:,:))/2):n/2+round((length
        (ax(lower:upper,:,:))-1)/2),:)=ax(lower:upper,:,:);
90  fax=fft(bigax);
91
92  fax1=fax(1:n/2+1,:,:);
93  fax1(2:end-1,:,:)=2*fax1(2:end-1,:,:);
94
95
96  mfax1(:,i-4)=real(mean(fax1,3));
97 % mfax1(:,i-4)=abs(mean(fax1,3));
98
99 % mfax2(:,i-4)=imag(mean(fax1,3));    % use mfax2 as imaginary part
100 mfax2(:,i-4)=abs(mean(fax1,3));     % use mfax2 as absolute value
101
102 sfax1(:,i-4)=std(real(fax1),0,3)/sqrt(sum(fparam));
103 % sfax1(:,i-4)=std(abs(fax1),0,3)/sqrt(sum(fparam));
104
105 sfax2(:,i-4)=std(imag(fax1),0,3)/sqrt(sum(fparam));
106 % sfax2(:,i-4)=sqrt(var(real(fax1),0,3)+var(imag(fax1),0,3))/sqrt(
        sum(fparam));
107
108
109 end
110
111 end
```

APPENDIX

# C

# CODE FOR EXACT ANALYTIC FIT FUNCTION

This code is used for the "exact analytic fit funciton" method in Sec. 4.2.4. It provides both the 4-parameter fit (floating A) and the 3-parameter fit (fixing A for measured $\delta n(q,0)$.

```
function EAnFit = fitExactAnalytic(x,t,dnQ0,q,density)

if length(x)==4
    A = x(1);wT = x(2);Geta = x(3);Gkappa = x(4);
else
    A = dnQ0;wT = x(1);Geta = x(2);Gkappa = x(3);
end

cT = wT/q;
syms('S','real')
Cub_eq = S^3-S^2*(Gkappa+Geta)+S*(wT^2*GetCPoverCV(density,cT)+
    Gkappa*Geta)-Gkappa*wT^2 == 0;
```

```
12 Gamma = double(solve(Cub_eq));
13
14 a = (Gkappa+Geta-Gamma)/2;
15 % wS = wT * sqrt(GetCPoverCV(density,cT));
16 b = sqrt((wT^2*GetCPoverCV(density,cT)+(Gamma-Gkappa)*(Gamma-Geta)
       -0.25*(Gkappa+Geta-Gamma)^2));
17 A0 = A*(a^2+b^2-wT^2)/((Gamma-a)^2+b^2);
18
19
20 EAnFit = A0.*exp(-Gamma.*t) + exp(-a.*t).*((A-A0).*cos(b.*t)+((
       Gamma-a)*A0+a*A)./b.*sin(b.*t));
```